The Dissertation Committee for Clara Leigh Feider Certifies that this is the approved version of the following Dissertation:

Advanced development of ambient ionization mass spectrometry imaging methods and their utilization towards the understanding of metabolic diseases

Committee:

Livia Schivinato Eberlin, Supervisor

Jennifer S. Brodbelt

Richard Crooks

Thomas Milner

Advanced development of ambient ionization mass spectrometry imaging methods and their utilization towards the understanding of metabolic diseases

by

Clara Leigh Feider

Dissertation

Presented to the Faculty of the Graduate School of

The University of Texas at Austin

in Partial Fulfillment

of the Requirements

for the Degree of

Doctor of Philosophy

The University of Texas at Austin

August 2020

Dedication

To my loving grandfather, Leroy Feider, who has selflessly supported all my endeavors and without whom I would have never accomplished this milestone. I love you, Nonno.

Acknowledgements

There are so many people in my life that deserve recognition for what they have done for me during my path to obtaining my PhD. It would not be right of me to take the credit for an accomplishment that we all share. First, I would like to thank my entire family for their constant support, specifically my parents Robert and Teri, my grandfather Leroy, and my sister Annabel. Dad, you have always taught me that I can accomplish anything I set my mind to and I attribute my analytical mind and quest for knowledge to you. Mom, you have always supported me and never stopped promoting me and my accomplishments to anyone who was around to listen. Your desire to understand and learn from me was a humbling experience. Nonno, without you, none of my accomplishments would be possible. You have given selflessly to me more times than I can count so that I may follow my dreams and lead a life filled with joy and success. You are the greatest man I have ever known. Annabel, thank you for paving the way in our family and teaching me to follow my own path in life without regard for what others may believe. Thank you all for your love, support, and advice throughout my entire education. This would not have been possible without you. I love you so much.

To my advisor Prof. Livia S. Eberlin, I cannot express how thankful I am to you for helping me reach this milestone. You have taught me so much more than simply how to be a scientist. I admire your dedication, your perseverance, and your commitment to us and your family. You have always said that I have grown so much in the last five years, and I want you to know that you have inspired that growth. Thank you from the bottom of my heart for saying yes when I asked to be your first student, it has changed my life in many ways. I hope that I have made you proud. To my committee members, Dr. Jennifer

Brodbelt, Dr. Richard Crooks, and Dr. Tom Milner, thank you for your time and support throughout my PhD.

To my amazing research group, I love you all so much. We have been through so many ups and downs together while building this lab into something we should all be very proud of. Marta, thank you for being my other half on this PhD journey. We have shared so many moments together during the last five years and there is no one I would have rather had by my side that entire time. Jialing and Sunil, thank you for teaching me everything I know about mass spectrometry. Your mentorship and guidance was always appreciated and I have learned so much from our friendships. To Kyana, Rachel, and Alena, I loved getting to expand our little group with you three. You all inspired me to be better so that I could help you get better too. To Anna, Mary, and Abby, each of you brought something extremely special to our group: Anna brought the banter, Mary brought the puns, and Abby brought the sass. Thank you for making our lab the most fun place to work. To Mike, Sydney, Monica, and Meredith, I am so proud of what you four have accomplished thus far and I can't wait to see what you will do in the future. To all of our undergraduate students and past group members that have helped with many projects throughout my time here, including Jonathan Young, John Lin, Natalia Elizondo, Ofer Koren, Ashish Chakraborty, and Prajwal Gowda, your hard work did not go unnoticed or unappreciated and I wouldn't be here without you. I was so blessed to have you all as my friends and coworkers the last five years, and I don't think I will ever find a group of people I appreciate more than you all.

To my fantastic collaborators, this work would not have been possible without your ideas, knowledge, resources, and time. To those at Seton Medical Center, including Dr. Michael Breen, Dr. Suzanne Ledet, Katherine Sebastian, Loren Cain, and Faith Ozer, I appreciate your dedication that has allowed for me to work on a project that I believe

truly matters. To those within research labs at the University of Texas who have shared their resources and experience, including Dr. Jennifer Brodbelt, Dr. Dustin Klein, Luis Macias, Dr. Richard Crooks, Collin Davies, Logan Wilder, and Spencer Woody, I am thankful that you believed in my ideas and helped me bring them to fruition. And to those within my own research lab that went above and beyond to help me accomplish my goals and have assisted in the publications within this dissertation, specifically Kyana Garza, Anna Krieger, Rachel DeHoog, Marta Sans, and Jialing Zhang, I am forever grateful for your support.

To Mason Valentine, never in my wildest dreams did I think part of getting my PhD would be meeting you. You and I have done this together, and I can't imagine it any other way. Thank you for your love, your support, your jokes, and your constant presence in my life. I am so happy that we have shared this together and picked up our two buddies Kevin and Jasper along the way. I am excited to see what the future holds for us.

Thank you all once again for just being here with me throughout the last five years. It means so much more than you will ever know.

Abstract

Advanced development of ambient ionization mass spectrometry imaging methods and their utilization towards the understanding of metabolic diseases

Clara Leigh Feider, Ph.D.

The University of Texas at Austin, 2020

Supervisor: Livia S. Eberlin

Ambient ionization mass spectrometry (MS) technologies offer a unique opportunity to bring the specificity and sensitivity of MS into clinics, potentially allowing rapid analyses of biospecimens without need for sample preparation or highly trained personnel. As these technologies offer significant advantages over current technologies in terms of speed and suitability for a hospital environment, ambient ionization methods have been applied to a wide variety of clinical applications such as disease diagnosis, therapeutic drug monitoring, and biomarker discovery. Despite these successes, there remain challenges for these methods to overcome before they can be relied upon for routine analysis of patient samples. Prior to their use by physicians to inform decisions regarding patient care, ambient ionization MS technologies must be robust, versatile, and be shown to improve patient outcomes by providing information that is lacking in current standard of care procedures.

This dissertation serves to outline recent advancements made towards the improvements of ambient ionization MS technologies as well as the application of these

techniques towards disease indications that have yet to be explored. Chapter 2 provides data and discussion about how relative humidity can contribute to variability and poor data quality during desorption electrospray ionization (DESI) MS experiments, providing essential information about how atmospheric conditions can contribute to the robustness of the technique. Chapters 3 and 4 present methods for integration of new separation and fragmentation techniques with ambient ionization methods in order to increase the amount of information that can be gathered from a biological specimen. Finally, Chapter 5 presents results from the utilization of DESI-MS imaging towards understanding endometriosis, a chronic gynecological condition that has limited diagnosis and treatment options for patients. The entirety of this work aims to discuss how further improvements to ambient ionization MS technologies can make them useful for understanding a wider variety of disease processes and the progress that is being made to this end.

Table of Contents

List of Tables

List of Figures

List of Illustrations

Chapter 1: Introduction

1.1 Mass spectrometry for the molecular understanding of diseased tissue samples

Mass spectrometry (MS) has become a powerful tool for the investigation of the molecular composition of biological samples and to further understand the alterations within these chemical environments during times of dysregulated function. As mass spectrometers have increased in performance and decreased in size and costs, they have become an integral part of clinicals labs. The versatility, sensitivity, and specificity of mass spectrometers make them the ideal tool for the development of assays for the detection and diagnosis of many diseases from nearly any biological matrix. Methods have been implemented in clinical laboratories for the analysis of metabolites, lipids, and proteins from human samples to diagnosis a variety of ailments such as bacterial infections[1], prostate cancer[2], and adverse cardiac events[3], and research is currently ongoing to develop new MS biomarker detection assays.

The two most widely implemented MS techniques for biological sample assays and disease diagnosis are liquid chromatography mass spectrometry (LC-MS) and matrix assisted laser desorption/ionization mass spectrometry (MALDI-MS). LC-MS is a robust analytical tool that utilizes a liquid separation step to concentrate analytes of interest and remove unwanted contaminants within the sample. As analytes flow out of the separation column, they are introduced into the mass spectrometer by an ionization source. Electrospray ionization (ESI) is the most commonly used ionization source that is coupled to liquid chromatography, but other sources such as atmospheric pressure chemical ionization (APCI) and atmospheric pressure photoionization (APPI) can be used for specific applications. Chromatographic separation of analytes allows for low limits of

detection of analytes as well as the possibility of quantitative analysis of biomarkers within clinical samples.[4] However, LC-MS is limited to the analysis of liquid samples and often requires extensive sample preparation prior to introduction into the instrument to prevent contamination and clogging of the chromatography system and mass spectrometer, limiting throughput. Further, very targeted and standardized methods must be developed to analyze specific compounds and different molecular classes require significantly different separation and analytical parameters.[5] In MALDI-MS, a light-absorbing matrix is applied to the surface of a sample which can then be ablated with an ultraviolet laser, releasing analytes from the sample for MS analysis. MALDI-MS is advantageous in a clinical setting as it allows for direct analysis of both liquid and solid samples, reducing the need for extensive sample clean-up prior to analysis. Additionally, as MALDI-MS is not coupled to a chromatographic separation step, analysis of an entire molecular profile containing multiple molecular classes is possible and allows for simple biomarker discovery. The disadvantages of MALDI-MS, however, make it a less desirable clinical tool. For example, the matrix used for each application must be optimized for the sample type and the matrix application step can be time consuming and utilizes harmful chemicals.[6] Moreover, MALDI-MS is traditionally performed within a high vacuum apparatus which can further complicate introduction into a fast-paced clinical workflow.

A significant advancement in the field of clinical MS is the development of MS imaging, a technique in which a two-dimensional sample is rastered beneath an ionization source to collect MS data on a spot-by-spot basis, generating chemical maps of the species within a sample. MS imaging has been employed for a variety of applications but has shown highest promise in the field of biological tissue imaging as molecular information generated can be directly correlated to histological features within thin tissue

sections. MS imaging using MALDI-MS as well as secondary ion mass spectrometry (SIMS) has revolutionized the field of histological imaging, allowing for label-free and multiplexed interrogation of cell populations and tissue microenvironments for applications in disease diagnosis and clinical research.[7] Applications of MS imaging in clinical research have been wide reaching, spanning from distinguishing breast cancer molecular subtypes[8-10] to investigation of molecular alterations occurring with respect to pathogenic infections.[11,12] Further advancements in laser and ion beam technologies as well as histological image fusion algorithms have allowed for sub-micron pixel size for molecular ion images,[13-15] rapidly closing the resolution gap between MS imaging and traditional histological staining. Therefore, advanced development of these molecular imaging technologies could allow for future use of MS imaging in clinical laboratories.

1.2 AMBIENT IONIZATION MASS SPECTROMETRY IMAGING OF BIOLOGICAL TISSUE SECTIONS

The early 2000s brought a new age in the field with the introduction of ambient ionization MS techniques. Ambient ionization refers to "the ionization of unprocessed or minimally modified samples in their native environment, and it typically refers to the ionization of condensed phase samples in air." A wide variety of ambient ionization MS methods using versatile forms of energy to generate molecular ions have been developed, greatly expanding the use of these technologies while improving their performance for a range of applications (Illustration 1.1). However, one of the most prominent and most well-established uses for ambient ionization MS is biological sample

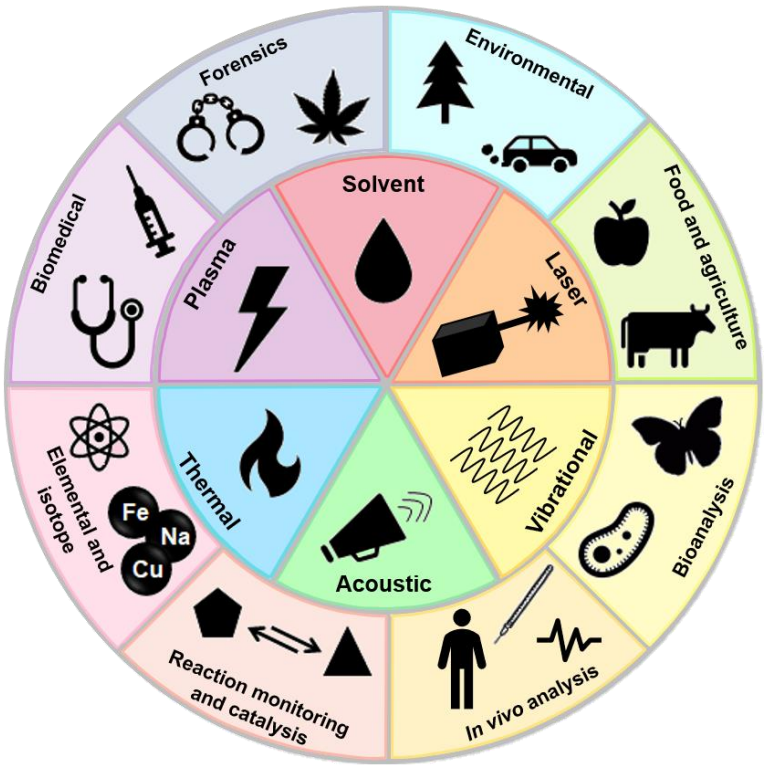

Illustration 1.1. Representation of the different modes of desorption/ionization typically used in ambient ionization techniques.

Pictured in the center wheel, and a variety of applications these methods can be used for, illustrated in the outer wheel of the figure. In this dissertation, the primary methods used are solvent extractions techniques applied to biomedical research applications. This figure is reprinted with permission from "Feider, C. L.; Krieger, A.; DeHoog, R. J.; Eberlin, L. S., Ambient Ionization Mass Spectrometry: Recent Developments and Applications. *Analytical Chemistry* **2019,** *91* (7), 4266-4290." Copyright 2019 American Chemical Society.

analysis within a clinical environment. Due to the minimal sample preparation steps required to generate molecular ions as well as the ability to perform these types of analyses in the open atmosphere, ambient ionization MS techniques are well suited for a clinical lab. Liquid extraction based ambient ionization techniques, in particular, have become the most widely used subclass of ambient ionization MS technologies for the analysis of biological sample due to their efficiency in generating molecular ions for many biological species such as metabolites, lipids, and proteins.[16] Additionally, most solvent-based ambient MS methods utilize an ESI mechanism, a soft ionization method that results in the generation of intact molecular ions which can be much more easily interpreted and directly correlated to biological processes.[17] Desorption electrospray ionization (DESI) was the first liquid extraction based ambient ionization MS method developed and is the most well-established of the techniques for the analysis of biological tissue sections.[18-20] DESI-MS utilizes a spray of charged solvent droplets to bombard a tissue surface and desorb analytes from the sample. The solvent-encapsulated molecules are then directed towards the inlet of the mass spectrometer, during which time the droplets undergo evaporation and coulombic explosion until the molecular ions are desolvated and can traverse through the mass spectrometer to the mass analyzer. Similarly to MALDI-MS, the DESI source can then be mounted onto a moving platform that can raster the sample beneath the solvent spray in two-dimensions, allowing for spatial mapping of the molecules within a sample. Further, use of histologically compatible solvent systems that allow for DESI- MS analysis without disrupting the cellular structure of tissue sections have facilitated direct comparison of pathological and molecular information from the same sample.[21] Therefore, DESI-MS is an ideal tool for the investigation of the lipid and metabolite composition of tissue samples and correlation of these molecular patterns to the disease state of the sample. DESI-MS has been

employed extensively to this end to facilitate the understanding of a variety of diseases, but efforts have been primarily focused on distinguishing between normal and cancerous tissue. Many cancers, including breast[22,23], ovarian[24,25], prostate[26], thyroid[27,28], and brain[20,29,30], among others, have been analyzed with DESI-MS, showing significant alterations in the molecular profiles between healthy and tumor tissues. The ability to distinguish cancerous and normal tissues with DESI-MS has encouraged the expansion of potential clinical applications for the technology, with recent work using the method for the investigation of metabolic changes associated with multiple sclerosis and cardiac ischemia.[31,32] Further development and utilization of DESI-MS should allow for an increased use of this technology for a larger breadth of clinical applications outside of cancer diagnosis.

1.3 RESEARCH AIMS

While ambient ionization MS imaging technologies have undergone significant development and improvement since their inception, limitations in their capabilities have hampered their use for many clinical applications. Further understanding and advanced modifications of ambient ionization MS methods to increase the reliability, sensitivity, and specificity of will improve the likelihood of these technologies being implemented in the clinic. Within this goal, my research has been focused on integrating ambient ionization techniques with various separation, ionization, and activation methods to develop methods for using ambient ionization for novel applications. The main objectives were to ensure DESI-MS data is reliable under fluctuating ambient conditions, coupling multiple ambient ionization methods to gas phase separations to improve ion selectivity, and integrate high energy activation methods into a DESI workflow for in depth lipid characterization. Finally, I employed DESI-MS imaging to increase the

biological understanding of endometriosis, a benign gynecological condition with severe health impacts for patients.

1.3.1 Effects of humidity on DESI-MS data quality

While DESI-MS is termed an ambient ionization MS technique and can hypothetically be applied in an open-air environment, atmospheric conditions that vary by location can have detrimental affects on the performance of the ionization method. As MS imaging data interpretation and analysis relies heavily on relative abundance measurements, stability and consistency of the DESI-MS spray system is of the utmost importance. Alterations in the performance of other ambient ionization techniques including direct analysis in real time (DART) and flowing atmospheric pressure afterglow (FAPA), regarding atmospheric temperature, pressure, and moisture have been explored, but these factors have not been evaluated for DESI-MS. Chapter 2 of my dissertation chronicles a period of time within the Eberlin laboratory during which the signal from our DESI-MS system was extremely variable and unreliable with no direct cause. Upon systematic evaluation of source and instrument parameters, the cause of the instability was attributed to the significant fluctuations in relative humidity that were occurring within the laboratory. This discovery suggests that not every environment is suitable for DESI-MS analysis and that there is much more to understand about ambient ionization techniques before they can be implemented for fieldable and clinical applications.

1.3.2 Incorporating gas-phase separations into MS imaging workflows

Ambient ionization MS techniques have the advantage of untargeted analysis of small molecules from nearly any sample surface, making these methods broadly

applicable. However, this advantage is directly correlated to the major significant disadvantage of ambient ionization and MS imaging technologies: ion suppression resulting from a complex matrix. As traditional ambient ionization MS methods do not incorporate and liquid chromatographic separation of analytes prior to introduction into the mass spectrometer for analysis, all the molecules from a sample are ionization and analyzed simultaneously. This can lead to competitive ionization during the ESI process or the filling of trap-based mass analyzers with the most abundant species in a sample, resulting in lower abundance of less easily ionizable or lower abundance species. Additionally, complex matrices can contain salts and contaminants that can further suppress the ion signal from the analytes of interest, reducing the sensitivity of the mass spectrometer and resulting in higher detection limits. Due to the definition of ambient ionization MS, coupling to a traditional chromatographic separation or incorporating sample preparation steps to limits these matrix effects are not desired. Therefore, separation methods that occur post-ionization and on a micro- to millisecond time scale have been explored for increasing the sensitivity and selectivity of ambient ionization methods.

Chapter 2 of my dissertation describes the integration of two ambient ionization MS imaging techniques, DESI and liquid micro-junction surface sampling probe (LMJ-SSP), with high field asymmetric waveform ion mobility spectrometer (FAIMS) to allow for semi-selective analysis of analytes of interest during an imaging experiment. FAIMS is a gas phase separation method that allows for separation of ions based on their differential mobility, a property that is inherent to the ion and is orthogonal to the mass-to-charge ratio. Essentially, FAIMS can serve as an ion filter for certain classes of molecules by applying appropriate voltages to the device, allowing for semi-selective analysis of ions without increasing the time needed for the experiment. By coupling

FAIMS to ambient ionization MS techniques, we were able to increase the sensitivity for certain analytes from human and mice biological tissue sections, namely multiply charged complex lipids and biopolymers, while also decreasing the noise resulting from the complex matrix. Using the FAIMS integrated platforms during an imaging experiment allowed for increased contrast of the analytes to the noise within the ion images. Coupling of ambient ionization techniques to methods for gas-phase separation, as explored in this study, is a significant advance towards using these analysis tools for a wider variety of applications and analytes, therefore increasing the usefulness of these technologies for biological sample analysis.

1.3.3. In depth characterization of lipids directly correlated to histological features

DESI-MS imaging allows for detection of a wide variety of molecules in a single experiment, yielding molecular profiles that encompass a large portion of the analytes within a tissue section. The use of high resolution and high mass accuracy mass spectrometers further facilitates the molecular characterization of these tissues as they enable mass-to-charge separation of species with identical nominal mass values. However, isomers at the same exact mass cannot be deconvoluted from one another during this type of analysis and require tandem MS measurements for identification. Tandem MS, while a valuable tool for the identification of many analytes, is still limited in its ability to resolve the structure of all species. The most common activation methods for tandem MS experiments are collisional activation techniques, primarily collision induced dissociation (CID) and higher energy collisional dissociation (HCD), which rely on excitation of analytes and subsequent impaction with a collisional gas. The energy stemming from multiple collisions results in fragmentation of the labile bonds. This method is limited by this fact, as not all isomers can be identified by fragmentation of the

most fragile bonds. For example, glycerol lipid isomers can differ in the number of double bonds within each fatty acid chain, the location and the stereochemistry of the double bonds within each chain. Collisional activation can identify the number of double bonds in each chain through fragmentation of the C-O bond that connects the fatty acid to the glycerol, but no diagnostic fragments that reveal the double bond location or stereochemistry are produced. This results in a lack of complete understanding of the molecular composition of samples and how those compositions may be altered with disease.

In collaboration with Luis Macias and Dustin Klein from the research group of Prof. Jennifer Brodbelt, we have developed methods for lipid double bond characterization during DESI-MS imaging analyses by integrating with Ultraviolet Photodissociation (UVPD). UVPD is an increased energy activation method in which ultraviolet photons are absorbed by the analytes, triggering fragmentation. Fragmentation by UVPD typically results from the absorbance of one high energy photon, allowing for access to an increased number of fragmentation pathways that can often generate more informative fragments than the lower energy collisional activation methods. When lipids are subject to UVPD irradiation, fragmentation along the carbon chains of the fatty acids occurs and yields fragments that are indicative of the double bond placement. Chapter 4 of this dissertation focuses on the development of a method for online double bond characterization within free fatty acids by reactive DESI and charge remote UVPD fragmentation. This method was then applied to investigating fatty acid double bond position within histological and molecular subtypes of breast tumors, furthering the understanding of the role free fatty acids and fatty acid synthases play in the disease.

1.3.4 Use of ambient MS towards the molecular understanding of endometriosis

The final chapter of my dissertation focuses on the utilization of ambient ionization MS imaging towards the increased understanding of a disease that could greatly benefit from the advantages afforded by this technology. Endometriosis is a gynecological condition in which the endometrial tissue that typically lies the walls of the uterus grows in other areas of the abdominal cavity. This condition that affects approximately 176 million women worldwide can cause chronic severe pain and subfertility, greatly diminishing the quality of life of patients. Unfortunately, despite its prevalence and impacts, little is known about the cause of the disease and noninvasive biomarkers of the condition have yet to be discovered. MS has been used to analyze endometriosis lesions previously, but the heterogeneity of the lesions and the comorbidity of endometriosis with other ailments has prevented to detection of reliable biomarkers.

Chapter 5 outlines the use of DESI-MS imaging for the metabolic analysis of endometriosis lesions and healthy endometrium tissue to determine if there are differences between these two histologically similar tissue types. The spatial correlation of the lipids and metabolites with the histological features of the endometrial glands and stroma allowed by MS imaging yielded molecular data specific to these tissue types. The molecular data collected with DESI-MS is solely from our cell types of interest, facilitating confidence that the metabolic information collected is an accurate representation for the tissue. Comparison of the molecular composition of these tissues revealed significant differences between these tissues despite them being the exact same tissue type. Using the least absolute shrinkage and selector operator statistical method, a model utilizing the MS data was created that was capable of distinguishing eutopic and ectopic endometrial tissue with 98.8% accuracy on an independent test set. Statistical analysis also yielded identification of 34 molecular ions with significantly altered

abundances between the two grounds. Alterations in the free fatty acid, phosphatidylserine, and small metabolite abundances were observed as the primary contributors to the differences between the two classes of tissue. This study illustrates the power of DESI-MS imaging as an exploratory tool towards the understanding of disease, allowing for the analysis of precise regions of heterogeneous samples in a simple and non-destructive manner.

Chapter 2: Desorption electrospray ionization mass spectrometry imaging is dependent on relative humidity[1]

2.1 INTRODUCTION

The field of ambient ionization MS was introduced over a decade ago with the development of desorption electrospray ionization (DESI),[18] and direct analysis in real time (DART)[33] techniques, opening opportunities for MS to be used in settings where complex sample preparation and in vacuum analysis are not desired. Since then, tens of ambient ionization MS techniques have been established and applied in various research fields including drug development[34], disease analysis[23,30,35], plant biology[36], forensics[37], and others. A fundamental feature of ambient ionization MS is an open atmosphere analysis with minimal sample preparation requirements.[38] In DESI, a spray of charged microdroplets is directed towards a sample surface to desorb, ionize, and transfer molecules from the sample surface to a mass spectrometer for analysis.[18] When DESI-MS is performed in the imaging mode, two-dimensional maps of the chemical constituents are obtained, displaying the intensity and distribution of the ions throughout the surface analyzed.[39] DESI-MS imaging has been applied to a variety of samples[40,41], with exciting applications to biological tissue section imaging and disease diagnosis.[42] As such, the effects of sample handling and experimental protocols on the quality of the data obtained from biological tissue sections have been previously investigated.[43] Nevertheless, operation in an ambient environment comes with the cost of potential susceptibility to changes in environmental conditions. In particular, relative humidity

[1] Adapted with permission from "Feider, C. L.; DeHoog, R. J.; Sans, M.; Zhang, J.; Krieger, A.; Eberlin, L. S., DESI Spray Stability in the Negative Ion Mode Is Dependent on Relative Humidity. *J. Amer. Soc. Mass Spectrom.* **2019,** *30* (2), 376-380." Copyright 2019 American Chemical Society. C.L. Feider, R.J. DeHoog, M. Sans, J. Zhang, and A. Krieger assited with the collection and analysis of the data presented in this chapeter. C.L. Feider, A. Krieger, and L.S. Eberlin prepared and edited the manuscript. All authors revised the manuscript.

(RH) has been shown to impact ionization stability and efficacy in several MS techniques.[44,45] For example, the effect of RH on the mass spectra obtained using plasma-based ambient ionization sources, such as DART and flowing atmospheric pressure afterglow (FAPA), has been reported.[46,47] Newsome et al. suggested that small variations in RH that occur in a laboratory environment can lead to large variations in DART and FAPA mass spectra due to altered ion fragmentation during ionization.[48] Several studies have investigated how variations in RH alter the Taylor cone formation and ionization in electrospray ionization (ESI) sources.[49,50] Our group has observed substantial variations in spray stability during DESI-MS imaging experiments performed in the negative ion mode in our laboratory. After many attempts in source optimization followed by a systematic investigation of the potential factors leading to instability, we determined RH to be a crucial yet often overlooked factor influencing data quality in DESI-MS imaging. Here, we describe how RH affects DESI spray stability in the negative ion mode, and briefly discuss why this instability due to RH should be avoided in DESI-MS imaging.

2.2 Materials and Methods

2.2.1 Chemicals

The Pierce LTQ ESI negative ion calibration solution was used for spray stability analysis (Thermo Fisher Scientific, Waltham, MA).

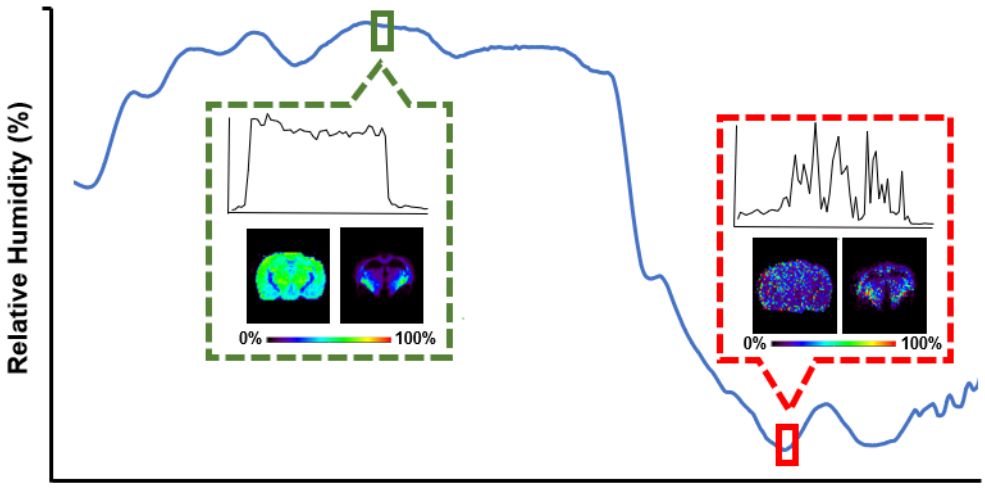

Illustration 2.1. Visual representation of the decrease in data quality with decreasing RH %.

2.2.2 Biological tissue samples

Mouse brain samples were obtained from BioIVT (Hicksville, NY). Samples were stored in a −80 °C freezer until sectioned. Tissue samples were sectioned at a thickness of 16 μm using a CryoStar NX50 cryostat (Thermo Scientific, San Jose, CA). After sectioning, the glass slides were stored in a −80 °C freezer. Prior to MS imaging, the glass slides were dried for ~15 min.

2.2.3 DESI-MS imaging parameters

A 2D Omni Spray (Prosolia Inc., Indianapolis, IN) coupled to a Q Exactive and an LTQ-Orbitrap Elite mass spectrometers (Thermo Scientific, San Jose, CA) was used for tissue profiling and imaging. DESI-MS was performed in both the negative and positive ion modes from *m/z* 100–1500 at 60,000 resolving power. The spatial resolution of the imaging experiments was 200 μm. The histologically compatible solvent system dimethylformamide/acetonitrile (DMF/ACN) 1:1 (v/v) was used for analysis at a flow rate of 1.2 μL/min, unless otherwise states, with 5 kV applied to the solvent.[21] The N_2 pressure was set to 180 psi. The capillary temperature of the mass spectrometer was set to 300 °C. Metabolite and lipid species were tentatively identified using high mass accuracy measurements, collision-induced dissociation, and high-energy collision-induced dissociation tandem MS analyses, performed using the Orbitrap as the mass analyzer of the LTQ-Orbitrap Elite mass spectrometer.

2.2.4 Monitoring of relative humidity

RH was monitored using a TP425 Dickson data logger (Addison, IL). Simulation of altered RH environments were done by enclosing the DESI imaging stage with the Dickson data logger and a cool air humidifier.

2.3 RESULTS AND DISCUSSION

2.3.1 Investigation of sporadic DESI-MS imaging data

The DESI-MS imaging experiments of mouse brain tissue sections described here were performed in the negative ion mode from October 2017 to April 2018 using optimized experimental parameters.[51] During this period, unexpected scan-to-scan variability was observed in the total ion current (TIC) chromatograms obtained on different days of analysis, as shown in Figure 2.1 for a period of 9 days from February 28 to March 8. In conjunction with TIC instability, the mass spectra obtained were inconsistent from scan-to-scan (Figure 2.2), with atypical relative abundances of metabolites and lipids species commonly detected in DESI mass spectra. Under optimized experimental conditions, the relative standard deviation (RSD) of the TIC obtained when analyzing across a single line of a mouse brain tissue section was 21.3%, resulting in chromatograms presenting a smooth pattern. The RSD calculated for the TIC under unstable conditions were significantly higher (68.6%), indicating an issue in our experiments. Furthermore, we observed that the spray stability often changed day-to-day or even hour-to-hour, despite no change in the DESI-MS source or instrument parameters. To investigate the potential causes for the inadequate DESI-MS performance, we systematically evaluated hardware and experimental conditions including DESI source optimization and mass spectrometers.

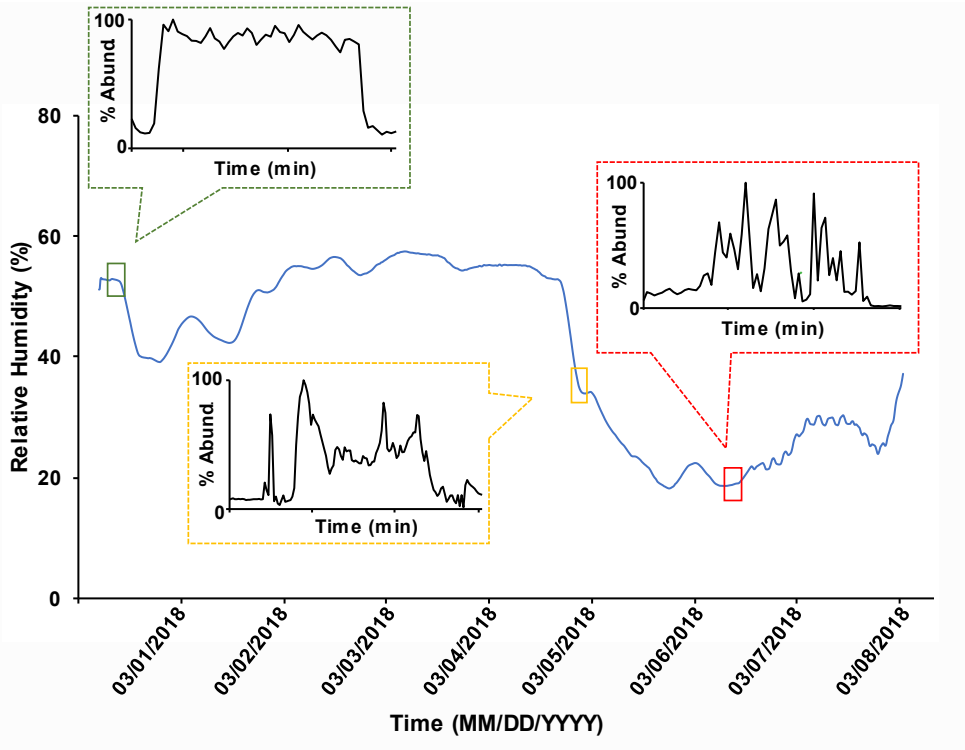

Figure 2.1. TIC plots obtained from a single line scan DESI-MS analysis of mice brain tissue sections at various RH levels.

At RH > 35% (green outline), the TIC is stable and rapidly increasing and decreasing when moving on and off the tissue sample, respectively. At RH ~ 35% (yellow outline), the TIC begins to destabilize, showing seemingly random fluctuations. At RH < 35% (red outline), the TIC plot shows large variations throughout the tissue that are indicative of DESI spray instability.

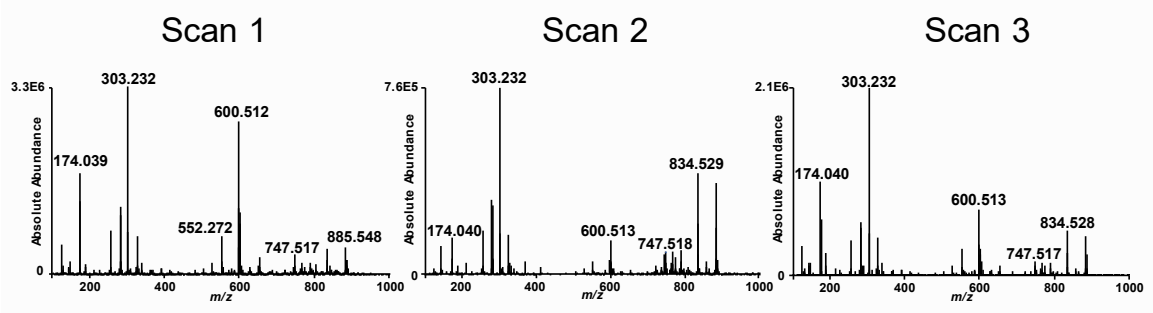

Figure 2.2. Scan-to-scan variability of the DESI mass spectra from a mouse brain tissue section during times of instability

To investigate the potential causes for the inadequate DESI-MS performance, we first evaluated if hardware issues related to the DESI source or the mass spectrometer used were present. A DESI source that was unstable on an LTQ-Orbitrap Elite mass spectrometer was transferred to an Orbitrap Q Exactive mass spectrometer in our laboratory to determine if TIC instability was related to an issue with the mass spectrometer. The instability remained, indicating the issue was not associated to instrument conditions or cleanliness. To evaluate if the source instability was caused by the DESI sprayer, we tested multiple DESI sprayers, including several lab-built sprayers and a commercial DESI sprayer, and still observed instability. To evaluate if source optimization and experimental conditions were related to signal instability, we then altered the source geometry of the DESI sprayer, the solvent flow rate and composition, the gas flow rate, and the applied voltage. The changes in source parameters that partially alleviated the TIC instability were decreasing in the voltage applied from 5 kV to 0 kV (Figures 2.3 and A.1) or increasing the solvent flow rate from 1.2 µL/min to 5 µL/min (Figure 2.4). The use of MeOH:H_2O, another very common DESI spray solvent, rather than ACN:DMF, actually decreased the stability of the spray (Figure A.2). The voltage dependence indicated that the instability observed could be related to the high electric field experienced by the charged microdroplets. However, reducing the applied voltage also decreased the TIC intensity by approximately one order of magnitude, making it challenging to determine whether lower voltage potentials alleviated the instability or reduced it due to lower signal intensity (Figure A.3). To investigate the issue further, we decoupled the ionization and desorption processes by performing reflective electrospray ionization (RESI)[52] using a standard calibration solution as the DESI spray solution. The instability remained when infusing at 5 kV but was reduced at 0 kV (Figure A.4),

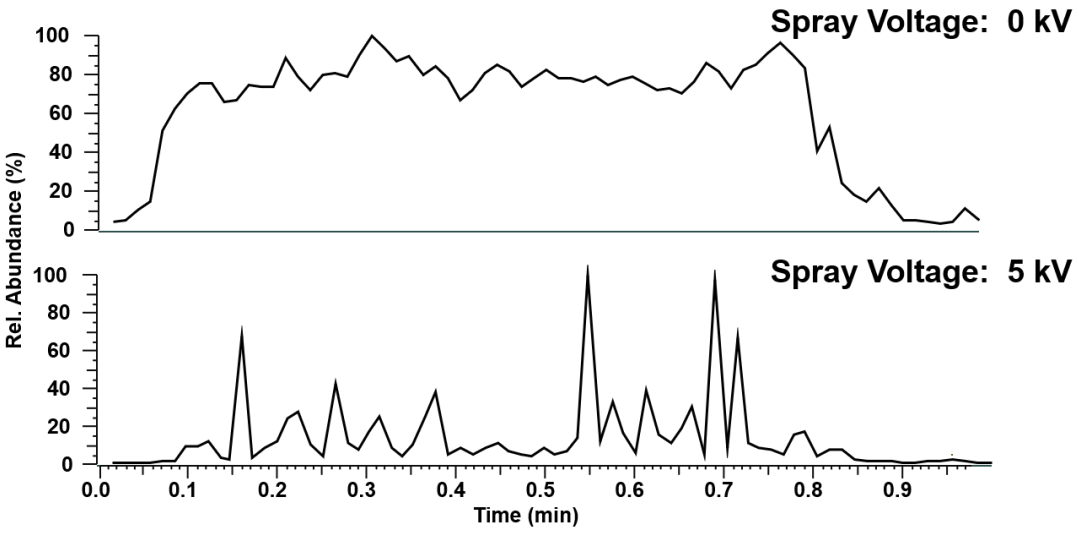

Figure 2.3. TIC variability obtained a low and high voltages

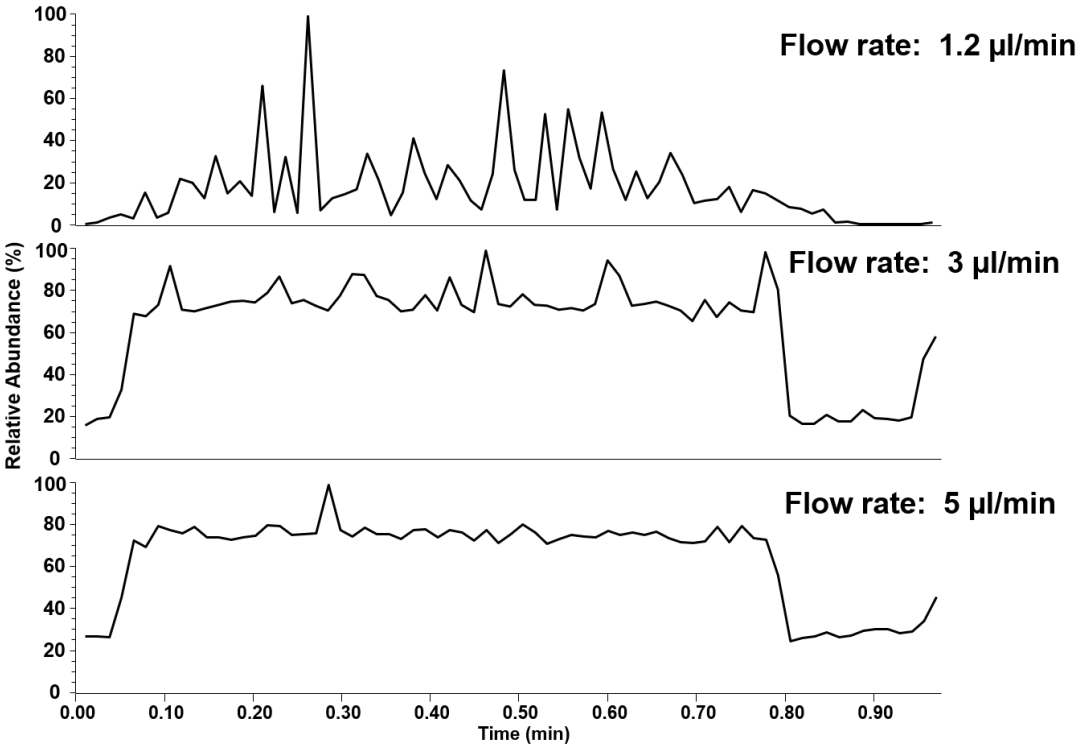

Figure 2.4. TIC variability obtained at varying solvent flow rates

suggesting that the ionization process, not desorption, was the major cause of signal instability.

2.3.2 Evaluation of relative humidity on DESI-MS data quality

This systematic evaluation of DESI and instrument parameters led to the hypothesis that the spray instability was related to an external or environmental factor. A noteworthy observation was that decreasing the voltage applied from 5 kV to 0 kV (Figures 2.3 and A.1) during a single DESI experiment appeared to alleviate spray instability, suggesting that the issue could be related to corona discharges occurring at the spray tip. Corona discharge is a common phenomenon in both negative and positive ion mode ESI, although corona discharge often onsets at higher voltages in the positive ion mode (> 5 kV) than in the negative ion mode.[53] This hypothesis is also corroborated by the alterations observed in the mass spectra, as shown in Figure 2.5A. Typical mass spectra acquired from mouse brain tissue sections using optimized DESI-MS conditions are commonly reproducible.[21,43,54] In the negative ion mode, deprotonated lipid species including *m/z* 834.528 (glycerophosphoserine (PS) 18:0_22:6) and *m/z* 885.549 (glycerophosphoinositol (PI) 18:0_20:4) are commonly observed at high relative abundances in the gray matter region of the brain, while *m/z* 888.623 (sulfatide (ST) C24:1) is commonly observed at the high relative abundance in the white matter. On the other hand, atypical mass spectra obtained during the period of experimental instability presented a higher relative abundance of chloride adducts of lipid species, specifically ceramide (Cer) d36:1 at *m/z* 600.513. The increase in chloride adducts suggests that electrical discharge may be occurring at the DESI spray tip, as chloride adduct formation is more common in plasma-based than spray-based ionization mechanisms.[55] Thus, our observations suggested that an external factor was contributing to a discharge increase,

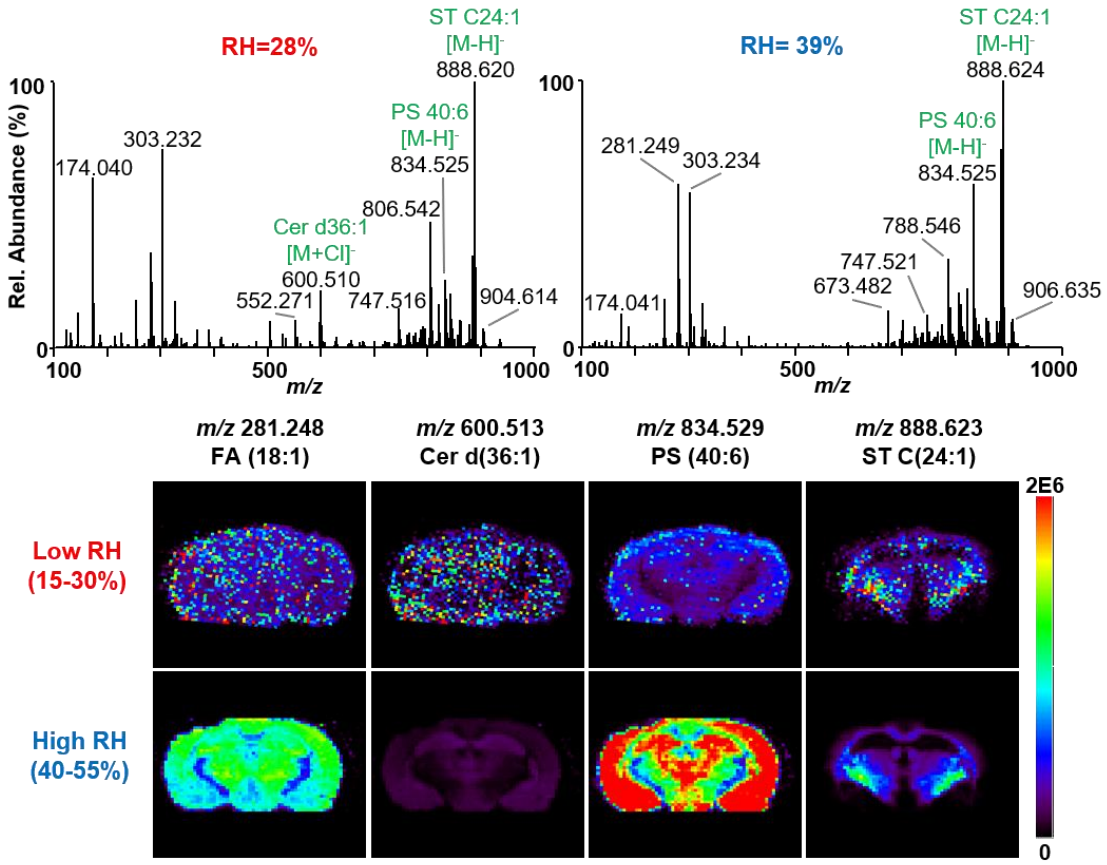

Figure 2.5. Comparison of DESI-MS imaging data at low and high RH levels.

(A) Representative mass spectra from the white matter of a mouse brain tissue section at high (39%) and low (28%) RH. Each spectrum is an average of 10 scans. (B) Representative DESI-MS ion images collected at low and high RH levels. Low humidity results in images with erratic ion distributions that are not reflective of the true molecular distribution. High humidity results in images that are consistent with what has been published in the literature

causing spray instability. Previous work has suggested that the maximum voltage that can be applied to an atmospheric pressure ESI source without inducing corona discharge is higher in summer months when atmospheric conditions are presumably more humid.[45] Therefore, we explored the possibility that the external factor affecting DESI spray stability was the RH in our laboratory.

Upon investigation of DESI-MS spray stability during times of low (~ 15–30%) and high (~ 40–55%) RH, we found a startling difference in the steadiness of the overall TIC (Figure 2.1) and the mass spectra (Figure 2.5A) depending on RH. Figure 2b shows the DESI-MS imaging results of two serial mouse brain tissue sections analyzed only 20 hrs apart at low and high RH levels, using the same mass spectrometer and nearly identical DESI source conditions and spatial resolution. As expected from the large variations in the TIC and mass spectra patterns in low-RH conditions, the DESI ion images acquired at low RH conditions were not in agreement with the lipid distributions commonly seen in mouse brain tissue, which have been extensively reported in the literature using various ionization methods.[54,56] At low RH, the intensity of the molecular ions spiked sporadically, resulting in spotty ion images and a higher relative intensity of the chloride adduct of (Cer) d36:1 at *m/z* 600.513. An atypical reduction in the relative abundance and total intensity for a variety of phospholipid species, including PS 18:0_22:6 and PI 18:0_20:4, was also observed. Under higher RH levels, smooth TIC as well as typical mass spectra and ion spatial distributions were observed in the DESI-MS imaging data for the mouse brain tissue, in agreement with what has been extensively reported in the literature.[39,54]

Further experiments were performed to more confidently determine that RH significantly contributes to DESI spray instability. A semi-enclosed DESI-MS chamber connected to a

humidifier and a nitrogen gas source was used to control RH levels during DESI-MS imaging experiments at constant temperature (T = 23 °C). Figure 2.6 shows the data acquired in a DESI-MS experiment within the same mouse brain tissue section, with the first TIC chromatogram taken at ~ 60% RH followed by a purge of the humid air with N_2 gas to acquire the second TIC chromatogram at ~ 16% RH. The RSD in TIC of the scans acquired at 60% RH was 3.3%, while an RSD of 23.6% was calculated from the data collected at 16% RH. Note that these RSD values are lower than those reported when the DESI system is not enclosed, suggesting that there is a difference in running these experiments in an enclosed system compared to the open environment. However, these results still suggest an increase in DESI spray instability due to RH levels. To further evaluate the relationship between DESI signal stability and RH, we plotted the RSD between TIC values collected at five RH ranges, 10–20%, 20–30%, 30–40%, 40–50%, and 50–60%, for the same regions of mouse brain tissue sections (Figure 2.7) using the semi-enclosed chamber. These data show that the RSD of the TIC is higher and more variable at lower RH than at higher RH levels, and the difference was statistically significant between the lowest and highest RH ranges investigated ($p < 0.05$). Similar experiments were conducted in the positive ion mode and as previously noted RH did not appear to have a significant impact on DESI spray stability or the acquired spectra (Figure A.5). Note that further work is needed to evaluate the effects of even higher RH (> 70%) on DESI spray stability, as this range could not be achieved and thus investigated in our study due to the limitations in our laboratory and experimental conditions.

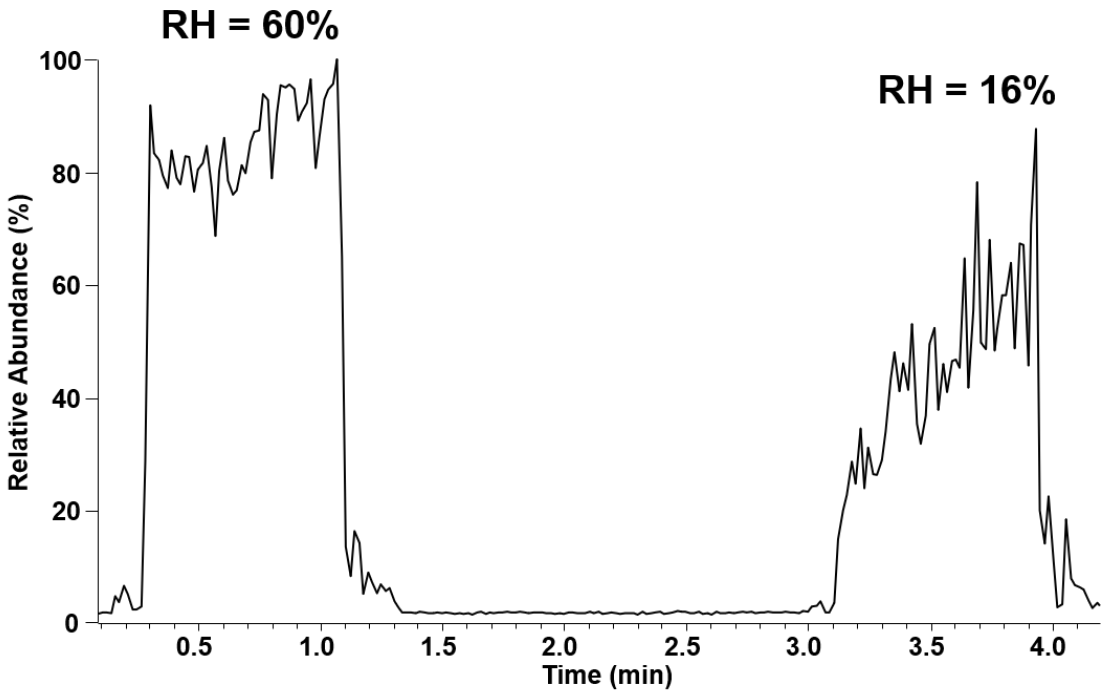

Figure 2.6. TIC chromatograms at stable RH conditions (>40%) and unstable RH conditions (<30%).

From times 1.5-3.0 min, a semi-enclosed chamber containing the DESI source as purged with N_2. The temperature for these measurements was kept at ~23°C

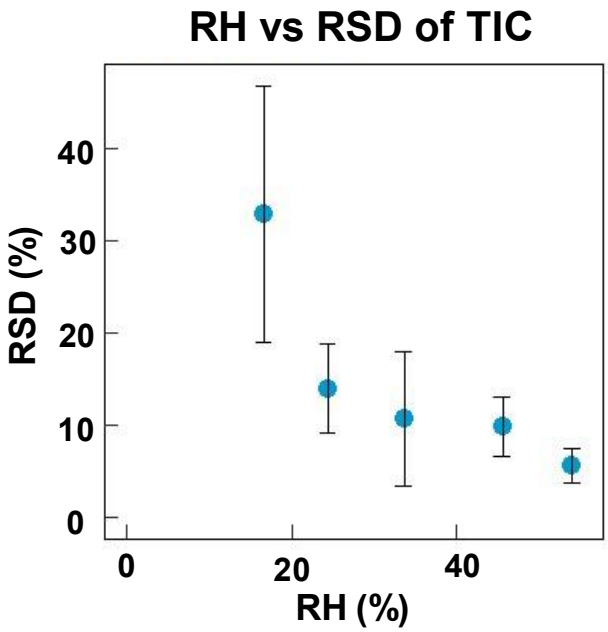

Figure 2.7. RH% vs. RSD% of the TIC at five RH% ranges.

10– 20% (n = 4), 20–30% (n = 6), 30–40% (n = 9), 40–50% (n = 4), and 50–60% (n = 10). Both the average RSD and the RSD variance for the 10–20% and 50–60% ranges were significantly different from each other ($p < 0.05$), suggesting there are observable and noteworthy differences in the stability of DESI depending on RH%. An average of eight scans were used for each recorded RH value. T tests were performed using unequal variance assumptions.

2.4 CONCLUSIONS

We have performed a study to evaluate the causes of signal instability in optimized DESI-MS experiments and have determined that DESI spray stability is dependent on RH levels in the negative ion mode under the experimental conditions evaluated. Under low-humidity conditions (~ 15–30%), negative ion mode DESI mass spectra were prone to spray artifacts resulting in atypical ion abundances and inaccurate spatial distributions, while stable and typical mass spectra were obtained in RH levels of 35–60%. Our data suggest that signal instability could be due to corona discharges occurring at the DESI spray under low-humidity conditions, although this hypothesis is not fully confirmed. As a primary goal of DESI-MS imaging is to obtain reproducible and spatially accurate mass spectral data from tissue sections, the reduction in data quality associated with low-RH conditions is noteworthy. Further, as DESI-MS imaging is often used to qualitatively evaluate trends in mass spectra patterns that allow disease diagnosis and statistical classification,[42] attention to this matter is important. Special consideration should be given in winter months when RH is typically lower, which was the case in our study, as buildings may not have advanced humidity control infrastructure to adjust for drastic local weather fluctuations. Thus, based on the data presented here, we suggest that RH conditions should be monitored and maintained at levels of 35–60% RH to favor the acquisition of high quality and reliable negative ion mode DESI-MS data.

Chapter 3: Ambient ionization and field asymmetric ion mobility mass spectrometry for enhanced imaging of multiply charged molecular ions in biological tissues[2]

3.1 INTRODUCTION

Mass spectrometry (MS) imaging provides the outstanding ability of probing the spatial distribution of molecules in a sample surface with high specificity and sensitivity.[57-59] In particular, ambient ionization MS imaging techniques have revolutionized the means by which spatial and molecular information is obtained from biological samples by enabling in situ, real time analysis of tissue samples with minimal pretreatment.[38,60] Desorption electrospray ionization (DESI) is the most commonly used solvent-based ambient ionization MS technique to image and characterize lipids and metabolites in biological tissue samples.[18,39] DESI has been increasingly applied for cancer diagnosis with the perspective of clinical use.[42] In addition to DESI, other solvent-based ambient ionization techniques have been used to analyze biological tissue samples, including liquid microjunction surface sampling probe (LMJ-SSP)[61] and nanoDESI.[62,63] Despite providing a wealth of chemical and spatial information, inherent challenges of sample complexity using direct analysis by MS imaging have prevented comprehensive detection and characterization of molecular species.[61,63] Naturally occurring lipids, for example, present enormous diversity of molecular structures and are observed over a relatively narrow mass-to-charge (*m/z*) range as molecular ions. Isobaric interferences in the mass spectrum complicate tandem MS analysis for structural characterization and

[2] Adapted with permission from "Feider, C. L.; Elizondo, N.; Eberlin, L. S., Ambient Ionization and FAIMS Mass Spectrometry for Enhanced Imaging of Multiply Charged Molecular Ions in Biological Tissues. *Analytical Chemistry* **2016,** *88* (23), 11533-11541" Copyright 2016 American Chemical Society. C.L. Feider contributed to the collection and analysis of data and preparation of the manuscript. N. Elizondo assited in the collection of data. L.S. Eberlin assited in the preparation and editing of the manuscript. All authors revised the manuscript.

obscures visualization of an ion's spatial distribution,[64] an issue that has been previously addressed through MS/MS imaging.[65] Lipids present in high concentration in biological tissues may also suppress the detection of other lipids at lower abundances.[66] Protein imaging directly from biological samples is also an ongoing analytical challenge for ambient ionization techniques, although recent progress has been made.[67] New approaches that integrate several analytical strategies are needed for improved imaging and characterization of molecules within biological tissue samples.[68,69] Ion mobility has been increasingly applied to overcome issues in complex sample analysis by MS.[70-72] In particular, high-field asymmetric waveform ion mobility spectrometry (FAIMS), or differential mobility separation, separates gas phase ions at atmospheric pressure on the basis of differences in their mobilities in electric fields prior to MS analysis.[73] A high-frequency, asymmetric waveform is employed by alternating low and high electric fields perpendicular to the path through which the ions travel.[74] This waveform, called the dispersion field (DF), causes the ions to be displaced from their initial trajectories, collide with the electrode walls, and be dissipated. However, a second, smaller DC voltage can be applied between the two electrode plates, creating a low-energy electric field that is superimposed on the DF. This compensation field (CF) counteracts the ion drift caused by the DF, allowing ions with specific mobilities to be transmitted for mass analysis. The high-speed gas phase separation provided by FAIMS has been shown to reduce chemical noise and to improve signal-to-noise ratios (S/N), sensitivity, and dynamic range.[73] By optimizing the DF and CF, semi-selective transmission of subsets of ions or classes of molecules can be achieved. The filtering capability of FAIMS allows only subsets of ions to enter and fill the mass analyzer, resulting in higher sensitivity in their detection. Several groups have explored the use of FAIMS, as well as other ion mobility techniques, for MSI applications.[75-79] A lab-built DMS cell integrated with a DESI platform was used

to image glycerophosphocholines (PC) in a mouse brain tissue, resulting in decreased chemical noise, as well as improved S/N and image contrast.[80] More recently, liquid extraction surface analysis (LESA) was integrated with the FAIMS device we applied in our study to image proteins in mouse brain and liver tissue samples.[81,82] Using the integrated LESA-FAIMS approach, 26 protein species in mouse brain and 29 protein species in mouse liver undetectable through LESA alone were observed.[82] Here, we report an analytical approach coupling DESI or LMJ-SSP with FAIMS to image and characterize lipids and proteins from biological tissue sections. In our study, we integrated and optimized a chip-based, high-speed ultraFAIMS device with DESI-MS/LMJ-SSP-MS and a high mass resolution mass spectrometer to image and characterize singly charged metabolites, singly- and doubly charged glycerophospholipids (GP) and glycosphingolipids, and multiply charged proteins in rat brain, human thyroid, and human ovarian cancer tissues. 2D-FAIMS sweep experiments were performed in tandem with DESI-MS imaging using a spot-by-spot approach to explore separation voltages for specific molecular classes of lipids and metabolites in a rat brain tissue section. Static, optimized FAIMS conditions were then used for doubly charged CL and gangliosides with no increase in analysis time. Multiply charged protein ions were imaged in biological tissues using LMJ-SSP-FAIMS with enhanced analytical performance. Using this approach, we show the first example of global protein imaging in human cancerous tissue by ambient ionization MS imaging. Our results indicate that integration of FAIMS with DESI or LMJ-SSP is valuable for imaging selected molecular classes in biological tissues.

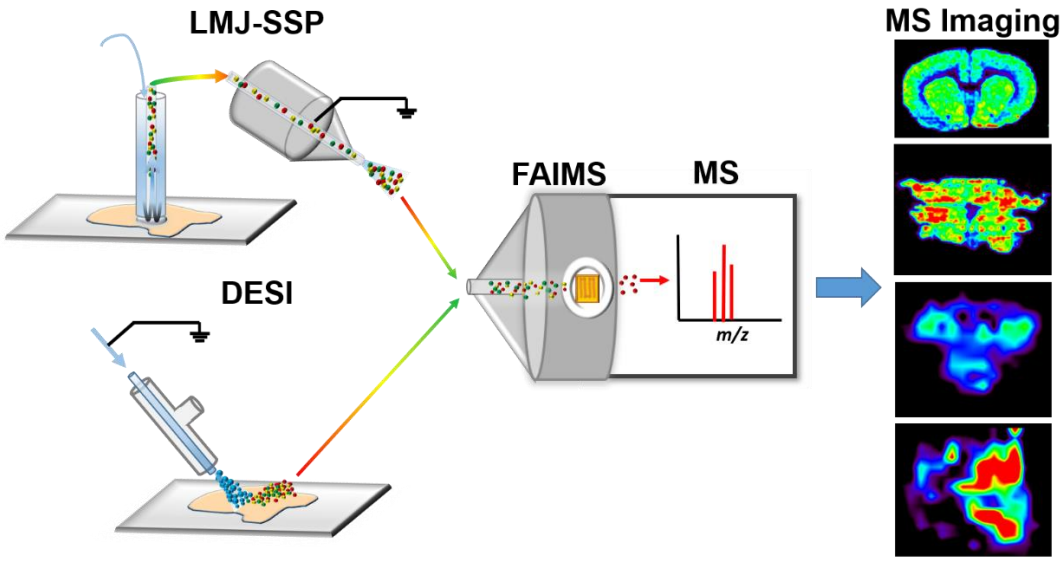

Illustration 3.1. Scheme of the integration of LMJ-SSP and DESI integrated with an ultraFAIMS system for improved MS imaging of biological tissues

3.2 MATERIALS AND METHODS

3.2.1 Chemicals

18:1 glycerophosphoinositol (PI), 18:1 glycerophosphoserine (PS), 18:1 glycerophosphoethanolamine (PE), 18:1 glycerophosphoglycerol (PG), 18:1 glycerophosphatidic acid (PA), 18:1 cardiolipin (CL), and a total ganglioside extract were purchased from Avanti Polar Lipids (Alabaster, AL). Fatty acids (FA) including oleic acid, lignoceric acid, and arachidonic acid, as well as metabolites n-acetylaspartic acid (NAA) and 2-hydroxyglutarate were purchased from Sigma-Aldrich (St. Louis, MO). Standards were dissolved in chloroform/methanol ($CHCl_3$/MeOH) 1:1 (v/v) at a concentration of 10 μg/mL. A ubiquitin standard (Sigma-Aldrich, St. Louis, MO) was dissolved in acetonitrile/water (ACN/H_2O) 60:40 (v/v) with 0.1% formic acid at 1 μg/mL. Direct electrospray ionization (ESI) infusion of the standards was performed at a flow rate of 5 μL/min.

3.2.2 Biological tissue samples

Rat brain samples were obtained from BioreclamationIVT (Hicksville, NY). Banked frozen human tissue samples including human thyroid oncocytic tumor, ovarian cancer, and normal ovarian tissues were obtained from Cooperative Human Tissue Network (CHTN) under approved IRB protocol. Samples were stored in a −80 °C freezer until sectioned. Tissue samples were sectioned at a thickness of 16 μm using a CryoStar NX50 cryostat (Thermo Scientific, San Jose, CA). After sectioning, the glass slides were stored in a −80 °C freezer. Prior to MSI, the glass slides were dried for ~15 min. For protein analysis, sections were washed in ethanol for 10 s, followed by a wash in chloroform for 10 s to remove excess lipids.

3.2.3 FAIMS parameters

An ultraFAIMS device (Owlstone Ltd., Cambridge, UK) using an ND chip (Owlstone), was used for all experiments performed. The ND chip has a trench length of 97.0 μm, a gap width of 101.51 μm, and a chip thickness of 700 μm. The chip-region temperature was set to 90 °C. At this temperature, the DF can be set to any value from 0 to 280.98 Townsends (Td) and the CF from −14.84 to 14.84 Td.

3.2.4 DESI-MS imaging parameters

A 2D Omni Spray (Prosolia Inc., Indianapolis, IN) coupled to a Q Exactive mass spectrometer (Thermo Scientific, San Jose, CA) was used for tissue profiling and imaging. An unheated extended transfer tube of 5 in. with an inner diameter of 0.067 in. was lab-built to fit the FAIMS platform. DESI-MSI was performed in the negative ion mode from *m/z* 100–1500, using the Q Exactive mass spectrometer which allows for high mass accuracy (<5 ppm mass error) and high mass resolution (70,000 resolving power at *m/z* 200) measurements. The spatial resolution of the imaging experiments was 200 μm. The histologically compatible solvent system dimethylformamide/acetonitrile (DMF/ACN) 1:1 (v/v) was used for analysis at a flow rate of 1.2 μL/min with 5 kV applied to the solvent.[21] The N_2 pressure was set to 180 psi. The capillary temperature of the mass spectrometer was set to 300 °C.

3.2.5 LMJ-SSP-MS imaging parameters

An LMJ-SSP system, the Flowprobe (Prosolia Inc. Indianapolis, IN), coupled to a Q Exactive mass spectrometer (Thermo Scientific, San Jose, CA) was used for tissue profiling and imaging. LMJ-SSP-MS imaging was performed in the positive ion mode from *m/z* 250–2000, using the hybrid Quadrupole-Orbitrap mass spectrometer. The

spatial resolution of the imaging experiments was ~630 μm. The solvent system of acetonitrile/water (ACN/H_2O) 60:40 (v/v) with 0.1% formic acid was used for analysis at a flow rate of 40 μL/min, as suggested by the manufacturer (10–100 μL/min). The N_2 pressure was between 30 and 70 psi and was adjusted manually when necessary to maintain the liquid microjunction throughout experiments. Leaking of the solvent from the probe is avoided through alterations in pressure applied to the ESI source but can occur during operation. The voltage applied to the solvent within the ESI nozzle was 4 kV, and the capillary temperature of the mass spectrometer was 300 °C.

3.2.6 Tissue staining and histological evaluation

The same tissue sections analyzed by DESI-MS imaging and adjacent sections analyzed by LMJ-SSP-MS imaging were stained using standard H&E staining protocol. Pathologic evaluation was performed using light microscopy.

3.2.7 Lipid and protein identification

Lipid species were identified using high mass accuracy measurements and higher-energy collision induced dissociation (HCD) tandem MS analysis, performed on the Q Exactive at 70,000 resolving power (*m/z* 200). Lipid fragmentation patterns were compared to literature reports and used in conjunction with data from Lipidmaps database (www.lipidmaps.org) for identification. For protein identification, mass spectra from sequential profiling experiments with and without the FAIMS separation were obtained. The data was deconvoluted using the Xtract function within Xcalibur software using a S/N threshold of 3 to obtain monoisotopic masses of protein species detected during experiments. Protein species were analyzed by top-down collision induced dissociation (CID) tandem MS, performed on a hybrid LTQ-Orbitrap Elite mass spectrometer

(Thermo Scientific, San Jose, CA) at 120,000 resolving power at *m/z* 200. Protein fragmentation patterns were input into ProSight Lite software (http://prosightlite.northwestern.edu/) and compared with protein amino acid sequences that have been previously observed within the tissue types analyzed. Protein amino acid sequences were obtained from the UniProt database

3.2.8 2D imaging data analysis

Xcalibur RAW files were converted into images using FireFly data conversion software (Prosolia, Inc. Indianapolis, IN) and then uploaded into the open source imaging software packages BioMap (Novartis) or MSiReader[83] for visualization. The interpolate function within BioMap was used to smooth the pixels within the images. All images are normalized to the maximum ion intensity within all the spectra (all pixels) used to create the image.

3.3 Results and Discussion

3.3.1 Optimization of FAIMS for separation of lipids and metabolites

To evaluate FAIMS separation voltages for lipids and metabolites, a synthetic mixture of standards was prepared and analyzed using ESI and DESI in the negative ion mode. The mixture of lipids contained species from the main classes of GP commonly detected from biological tissues in the negative ion mode including singly charged PI, PS, PE, PG, and PA, doubly charged CL and gangliosides, three common FA (oleic, lignoceric, and arachidonic), and two representative metabolites, NAA and 2-hydroxyglutarate. For ESI experiments, the synthetic mixture was directly infused while a 2D FAIMS field sweep was performed in which the DF was stepped in 10 Td

increments from 150 to 280 Td with a CV sweep from −1 to +4 Td occurring at every DF value. Increasing DF causes an increase in separation efficiency while decreasing total ion current. Thus, an optimal DF was chosen as the field at which lipids and metabolites were most clearly separated in the ion chromatogram without detrimental loss of total ion current. At this selected DF value, an optimal CF for each species was chosen as the voltage at which the specific ion had a maximum total intensity. ESI experiments yielded an optimal DF of 220 Td for the highest transmittance and separation of lipids and small metabolites by FAIMS. At this DF, optimal CFs were determined for small metabolites (CF = −0.10 Td), singly charged GP (CF = 0.99 Td), singly charged FA (CF = 1.17 Td), doubly charged gangliosides (CF = 1.80 Td), doubly charged CL (CF = 2.20 Td), and triply charged gangliosides (CF = 2.71 Td), as shown in Figure 3.1. A trend in optimized CF values was observed, in which higher CF values were ideal for transmission of larger, multiply charged ions and lower CF values were more suitable for the transmission of smaller, singly charged ions. Note that while different optimized CF values allowed separation of doubly charged CL and gangliosides from singly charged GP species, separation of different subclasses of singly charged GP was not clearly observed. DESI-FAIMS optimization experiments performed on the synthetic lipid and metabolite mixture yielded similar optimized CF values for the species of interest at DF of 220 Td. For both ESI and DESI, a drop in total ion current of 1 order of magnitude or more was observed with FAIMS separation for all experiments performed. Planar FAIMS devices are known to cause an exponential decrease in ion transmission with increasing residence time within the device in order to achieve higher separation resolving power.[84] Thus, despite the short residence time associated with this chip-based device, this method is not immune to this decrease in total ion transmission. Nevertheless, further decrease of noise leads to an overall increase in the S/N for selected molecular ions.[84] Optimization of the

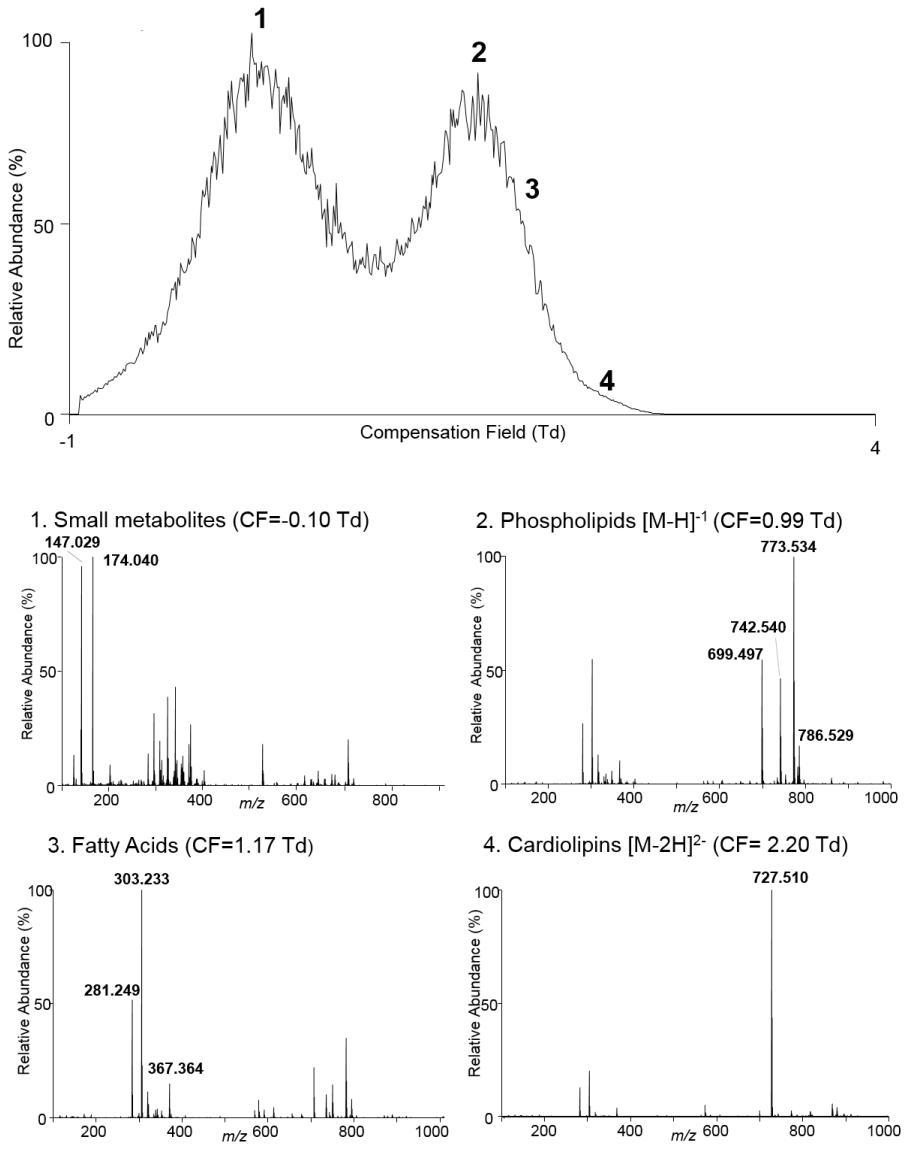

Figure 3.1. Optimization of FAIMS separation parameters for multiple lipid and metabolite classes using direct infusion.

(A) Chromatogram of a compensation field sweep (-1-4 Td) at a dispersion field of 220 Td, in which numbers annotating the peak field values for the transmission of different molecular classes of interest: metabolites, fatty acids, phospholipids, and doubly-charged species, i.e. cardiolipin (B) Spectra corresponding to the compensation field at which peak transmission of each molecular class.

DESI-FAIMS system was also performed for imaging lipids and metabolites from a tissue sample in the negative ion mode. A spot-by-spot DESI analysis of a rat brain tissue section was performed using a methodology similar to the one employed for ESI. At a spatial resolution (step size) of 200 μm, the DF was kept constant at the optimized 220 Td while a 1D FAIMS sweep (CF= −1 to 3 Td) was performed (Figure 3.2A). A total of eight mass spectra, each corresponding to a 0.5 Td CF increment, were acquired at each spot. Using this approach, a total of 6 s of analysis time was required for each spot (pixel). The spectra for each field were extracted and compiled into 2D ion images, yielding eight sets of 2D DESI-MS images at specific DF and CF values that highlight different molecular classes transmitted at the optimized voltages (Figure 3.2B). Although time-consuming, this DESI-FAIMS-MS imaging experiment allowed optimization of separation voltages for metabolites, FA, singly charged GP, doubly charged CL, and gangliosides, directly from a tissue sample. For example, preferential transmission and highest relative abundances of metabolites were observed at CF = 0 – 0.5 Td. At these parameters, clear spatial distribution of NAA, recently described as a glioma oncometabolite,[29] was observed mainly in the brain cortex. In contrast, doubly charged species (CL and gangliosides), which are difficult to image within complex biological tissue samples due to their low abundances, are nearly exclusively observed at CF= 2 – 2.5 Td. We note that a slight drop in signal intensity was observed with analysis time in each spot (Figure B.1), which could account for lower image quality for the species observed at higher CF values. At CF range 2.5–3 Td, little to no ion transmission through the FAIMS device was observed. The same optimal ion transmission voltages were obtained in replicate profiling experiments for the lipid classes investigated.

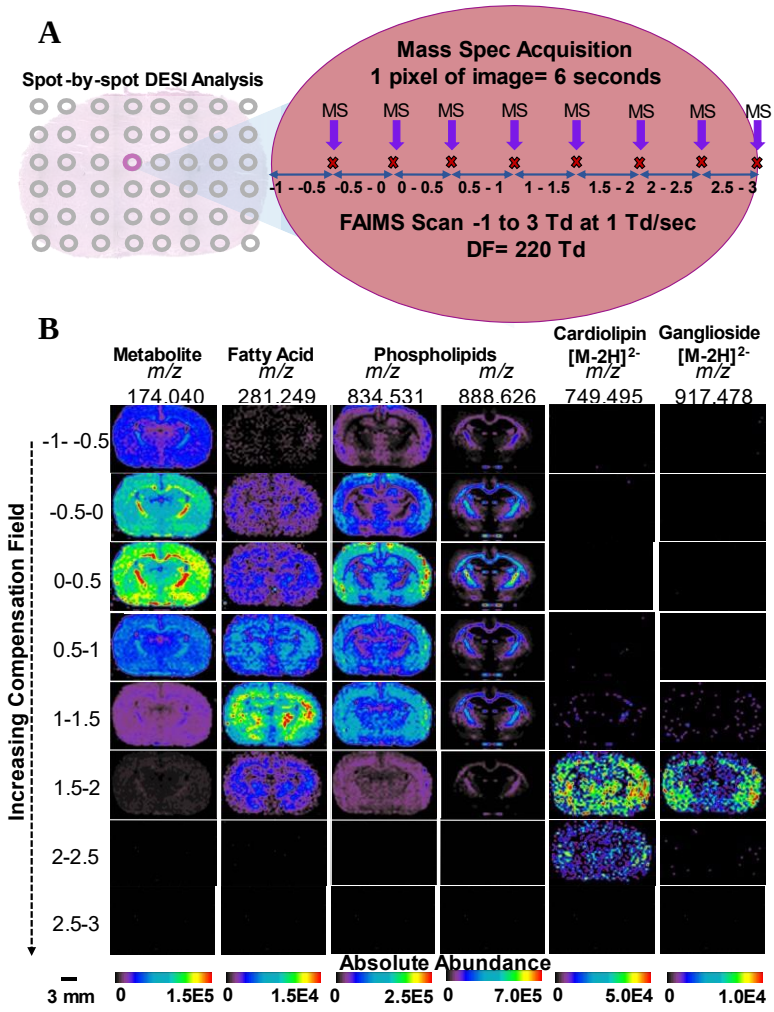

Figure 3.2. 2D-FAIMS, spot-by-spot DESI-MS imaging of a rat brain tissue section.

(A) Schematic of the 2D FAIMS sweep experiment used to create multiple sets of DESI-MS ion images at varied CF values in one tissue section. Each 200 μm spot on the tissue was analyzed for 6 s for a total of 8 MS acquisitions, in which a FAIMS sweep occurred, allowing MS acquisition correlated to different CF ranges. (B) DESI-FAIMS-MS ion images for a rat brain tissue section for 6 representative lipid and metabolite species, each acquired at DF = 220 Td and a different CF range, thus highlighting the increased transmission of different molecular species at each CF value. Small metabolites transmit at the lowest CF (−1 to +0.5 Td), followed by FA and singly charged complex lipids at midrange CF (0.5–1.5 Td), and doubly charged CL and gangliosides at the high-range CF (1.5–2.5 Td).

3.3.2 DESI-FAIMS semi-selective imaging of cardiolipins and gangliosides in rat brain sections

We further explored the DESI-FAIMS methodology for optimized imaging of doubly charged CL and gangliosides from biological tissue samples. CL are a complex class of GP that exist almost exclusively within the inner mitochondrial membrane of cells. These unique lipids are important structural and functional components of both normal and diseased tissues, and have been increasingly explored in a variety of pathologies.[85-87] We first performed DESI-FAIMS-MSI of doubly charged CL within rat brain tissue sections at the optimized FAIMS parameters in the negative ion mode. In this static FAIMS approach, both the DF and CF remain constant throughout the entire tissue imaging experiment at the optimized settings (DF = 220 Td, CF = 2.20 Td). Thus, DESI-MSI was operated in the usual rastering mode (0.5 s/pixel), without increase of analysis time, and with a spatial resolution of 200 μm. An evident increase in the S/N of CL species in comparison to other GP species was observed in the mass spectra obtained using DESI-FAIMS-MS imaging when compared to DESI-MS imaging alone (Figure 3.3). For example, using DESI-FAIMS-MS imaging, an increase in the S/N from 116 to 203 for an average of 50 spectra was observed for the most abundant CL species (*m/z* 749.495, CL (20:4_20:4_20:4_18:1), mass error of −0.93 ppm), with minimal change in absolute signal intensity (from 1.78×10^4 to 1.98×10^4), resulting in images that highlight the CL species over other GP within the tissue sample (Figures 3.3C and 3.4). MS fragmentation patterns for low abundance CL were unclear, tentative identification was based on accurate mass measurements alone. Overall, about 50% increase in the S/N was observed for all CL species detected with the DESI-FAIMS-MS imaging approach. Most importantly, an increase in the number of detectable CL species was observed with the addition of FAIMS. For example, *m/z* 797.494, identified as CL(84:18) with a mass error

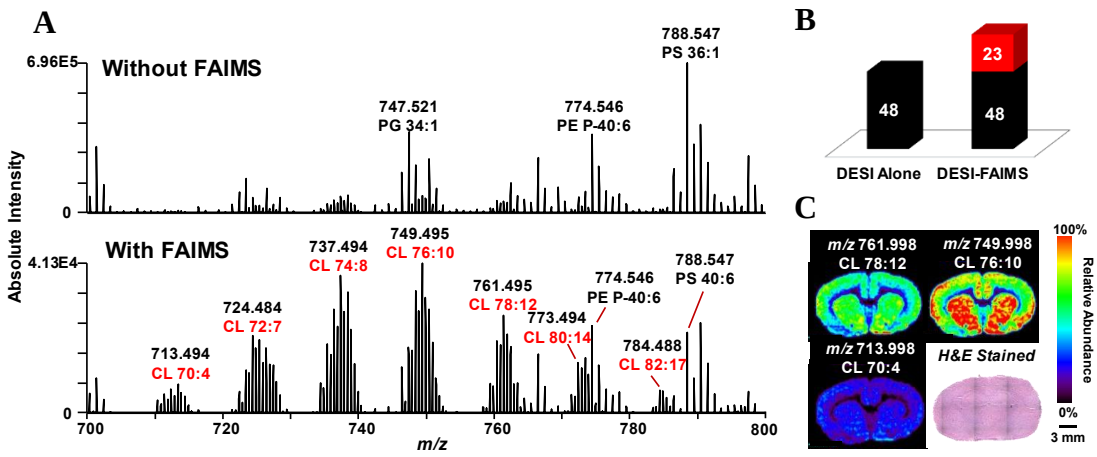

Figure 3.3. Static DESI-FAIMS-MSI of CL in rat brain tissue.

(A) Representative negative ion mode DESI mass spectra acquired without and with FAIMS in the *m/z* 700–800 range at the optimized doubly charged CL parameters (DF = 220 Td, CF = 2.20 Td), showing a clear increase in the relative abundance of CL species. Without FAIMS and with FAIMS spectra are averages of one DESI line scan, consisting of 68 and 66 scans, respectively. (B) Chart of CL species detected with DESI alone and the DESI-FAIMS integrated approach. (C) 2D DESI-FAIMS ion images for selected CL species (spatial resolution of 200 μm).

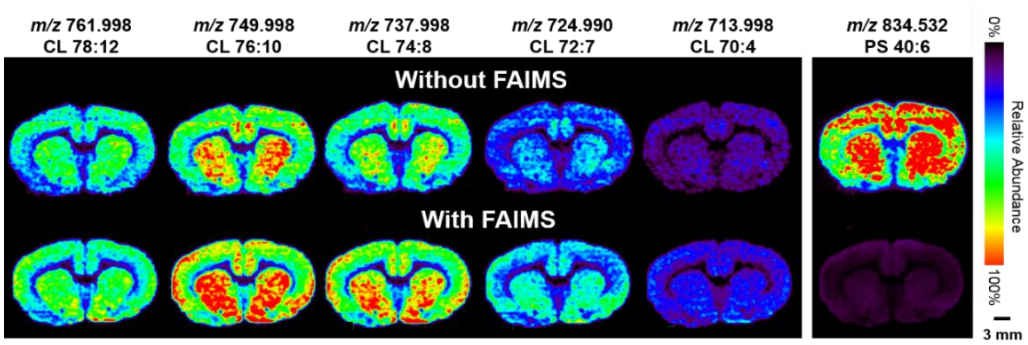

Figure 3.4. DESI-MS and DESI-FAIMS-MS ion images of rat brain tissue for five representative CL species compared to another representative lipid species.

There is an increase in relative abundance of CLs associated with FAIMS selective imaging and a significant decrease in the signal intensity from singly charged lipid species such as PS 40:6 (far right image). Scale bar= 3mm

of 1.00 ppm, was only observed by DESI-FAIMS-MS imaging and undetected with DESI-MS imaging alone. In total, 71 CL species were detected and identified using DESI-FAIMS-MS imaging, compared to 48 CL species detected when using DESI-MS imaging alone, as summarized in Table 3.1. Acyl chain composition, but not their sn position, was tentatively assigned based on tandem MS patterns, an example of which is shown in Figure B.2. When tandem MS fragmentation patterns for low abundance CL were unclear, tentative identification was based on accurate mass measurements alone.

Imaging of doubly charged gangliosides was performed using serial rat brain tissue sections at optimized FAIMS parameters (DF = 220 Td, CF = 1.8 Td) in the negative ion mode. Gangliosides are a subclass of glycosphingolipids which are most abundant within the nervous system. Gangliosides have important cellular functions, such as cell signaling and calcium homeostasis, and have been associated with multiple diseases including Alzheimer's and Tay-Sachs diseases.[88,89] DESI-FAIMS-MS imaging yielded an increased relative abundance and S/N of gangliosides compared to DESI-MS imaging alone. For example, the S/N of the most abundant ganglioside species detected, identified as trisialotetrahexosylganglioside at *m/z* 1063.530 (GT1 d36:1), doubled using FAIMS. Out of the 21 doubly charged ganglioside species detected by DESI-FAIMS-MS imaging, 7 were undetectable by traditional DESI-MS imaging (Table 3.2). Ganglioside species were identified by tandem MS experiments, an example of which is shown in Figure B.3. Gangliosides present at low relative abundances were tentatively identified by accurate mass alone. Note that while FAIMS allowed improved detection of triply charged gangliosides at CF = 2.71 Td using a standard lipid mixture, this charge state was not observed in biological tissues by DESI-FAIMS or DESI alone due to low abundance of gangliosides at this charge state under our experimental conditions.

Table 3.1. Representative CL species detected during DESI-MSI and FAIMS-DESI-MS imaging analysis of rat brain tissue.

Measured *m/z*	Exact *m/z* $[M-2H]^{2-}$	Tentative Attribution	Mass Error (ppm)[b]	Proposed Formula [M]
697.4654	697.4626	CL 68:6	-4.01	$C_{77}H_{138}O_{17}P_2$
698.4718	698.4704	CL 68:5	-2.00	$C_{77}H_{140}O_{17}P_2$
699.4803	699.4783	CL 68:4	-2.86	$C_{77}H_{142}O_{17}P_2$
700.4885	700.4861	CL 68:3	-3.43	$C_{77}H_{144}O_{17}P_2$
709.4647	709.4626	CL 70:8	-2.96	$C_{79}H_{138}O_{17}P_2$
710.4727	710.4705	CL 70:7	-3.10	$C_{79}H_{140}O_{17}P_2$
711.4796	711.4783	CL 70:6	-1.83	$C_{79}H_{142}O_{17}P_2$
712.4876	712.4861	CL 70:5	-2.11	$C_{79}H_{144}O_{17}P_2$
713.4955	713.4939	CL 70:4	-2.24	$C_{79}H_{146}O_{17}P_2$
714.5012	714.5018	CL 70:3	0.84	$C_{79}H_{148}O_{17}P_2$
715.5065	715.5096	CL 70:2	4.33	$C_{79}H_{150}O_{17}P_2$
717.4803	717.4783	CL 71:7	-2.79	$C_{80}H_{142}O_{17}P_2$
718.489	718.4861	CL 71:6	-4.04	$C_{80}H_{144}O_{17}P_2$
719.4963	719.4940	CL 71:5	-3.20	$C_{80}H_{146}O_{17}P_2$
720.5048	720.5018	CL 71:4	-4.16	$C_{80}H_{148}O_{17}P_2$
721.4654	721.4626	CL 72:8	-3.88	$C_{81}H_{138}O_{17}P_2$
722.4727	722.4705	CL 72:7	-3.05	$C_{81}H_{140}O_{17}P_2$
723.4806	723.4783	CL 72:6	-3.18	$C_{81}H_{142}O_{17}P_2$
724.4878	724.4861	CL 72:5	-2.35	$C_{81}H_{144}O_{17}P_2$
725.4943	725.4939	CL 72:4	-0.55	$C_{81}H_{146}O_{17}P_2$
726.5029	726.5018	CL 72:3	-1.51	$C_{81}H_{148}O_{17}P_2$
727.5103	727.5096	CL 72:2	-0.96	$C_{81}H_{150}O_{17}P_2$
728.516	728.5174	CL 72:1	1.92	$C_{81}H_{152}O_{17}P_2$
729.4827	729.4783	CL 73:9	-6.03	$C_{82}H_{142}O_{17}P_2$
729.5254	729.5252	CL 72:0	-0.27	$C_{81}H_{154}O_{17}P_2$
730.4873	730.4861	CL 73:8	-1.64	$C_{82}H_{144}O_{17}P_2$
731.4947	731.4939	CL 73:7	-1.09	$C_{82}H_{146}O_{17}P_2$
733.4658	733.4626	CL 74:12	-4.36	$C_{83}H_{138}O_{17}P_2$
734.4726	734.4705	CL 74:11	-2.86	$C_{83}H_{140}O_{17}P_2$
735.4803	735.4783	CL 74:10	-2.72	$C_{83}H_{142}O_{17}P_2$
736.4874	736.4861	CL 74:9	-1.77	$C_{83}H_{144}O_{17}P_2$
737.4956	737.4939	CL 74:8	-2.31	$C_{83}H_{146}O_{17}P_2$

Table 3.1. (cont.)

Measured *m/z*	Exact *m/z* $[M-2H]^{2-}$	Tentative Attribution	Mass Error (ppm)[b]	Proposed Formula [M]
738.5032	738.5018	CL 74:7	-1.90	$C_{83}H_{148}O_{17}P_2$
739.5087	739.5096	CL 74:6	1.22	$C_{83}H_{150}O_{17}P_2$
740.5154	740.5174	CL 74:5	2.70	$C_{83}H_{152}O_{17}P_2$
741.5216	741.5252	CL 74:4	4.85	$C_{83}H_{154}O_{17}P_2$
742.4877	742.4861	CL 75:10	-2.15	$C_{84}H_{144}O_{17}P_2$
746.4734	746.4705	CL 76:13	-3.88	$C_{85}H_{140}O_{17}P_2$
747.4812	747.4783	CL 76:12	-3.88	$C_{85}H_{142}O_{17}P_2$
748.4878	748.4861	CL 76:11	-2.27	$C_{85}H_{144}O_{17}P_2$
749.4952	749.4939	CL 76:10	-1.73	$C_{85}H_{146}O_{17}P_2$
750.5020	750.5017	CL 76:9	-0.40	$C_{85}H_{148}O_{17}P_2$
751.5093	751.5096	CL 76:8	0.40	$C_{85}H_{150}O_{17}P_2$
752.5164	752.5174	CL 76:7	1.33	$C_{85}H_{152}O_{17}P_2$
753.5249	753.5252	CL 76:6	0.40	$C_{85}H_{154}O_{17}P_2$
754.4879	754.4861	CL 77:9	-2.39	$C_{86}H_{144}O_{17}P_2$
755.4946	755.4939	CL 77:8	-0.93	$C_{86}H_{146}O_{17}P_2$
758.4722	758.4705	CL 78:15	-2.24	$C_{87}H_{140}O_{17}P_2$
759.4800	759.4783	CL 78:14	-2.24	$C_{87}H_{142}O_{17}P_2$
760.4874	760.4861	CL 78:13	-1.71	$C_{87}H_{144}O_{17}P_2$
761.4949	761.4939	CL 78:12	-1.31	$C_{87}H_{146}O_{17}P_2$
762.5031	762.5018	CL 78:11	-1.70	$C_{87}H_{148}O_{17}P_2$
763.5108	763.5096	CL 78:10	-1.57	$C_{87}H_{150}O_{17}P_2$
764.5217	764.5174	CL 78:9	-5.62	$C_{87}H_{152}O_{17}P_2$
765.5277	765.5252	CL 78:8	-3.27	$C_{87}H_{154}O_{17}P_2$
770.4733	770.4705	CL 80:17	-3.63	$C_{89}H_{140}O_{17}P_2$
771.4806	771.4783	CL 80:16	-2.98	$C_{89}H_{142}O_{17}P_2$
772.4886	772.4861	CL 80:15	-3.24	$C_{89}H_{144}O_{17}P_2$
773.4950	773.4939	CL 80:14	-1.42	$C_{89}H_{146}O_{17}P_2$
774.5007	774.5017	CL 80:13	1.29	$C_{89}H_{148}O_{17}P_2$
775.5109	775.5096	CL 80:12	-1.68	$C_{89}H_{150}O_{17}P_2$
776.5178	776.5174	CL 80:11	-0.52	$C_{89}H_{152}O_{17}P_2$
777.5264	777.5252	CL 80:10	-1.54	$C_{89}H_{154}O_{17}P_2$
783.4798	783.4783	CL 82:18	-1.91	$C_{91}H_{142}O_{17}P_2$
784.4882	784.4861	CL 82:17	-2.68	$C_{91}H_{144}O_{17}P_2$
785.4935	785.4939	CL 82:16	0.51	$C_{91}H_{146}O_{17}P_2$
786.4991	786.5018	CL 82:15	3.43	$C_{91}H_{148}O_{17}P_2$

Table 3.1. (cont.)

Measured *m/z*	Exact *m/z* $[M-2H]^{2-}$	Tentative Attribution	Mass Error (ppm)[b]	Proposed Formula [M]
795.4814	795.4783	CL 84:20	-3.90	$C_{93}H_{142}O_{17}P_2$
796.4873	796.4861	CL 84:19	-1.51	$C_{93}H_{144}O_{17}P_2$
797.4937	797.4939	CL 84:18	0.25	$C_{93}H_{146}O_{17}P_2$
798.4994	798.5018	CL 84:17	3.01	$C_{93}H_{148}O_{17}P_2$

[a] Red text denotes species that were only detectable with the addition of FAIMS with DESI-MSI [b] Calculated based on the exact monoisotopic *m/z* of the deprotonated molecular ion.

Table 3.2. Representative ganglioside species detected during DESI-MS imaging and FAIMS-DESI-MS imaging analysis of rat brain tissue and identified using high mass accuracy and tandem MS analyses.

Measured *m/z*	**Exact *m/z***	**Tentative Attribution[b]**	**Mass Error (ppm)[c]**	**Proposed Formula**
917.4798	917.4782	GD1 d36:2 $[M-2H]^{2-}$	-1.74	$C_{84}H_{148}N_4O_{39}$
918.4832	918.4860	GD1 d36:1 $[M-2H]^{2-}$	3.05	$C_{84}H_{150}N_4O_{39}$
919.4886	919.4939	GD1 d36:1 $[M-2H]^{2-}$	5.76	$C_{84}H_{152}N_4O_{39}$
931.4957	931.4939	GD1 d38:1 $[M-2H]^{2-}$	-1.93	$C_{86}H_{152}N_4O_{39}$
932.4993	932.5017	GD1 d38:0 $[M-2H]^{2-}$	2.57	$C_{86}H_{154}N_4O_{39}$
952.5009	952.4991	Acetylated GD1b d38:1 $[M-2H]^{2-}$	-1.89	$C_{88}H_{154}N_4O_{40}$
1063.0278	1063.0259	GT1 d36:1 $[M-2H]^{2-}$	-1.79	$C_{95}H_{165}N_5O_{47}$
1064.0313	1064.0338	GT1 d36:0 $[M-2H]^{2-}$	2.35	$C_{95}H_{167}N_5O_{47}$
1073.0093	1073.0103	GT1 d38:4 $[M-2H]^{2-}$	0.93	$C_{97}H_{161}N_5O_{47}$
1074.0175	1074.0181	GT1 d38:3 $[M-2H]^{2-}$	0.56	$C_{97}H_{163}N_5O_{47}$
1075.0205	1075.0259	GT1 d38:2 $[M-2H]^{2-}$	5.02	$C_{97}H_{165}N_5O_{47}$
1077.0433	1077.0416	GT1 d38:1 $[M-2H]^{2-}$	-1.58	$C_{97}H_{169}N_5O_{47}$
1078.0454	1078.0494	GT1 d38:0 $[M-2H]^{2-}$	3.71	$C_{97}H_{171}N_5O_{47}$
1082.0055	1082.0039	GT1 d36:1- Potassium adduct $[M-3H+K]^{2-}$	-1.48	$C_{95}H_{165}N_5O_{47}$
1083.0168	1083.0117	GT1 d36:0- Potassium adduct $[M-3H+K]^{2-}$	-4.71	$C_{95}H_{167}N_5O_{47}$
1084.0323	1084.0312	Acetylated GT1 d36:1 $[M-2H]^{2-}$	-1.01	$C_{97}H_{167}N_5O_{48}$
1085.0360	1085.0390	Acetylated GT1 d36:0 $[M-2H]^{2-}$	2.76	$C_{97}H_{169}N_5O_{48}$
1096.0210	1096.0195	GT1 d38:1- Potassium adduct $[M-3H+K]^{2-}$	-1.37	$C_{97}H_{169}N_5O_{47}$
1097.0294	1097.0273	GT1 d38:0- Potassium adduct $[M-3H+K]^{2-}$	-1.91	$C_{97}H_{171}N_5O_{47}$
1098.0490	1098.0466	Acetylated GT1 d38:1 $[M-2H]^{2-}$	-2.19	$C_{99}H_{171}N_5O_{48}$
1099.0496	1099.0547	Acetylated GT1 d38:0 $[M-2H]^{2-}$	4.64	$C_{99}H_{173}N_5O_{48}$

[a] Red text denotes species that were only detectable with the addition of FAIMS with DESI-MS imaging

[b] (X:Y) denotes the total number of carbons and doubles bonds within the steric acid and sphingosine chains

[c] Calculated based on the exact monoisotopic *m/z* of the deprotonated molecular ion.

3.3.3 DESI-FAIMS-MS imaging of cardiolipins in human oncocytic thyroid tumors

We have recently described a diverse group of CL as molecular markers of oncocytic thyroid tumors, including oxidized CL, adducts of CL and PC, and monolysocardiolipins.[27] However, many of the diagnostic CL are detected at low relative abundances and within close *m/z* values to other interfering GP, which complicates ion isolation for tandem MS experiments, obscures visualization of their 2D distribution, and adds complexity to data analysis. Thus, we applied the integrated DESI-FAIMS-MS imaging approach to improve imaging of CL in oncocytic thyroid tumors. Two serial sections from an oncocytic thyroid tumor were subjected to DESI-MSI under identical conditions in the negative ion mode, one with static mode FAIMS at the optimized CL voltages, and one without FAIMS separation. As shown in Figure 3.5A, DESI-FAIMS-MS imaging allowed enhanced detection of CLs within the oncocytic thyroid tumor tissue section with reduced interference from other GP in the *m/z* 700–800 range. For example, using DESI-MS imaging alone, PE(O-38:5) at *m/z* 750.545 had a signal intensity 4 times that of the doubly charged CL(76:9) at *m/z* 750.502. When FAIMS is applied, CL(76:9) had a signal intensity double that of PE(O-38:5), which facilitates ion isolation, fragmentation, identification, and visualization of its 2D distribution. DESI-FAIMS-MS imaging revealed high relative abundance of CL within the entire thyroid tissue section, as shown in Figure 3.5B for *m/z* 723.479, *m/z* 737.494, and *m/z* 747.473 identified as CL(18:2_18:2_18:2_18:2 and/or 20:4_18:2_18:2_16:0), CL(20:4_18:2_18:1_18:1, 20:3_18:2_18:2_18:1, 20:2_18:2_18:2_18:2) and CL(22:6_20:4_18:2_16:0), respectively. These results indicate the presence of oncocytic thyroid tumor in the entire tissue section, which was confirmed by histopathologic evaluation of the same H&E stained tissue section.

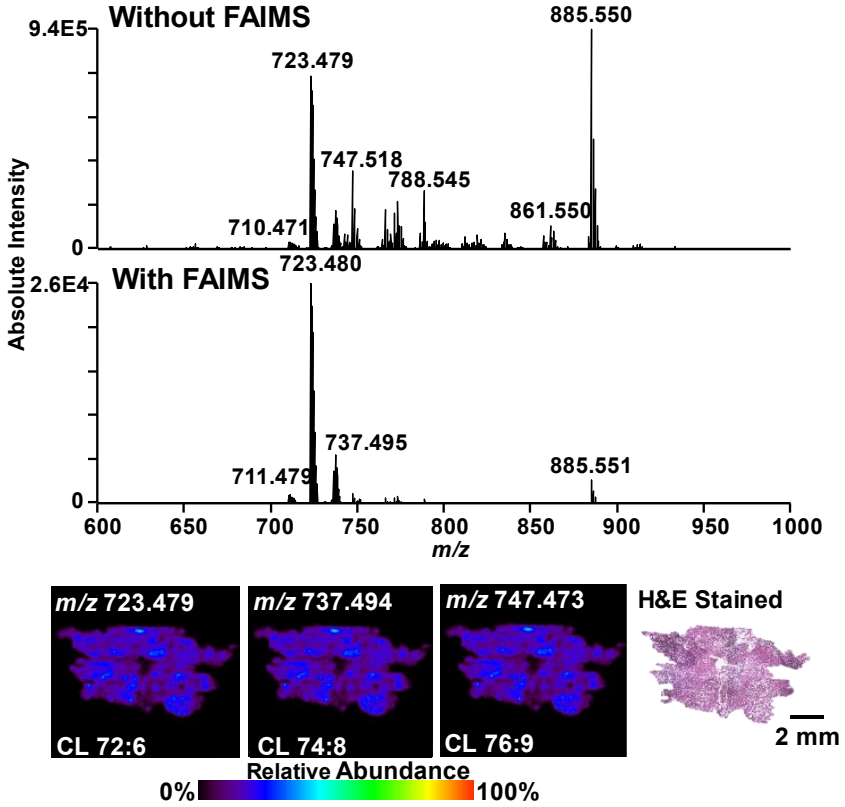

Figure 3.5. Static DESI-FAIMS-MS imaging of CLs in an oncocytic thyroid tumor tissue. (A) Representative negative ion mode DESI mass spectra acquired without and with FAIMS in the complex lipid region (*m/z* 700–900) at the optimized doubly charged CL parameters (DF = 220 Td, CF = 2.20 Td). Zoom in show spectra from *m/z* 750–752. Without FAIMS and with FAIMS spectra are averages of a DESI line scan, consisting of 57 and 54 scans, respectively. (B) DESI-FAIMS-MS ion images and optical images of the H&E stained oncocytic thyroid tumor sections for three CL species, *m/z* 723.479, *m/z* 737.494, and *m/z* 747.473, showing high relative intensities of CL, a feature of oncocytic tumors (spatial resolution of 200 μm).

3.3.4 LMJ-SSP-FAIMS-MS imaging of proteins in rat brain tissue sections

We next pursued the integration of LMJ-SSP and FAIMS for biological tissue imaging. LMJ-SSP provides similar molecular information as DESI from biological tissues with higher sensitivity yet lower spatial resolution and image quality, as limited by the probe tip diameter (~630 μm).[90] Metabolite and lipid optimization experiments performed using LMJ-SSP-FAIMS in the negative ion mode yielded similar results to those obtained by DESI-FAIMS. Yet, we found that positive ion mode LMJ-SSP-FAIMS allowed obvious improvements for imaging multiply charged protein species from biological tissue samples. Thus, we focused our efforts on evaluating and optimizing LMJ-SSP-FAIMS for protein imaging. Voltage optimization was performed for mid-mass range proteins (4–12 kDa) through LMJ-SSP-FAIMS profiling of a rat brain tissue section while conducting a 2D-FAIMS sweep from DF 230–280 Td and CF 0–4 Td. Ubiquitin, a well-known protein with a molecular weight of 8.5 kDa, was used for optimization. The highest abundance of its 10+ charge state at *m/z* 857.467 was found at DF = 220 Td and CF = 2.55 Td, and thus all static FAIMS experiments for protein imaging were performed at these settings. LMJ-SSP profiling experiments of rat brain tissue sections were performed with and without FAIMS separation in the positive ion mode under identical experimental conditions. A clear increase in the relative abundances of multiply charged protein peaks was observed in the mass spectra when FAIMS was applied at optimized voltages for protein transmission (Figure 3.6A, from *m/z* 600–1300), despite a 1 order magnitude drop in total ion current. In total, 84 species attributed to proteins and/or proteoforms were detected using LMJ-SSP-FAIMS, 66 of which were not detected by LMJ-SSP alone. For example, the protein isotope pattern for the 9+ ion at *m/z* 821.218 was clearly resolved with a S/N of 28 using LMJ-SSP-FAIMS, while undetectable above a S/N threshold of 3 with LMJ-SSP alone (Figure 3.6B). Using LMJ-

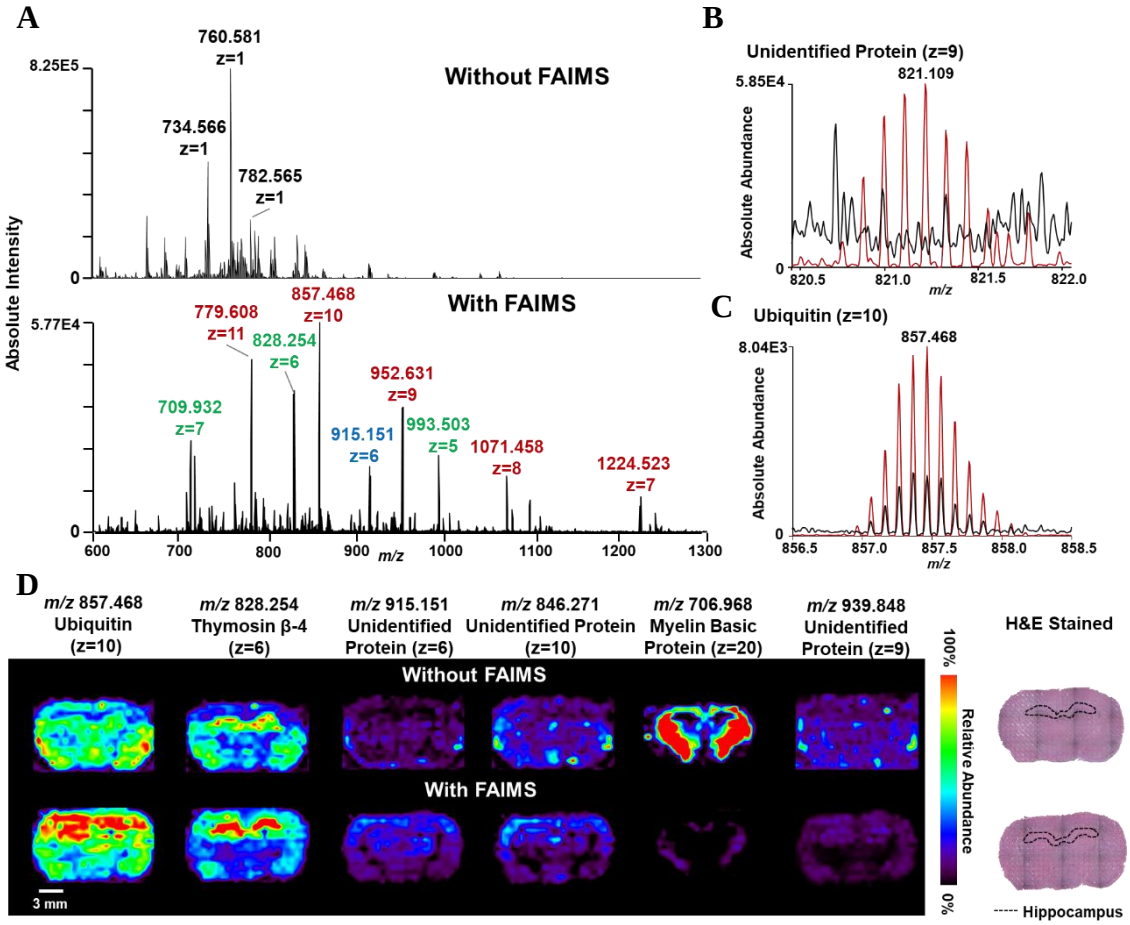

Figure 3.6. Static LMJ-SSP-FAIMS-MS profiling and imaging of rat brain tissue for protein detection.

(A) LMJ-SSP-MS spectra of a rat brain tissue section, analyzed without FAIMS and with FAIMS optimized for transmission of mid-mass range proteins (4–12 kDa). Different colored labels represent different charge states of same proteins. (B) Isotope patterns of an unidentified protein (z = 9) and (C) ubiquitin (z = 10), with (red) and without (black) FAIMS applied, showing absolute signal intensity and S/N enhancements with the addition of FAIMS. Without FAIMS and with FAIMS mass spectra are averages of a line scan, consisting of 75 scans each. (D) LMJ-SSP-MS and LMJ-SSP-FAIMS-MS ion images of rat brain tissue for six representative protein species including ubiquitin, thymosin β-4, MBP, and three unidentified proteins (spatial resolution ~630 μm).

SSP alone, 67 proteins were detected, 49 of which were not detected by LMJ-SSP-FAIMS. This effect is attributed to lower transmission of proteins with molecular weight outside of the optimized FAIMS parameters (4–12 kDa), as well as to the loss of total signal intensity associated with FAIMS.[84] Out of the six protein species detected by both approaches, four were observed at a slightly higher absolute signal intensity using FAIMS, while enhancement of S/N was observed for all six of the proteins. For example, a 7-fold increase in S/N (from 23 to 180) was observed for the 10+ ion cluster at *m/z* 857.468 when FAIMS was applied (Figure 3.6C). A list of the deconvoluted molecular weights of all protein and proteoform species detected using LMJ-SSP-FAIMS and LMJ-SSP alone is shown in Figure B.4.

In an effort to identify detected proteins, top-down CID tandem MS was performed on protein ions during rat brain tissue LMJ-SSP analysis. The 9+ charge state at *m/z* 857.370 (MW = 8559.61 Da) was identified as ubiquitin with a P-score of 8.9×10^{-53} (32% sequence coverage, Figure B.5 and Table B.1). The 6+ ions at *m/z* 828.256 (MW = 4960.48 Da) were identified as thymosin β-4 with a P-score of 2.5×10^{-11} (33% sequence coverage, Figure B.6 and Table B.2). Myelin basic protein (MBP) was tentatively attributed to the 20+ ion cluster at *m/z* 706.968 (MW = 14113.23 Da) with a P-score of 3.1×10^{-6} (21% sequence coverage). The cluster of 18+ ions at *m/z* 845.271 (MW = 15187.75 Da) was identified as hemoglobin α-1/2 with a P-score of 9.5×10^{-18} (21% sequence coverage, Figure B.7 and Table B.3). High mass accuracy measurements were used to confirm protein identity, yielding mass errors below 10 ppm for all identified protein ions

LMJ-SSP with and without FAIMS separation was performed on serial rat brain tissue sections in the positive ion mode. Figure 3.6D shows 2D ion images of selected protein species obtained using LMJ-SSP with a spatial resolution of ~630 μm. The

increase in S/N achieved with LMJ-SSP-FAIMS approach allowed for clear visualization of the spatial distribution of the proteins within the optimized transmission range. For example, the spatial distribution of the 9+ charge state of an unidentified protein (*m/z* 939.848, MW = 5449.60 Da) by LMJ-SSP alone was unclear, with signal due to protein detection and background noise observed throughout the tissue section and the surrounding glass slide. However, the LMJ-SSP-FAIMS image clearly shows protein distribution at higher relative abundances within the white matter of the rat brain. The same trend was seen for the protein detected at *m/z* 915.151. LMJ-SSP-FAIMS-MS imaging also allowed visualization of the spatial distribution of the 6+ charge state of thymosin β-4 (*m/z* 828.256) within the hippocampus of the rat brain (delineated over optical image of H&E stained tissues), while the 10+ charge state of ubiquitin (*m/z* 857.370) was distributed homogeneously throughout the tissue section. Protein distributions obtained by LMJ-SSP-MS imaging were reproducible ($n = 4$ for each approach, Figure 3.7), although small alterations in experimental parameters including pressure and probe distance to the sample slightly affected ion intensity, which most noticeably impacts ion images obtained for ions that are not localized in a specific region of the tissue. Similar spatial distributions for these proteins described have been recently reported using other ambient ionization MS imaging techniques.[67,82]

Proteins with molecular weights outside the optimized FAIMS voltages are observed at lower absolute intensities when compared to LMJ-SSP alone. For example, MBP has a molecular weight of 15 kDa which is outside the 4–12 kDa range. LMJ-SSP-FAIMS-MS imaging of its 20+ charge state at *m/z* 706.968 still allows for visualization of its spatial distribution despite a 2-fold reduction in intensity. Note that lipid ions could still be detected and imaged using the FAIMS conditions optimized from proteins,

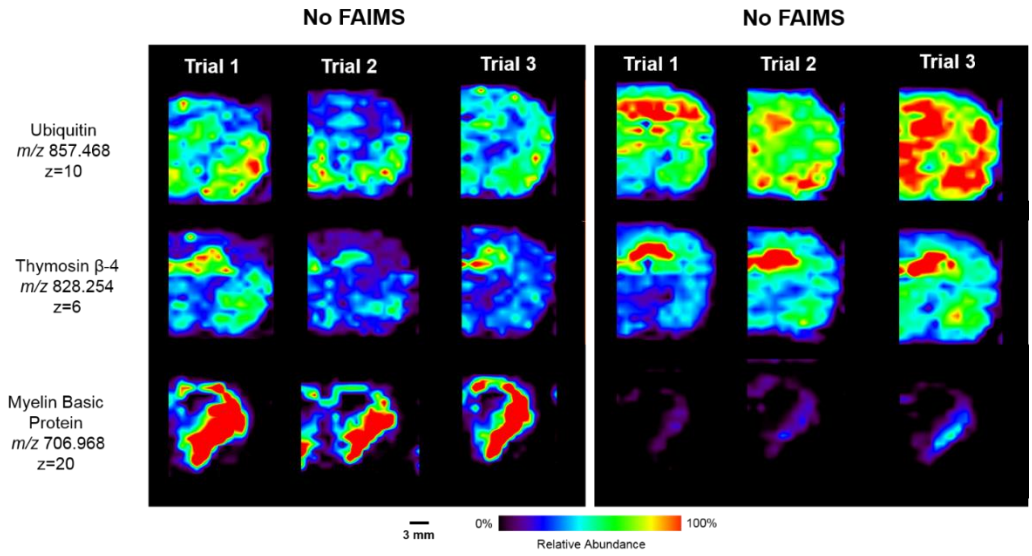

Figure 3.7. Ion images of three representative proteins on replicates (n=3) of serial sections of rat brain tissue half sections to show consistency of ion distribution when using LMJ-SSP and LMJ-SSP-FAIMS.

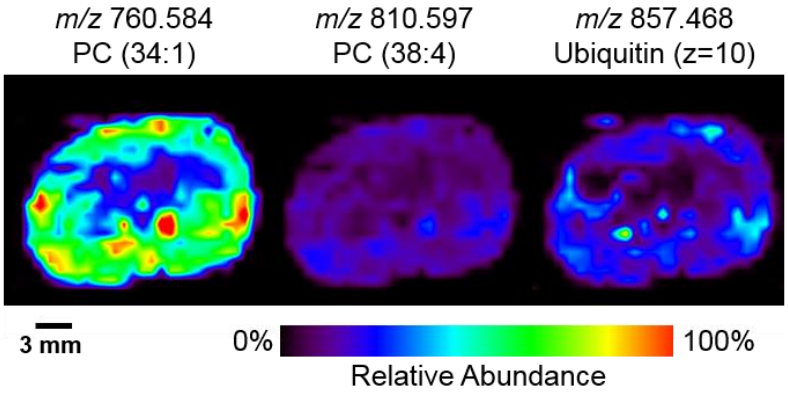

Figure 3.8. LMJ-SSP-FAIMS-MS lipid and protein ion images obtained through selective imaging for proteins.

although at lower relative and absolute abundances. For example, Figure 3.8 shows the ion images obtained from an unwashed rat brain tissue section for *m/z* 760.584, PC (34:1), *m/z* 810.597, PC (38:4), and *m/z* 857.370, ubiquitin, which were detected during the same LMJ-SSP-FAIMS-MS imaging experiment.

3.3.5 LMJ-SSP-FAIMS-MS imaging of proteins in ovarian cancer tissue sections

The integrated LMJ-SSP-FAIMS approach was applied to image proteins in human normal ovarian and high grade serous ovarian cancer tissue samples. 2D ion images revealed distinct spatial distribution of various protein ions within the tissue sections, as shown in Figure 5b for four selected protein ions: 10+ ion cluster at *m/z* 857.963 (MW = 8559.54 Da), identified as ubiquitin (P-score = 1.6×10^{-20}, 13% sequence coverage, mass error of 9.35 ppm, Figure B.8 and Table B.4); 5+ ion cluster at *m/z* 993.501 (MW = 4960.46 Da), identified as thymosin β-4 (P-score = 1.6×10^{-5}, 12% sequence coverage, mass error of 6.15 ppm, Figure B.9 and Table B.5); 16+ ion cluster at *m/z* 946.311 (MW = 15116.76 Da), identified as hemoglobin α-subunit (P-score = 5.3×10^{-11}, 26% sequence coverage, mass error of −7.94 ppm, Figure B.10 and Table B.6) and the 9+ ion cluster at *m/z* 1122.038 (MW = 10084.27 Da), proposed as calcyclin (P-score = 5.4×10^{-12}, 7% sequence coverage, mass error of 4.46 ppm). Histopathologic evaluation of H&E stained serial sections revealed the presence of necrotic tissue adjacent to the tumor cells in the tumor tissue, while the normal tissue was homogeneously composed of normal ovarian tissue. Comparison of the 2D ion images and the annotated optical images of the H&E stained samples revealed that ubiquitin, thymosin β-4, and calcyclin showed higher relative abundances within the tumor region of the ovarian tumor sample compared with both the necrosis region and the normal ovarian tissue. Hemoglobin α-subunit, however, showed higher relative abundances

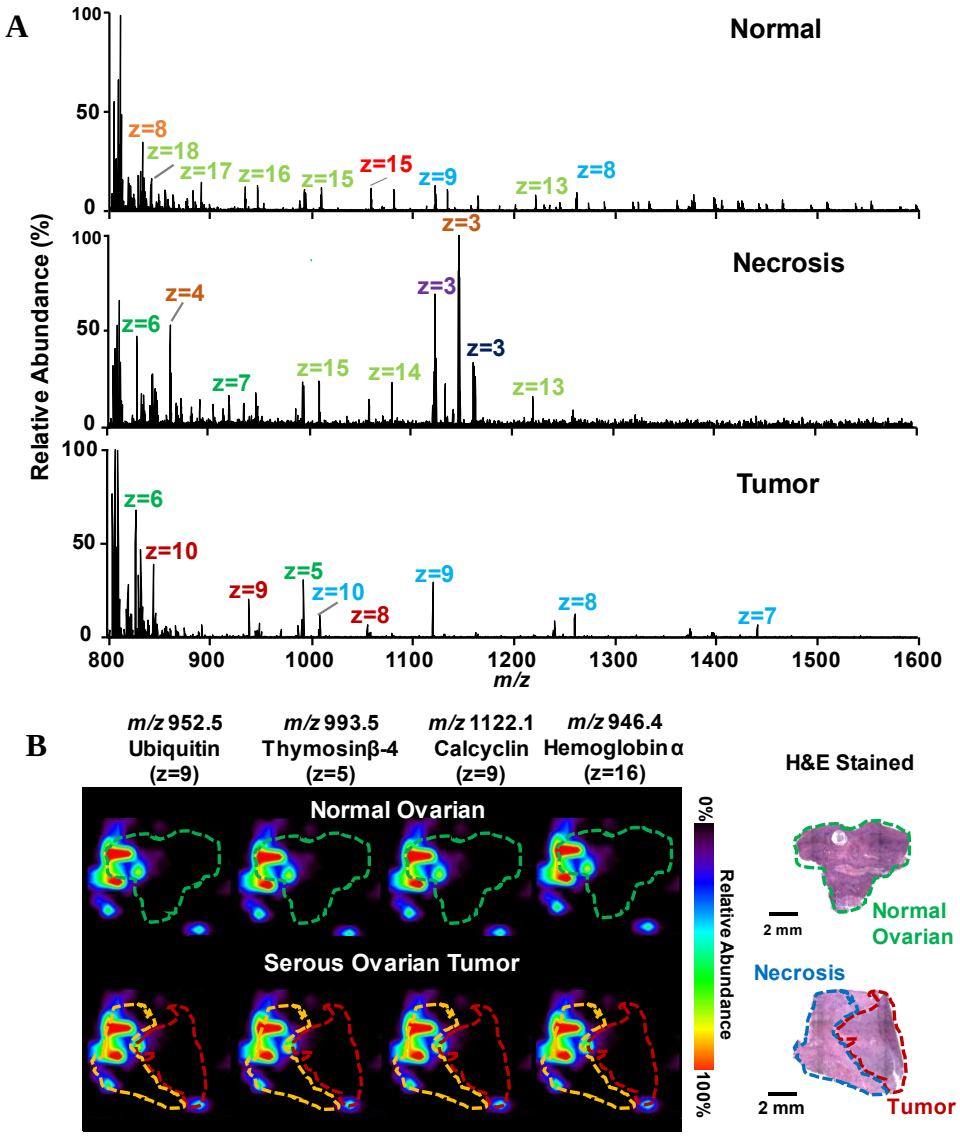

Figure 3.9. Static LMJ-SSP-FAIMS-MS profiling and imaging of human normal and cancerous ovarian tissues.

(A) LMJ-SSP-FAIMS-MS spectra of normal ovarian, necrotic, and serous ovarian cancer samples in which different colored labels represent different charge states of same protein species. (B) LMJ-SSP-FAIMS-MS ion images of ubiquitin, thymosin β-4, calcyclin, and hemoglobin α-subunit for a normal ovarian tissue sample compared with the high grade serous ovarian tumor sample, containing both necrotic and tumor regions (spatial resolution is ~630 μm). Optical images of H&E stained sections show regions of normal ovarian, necrotic, and high grade serous ovarian tumor.

within the necrosis region compared to the adjacent tumor region and the normal ovarian tissue. The mass spectra obtained showed distinct protein distribution for high grade serous ovarian cancer, necrotic ovarian tissue, and normal ovarian tissue under optimized LMJ-SSP-FAIMS conditions (Figure 3.9A).

3.4 CONCLUSIONS

We developed and optimized an analytical approach integrating DESI and LMJ-SSP with a chip-based FAIMS device for imaging biological tissue samples. This method allowed for partial separation of analytes after desorption or extraction from biological samples, resulting in decreased chemical noise and increased detection of selected molecular species. Reducing interferences through FAIMS separation improved the S/N for the species of interest, aiding in spectra interpretation and improving ion image quality. Optimization of DF and CF values for semi-targeted transmission of different molecular classes can be performed through 2D-FAIMS sweeping experiments during a profiling or a more time-consuming imaging assay, directly from tissue samples.

We show through several examples that this approach is particularly useful for semi-selective imaging of subsets of multiply charged lipids and proteins at optimized FAIMS conditions, with no increase in analysis time. For example, improvement in the S/N, ion abundances, and number of doubly charged CL and gangliosides species at optimized FAIMS conditions were observed in rat brain tissue sections. DESI-FAIMS-MS imaging allowed enhanced detection and imaging of diagnostic CL in human oncocytic thyroid tumor with reduced interference from other GP species, enabling improved ion isolation and identification by tandem MS. LMJ-SSP-FAIMS-MS imaging was particularly powerful for imaging multiply charged protein ions from biological

tissue samples. Optimized FAIMS parameters for proteins in the 4−12 kDa range allowed increase in the S/N, number detected, and visualization of the 2D spatial distribution of 84 protein species within rat brain, even with an overall decrease in total ion current. LMJ-SSP-FAIMS-MS imaging of human ovarian tissue samples enabled detection, identification, and correlation of spatial distribution of several proteins within the heterogeneous regions of the tissue samples, including regions of tumor, necrotic, and normal ovarian tissues. This is the first example of global protein imaging in human cancer tissue by ambient ionization MS imaging.

Our results show that FAIMS can be successfully integrated with DESI and LMJ-SSP for improved detection and imaging of subsets of molecular species in biological tissues. While separation using the planar FAIMS device caused a decrease in total ion abundance of 1 order of magnitude or more, an increase in S/N ratio due to concomitant reduction of noise level contributed to improved data quality for MS imaging experiments.[84] Thus, addition of FAIMS to a DESI or LMJ-SSP MS imaging workflow at optimized conditions is valuable for the detection and spatial visualization of otherwise undetectable lipids and proteins of diagnostic importance in biological tissues. Yet, while FAIMS provides a separation capability to increase data quality in ambient ionization MS imaging, ion suppression and matrix effects during ionization are still pertinent and should be considered as these may hinder ionization of molecules of interest.[63]

Further optimization of the integrated system is being pursued to increase sensitivity and ion transmission. As with other MS imaging techniques, the extent of molecular information obtained is significantly less than that achieved with standard HPLC-MS approaches. For example, HPLC-MS proteomic assays of selected tissue regions obtained by laser capture microdissection can be performed at similar spatial resolution as LMJ-SSP, although more time-consuming and labor intensive.[91] Evaluation

of the molecular coverage achieved when compared to standard chromatographic separation techniques will be sought to better quantify the utility of our approach. However, as ambient ionization MS imaging provides molecular and spatial information at a fraction of the time, without extensive sample preparation, we expect the integrated approach described here to be valuable in biomedical applications targeted at imaging specific diagnostic lipids and proteins which are otherwise difficult to detect in biological tissues.

Chapter 4: Double bond characterization of free fatty acids directly from biological tissue samples by ultraviolet photodissociation[3]

4.1 INTRODUCTION

Free fatty acids (FA) have a variety of roles within eukaryotic cells that are vital to cellular structure and functions. Often termed the "building blocks" of lipids, FAs play a crucial role in the formation of cell membranes and often contribute to their biophysical properties. Acyl chain length, degree of unsaturation, and double bond position of the FA chains of lipids dictate membrane fluidity, which can often affect biological processes occurring within or near cells.[92] FAs are also a significant source of energy for cells as they can be completely oxidized into CO2 by beta-oxidation, in turn producing energy-rich adenosine triphosphates to power cellular processes.[93] Cells can obtain FAs in two ways: scavenging from exogenous sources or by de novo synthesis through FA synthase. Typically, healthy cells rely predominantly on the former to source their required FAs. However, cancerous cells have shown to produce FAs endogenously in order to supply the molecules required for rapid cell growth.[94] Increased level of FA synthase has been observed in breast[95,96], ovarian[97], and prostate[98] cancers, resulting in increased abundance of FAs within the tissues and blood of these patients. Additionally, FA synthase overexpression has been associated with more aggressive forms of cancer. Kuhajda et al., for example, found that overexpression of the functional FA synthase OA-519 was associated with an aggressive form of breast cancer and increased de novo FA synthesis.[99] Due to this difference between healthy and cancerous cells, there has been a strong interest in understanding the alterations in FA composition caused by

[3] Adapted with permission from "Feider, C. L.*; Macias, L.A.*; Brodbelt, J.S.; Eberlin, L. S., Double bond characterization of free fatty acids directly from biological tissues by ultraviolet photodissociation." *Anal. Chem.* **2020,** *92* (212), 8386-8395. C.L. Feider and L.A. Macias contributed equally to the submitted manuscript, but data descibed in this chapter was collected primarily by C.L. Feider. All authors assited in the preparation and editing of the manuscript. All authors revised the manuscript.

cancer as these differences may be exploited for determination of disease biomarkers and possible therapeutic targets.[100,101]

Mass spectrometry (MS) is a powerful tool for the investigation of these alterations, allowing for both qualitative and quantitative analysis of FA within biological samples. For example, liquid chromatography (LC) MS couples with electrospray ionization (ESI) of biological extracts allows for the detection of deprotonated FA anions, facilitating investigation of the sum composition of FA within a sample based on the exact mass measurements of the ions.[102,103] Additionally, the structural information of FAs responsible for membrane properties, such as branching, degree of unsaturation, and double bond location, can be evaluated with the use of tandem MS (MS/MS). Unfortunately, the primary ion activation technique, collision induced dissociation (CID), does not provide this informative information. Low energy collisional activation of FA typically results in fragmentation of the most labile bonds proximal to the carbonyl group, producing neutral loss fragments of water and carbon dioxide rather than structural information about the acyl chain.[104,105] To bypass this limitation, three main strategies have been developed: double bond derivatization, charge-switching, and implementation of alternative ion activation methods.[106-111] Double bond derivatization techniques, such as the Paternò-Büchi reaction[107,112,113] and meta-chloroperoxybenzoic-acid (m-CPBA) epoxidation[114,115] have been implemented to modify the double bonds to make them amenable to fragmentation by CID, resulting in informative double bond products upon activation. Charge-switching strategies, in contrast, involve the modification of the carboxyl group to promote cationization and dissociation of the acyl chain of FA through stabilization of the fragile bonds near the carboxylic acid. These methods, which include non-covalent metal adduction,[116] head group derivatization,[108,117] and gas phase ion/ion reactions,[109,110] yield products informative of the double bond

position when applied to the fragmentation of FA. The use of alternative ion activation methods that facilitate higher-energy fragmentation pathways, such as ultraviolet photodissociation (UVPD),[118,119] ozone-induced dissociation (OzID),[120] and electron-induced dissociation (EID),[121] are also promising techniques for the localization of double bonds in lipids and integration with these activation methods with charge-switching strategies have been successful in elucidating FA structures.[122-125] Ultraviolet photodissociation, in particular, has been shown to provide detailed structural information including double bond and sn-position from phospho- and sphingo- lipid isomers as well as isomers from cationized FAs.[118,119,124,126] UVPD fragmentation of unsaturated lipids produces diagnostic product ions with a mass difference of 24 Da due to cleavage of the bonds adjacent to the double bonds, thus allowing for confident localization of the double bonds.

While shotgun and chromatographic analyses of biological extracts allow sensitive and in-depth investigation of the metabolic alterations in biological samples, they do not provide insight into the distribution or spatial localization of FAs or lipids in tissue. Human cancer tissues, for example, often present complex histology including viable tumor regions within necrotic tissue, healthy stroma, calcifications, connective tissue, and regions of inflammation. As each of these cell populations undergoes unique metabolic processes, tissue homogenization precludes precise identification of the molecular alterations occurring within tissue regions that are enriched with a specific cell type. Alternatively, MS imaging techniques allow acquisition of spatially accurate molecular information with the spatial resolution needed to correlate molecular and histologic information directly from tissues sections. Desorption electrospray ionization (DESI) MS, for example, has been extensively used to investigate the metabolic alterations occurring in diseased tissues, especially lipids.[127,128] For example, DESI-MS

imaging has been used to identify alterations in free FA in a variety of human tissues including cancer.[128,129] To improve detection of FA directly from tissues, the inclusion of silver ions and dicationic compounds (DCs) in the DESI solvent system has been used to enable detection of negatively charged lipids in the positive ion mode.[130,131] DESI and other MS imaging techniques have been integrated with double bond elucidation methods to investigate lipid isomerism within tissue sections. For example, matrix assisted laser desorption/ionization (MALDI) has been integrated with gas-phase OzID and Paternò–Büchi derivatization for the imaging of double bond and sn-positional isomers of phosphatidylcholines (PC), glycerophospholipids (GP) and glycosphingolipids in mouse brain tissues.[132,133] Tang et al. integrated online Paternò–Büchi derivatization with a liquid microjunction surface sampling probe (LMJ-SSP) to perform in situ isomeric ratio analysis of free FA and PC lipids in healthy and disease mouse tissue sections.[134] Kuo et al. utilized offline m-CPBA derivatization coupled to DESI-MS imaging to resolve FA isomers within kidney and metastatic lung tissue sections from murine cancer models.[115] Both works by Kuo et al. and Tang et al. showed significant alterations in the double bond position of FA 18:1, either free or conjugated to GP, within the murine cancerous tissue, suggesting dysregulation of FA synthase.

Previous work from our group shows the integration of 193 nm UVPD with DESI on an Orbitrap platform for MS imaging of GP isomers in biological tissue sections.[135] Using this approach, isomeric double bond distribution was observed in tissue sub-regions of different histologic composition in human tissue samples. For example, the 11Δ positional isomer of PC 18:1_18:1 was found at higher relative abundances in normal lymph node tissue when compared to the abundance within an adjacent thyroid metastasis, suggesting differential uptake of synthesis of FAs between these tissue types. In the present study, we used 193 nm UVPD coupled to reactive DESI to evaluate

double-bond positions in charge-inverted free FAs directly from biological tissue sections and uncovered differences in free FA isomer compositions between molecular subtypes of breast cancer tissues.

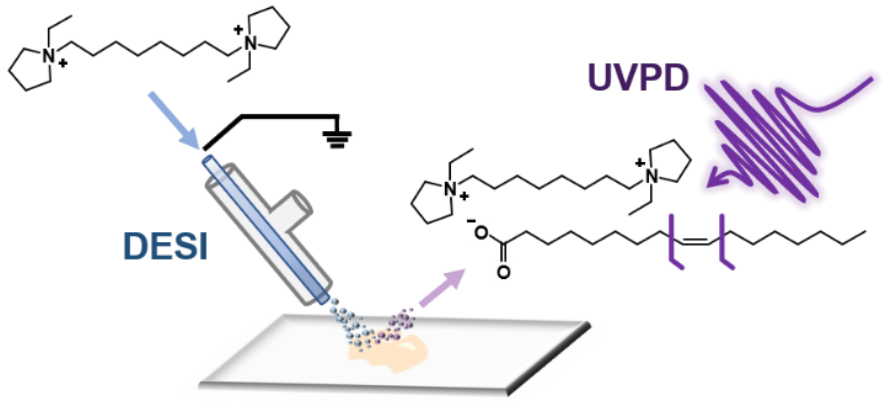

Illustration 4.1. Scheme of reactive DESI-UVPD-MS imaging of biological tissue sections

4.2 MATERIALS AND METHODS

4.2.1 Chemicals

All chemicals for the synthesis of the stable DC compounds, including 1,6-dibromohexane, 1,8-dibromooctane, 1-methylpyrrolidine, 1-ethylpyrrolidine, ethyl acetate, isopropyl alcohol, and phosphorus pentoxide were purchased from Sigma Aldrich (Milwaukee, WI). FA standards were purchased from Sigma-Aldrich (St. Louis, MO) and used without further purification. High purity methanol and acetone used for DESI-MS imaging was purchased from Fisher Scientific (Hampton, NH).

4.2.2 Synthesis and evaluation of dicationic compounds

Four DCs, displayed in Table C.1, were synthesized following established procedures reported in the literature.[136-138] All possible combinations of 1,6-dibromohexane, 1,8-dibromooctane, 1-methylpyrrolidine, and 1-ethylpyrrolidine were used to produce the four compounds under the same synthetic conditions. The four compounds were evaluated for efficient complexation with free FAs during DESI-MS analysis and for reduction of interfering fragment ions produced by UVPD. Due to a fragment ion produced from the 1-methylpyrrolidine containing compounds interfering with the distal diagnostic peak from the FA 18:1 (11Z) isomer (Figure C.1), the 1-ethylpyrrolindine compounds were selected as optimal for the present application. The synthetic yield of $C_8(epy)_2$-Br, termed 1,8-ethyl DC, was greatest and thus utilized for all experiments described in this work.

4.2.3 Tissue samples

Optimization of parameters was performed using mouse brain tissue samples, purchased from BioIVT (Westbury, NY). Frozen human tissue samples were obtained

from the Cooperative Human Tissue Network (CHTN) and Asterand Biosciences (Detroit, MI) under approved IRB protocols. Samples were stored in a -80C freezer until sectioned. Tissue samples were sectioned at 10 µm thick using a CryoStar NX50 cryostat (Thermo Scientific, Waltham, MA) and thaw mounted on glass slides. After sectioning, the glass slides were stored at -80C. Immediately prior to MS imaging, the glass slides were thawed and dried for ~15 min.

4.2.4 DESI-UVPD MS imaging

Mass spectra were collected on a Thermo Scientific Orbitrap Fusion Lumos mass spectrometer (San Jose, CA) modified to perform UVPD in the dual linear ion traps with a 193 nm Coherent Excistar excimer laser (Santa Cruz, CA) as previously described.[139] a 2D Omni Spay DESI imaging platform (Prosolia Inc. Indianapolis, IN) was coupled to an Orbitrap Fusion Lumos mass spectrometer (Thermo Scientific, San Jose, CA) using an adaptor (Prosolia, Indianapolis, IN) and a lab-built extended capillary, as described previously.[135] The DESI solvent system utilized was methanol:acetone 80:20 with 15 µM 1,8-ethyl DC at a flow rate of 7 µL/min, yielding a pixel size of the MS image of 200 µm. The complexed FAs were isolated in the quadrupole and subjected to 193 nm UVPD in the high-pressure ion trap with 20 laser pulses at 4 mJ per pulse. DESI-UVPD-MS imaging was performed in the positive ion mode with an isolation width of 1.5 *m/z* centered at the mass of interest and a resolving power of 30,000. The maximum injection time was set to 1800 msec to obtain optimal signal-to-noise of fragment peaks. Imaging data was acquired in full profile mode.

4.2.5 2D image processing

Thermo RAW files were converted to mzML files using msConvert (ProteoWizard) using a threshold peak filter of 50 to reduce file size.[140] mzML files were then imported into R using the mzR package from Bioconductor repository. Images were constructed for each *m/z* value using the intensity of the exact *m/z* value ± 0.02 Da.

4.2.6 Data extraction and statistical analysis

After DESI-MS imaging of breast carcinoma tissues, the same sections analyzed were stained with hematoxylin and eosin (H&E) and evaluated by a pathologist for determination of regions of pure tumor tissue. Converted mzML files were then compiled into an imzML data format using imzML converter[141] and uploaded into MSiReader for extraction of the double bond diagnostic *m/z* peaks within areas of breast carcinoma tissue.[142] Extracted data was then imported into R and the 9Δ /11Δ ratios for each pixel were calculated. Non-parametric t-tests of the data were performed by calculating the mean log ratio of the diagnostic ions was calculated for each sample, followed by calculation of the mean for the tissue subsets to be analyzed (metastatic vs. non-metastatic, estrogen receptor (ER) positive vs. ER negative, and progesterone (PR) positive vs. PR negative). We then permuted the sample log means between the two groups and calculated the hypothetical distribution of the permutated sample sets (repetitions = 5000). The p-values were calculated by dividing the number of times the absolute mean difference of the observed value was smaller than the absolute value of the permuted mean by the number of repetitions. As three hypotheses were tested using the same data, a Bonferroni correction was applied resulting in a new significance cutoff value of $\alpha = 0.0167$.

4.2.6 Nomenclature

Lipid shorthand, as described by Liebsich et al., was adopted.[143] FA structures are described by the number of carbon atoms, followed by a colon and the number of double bonds. Carbon positions are described relative to the carboxyl carbon (C1). If the position of the double bonds is known, it is indicated in parentheses following the number of double bonds. The double bond geometry is indicated by Z (for cis), E (for trans), or Δ (for unknown) following the double bond position. For ease of discussion, fragment ions arising from cleavage of C-C bonds adjacent to C=C double bonds are referred to as proximal (e.g. Δ_p) and distal (e.g. Δ_d) in reference to the C-C bond on the carboxyl- and methyl-end, respectively.

4.3 Results and Discussion

4.3.1 Double bond localization within fatty acids by dication complexation and UVPD

Our collaborators, Prof. Jennifer Brodbelt and Luis Macias, first explored the utility of 193 nm UVPD in cleaving and characterizing double bonds within deprotonated FAs in the negative ion mode. Application of this activation method to free FAs was explored and shown to result in low abundance fragment ions that paralleled the dissociation pathways of phospo- and sphingolipids. However, the intensity of these diagnostic fragments was extremely low, about 0.030% of the total ion current in the spectra, which precludes integration with a lower sensitivity ionization technique such as DESI-MS. Additionally, 193nm UVPD of polyunsaturated FAs yielded uninformative neutral losses and dissociation of C-C bonds, precluding the ability to assign double bond positions. As charge-switching strategies have shown ability to increase the efficiency of fragmentation for double bond elucidation, similar methods were explored for integration

into a DESI-UVPD imaging workflow. Specially designed dications (DCs), for example, have been shown to readily adduct and charge-invert free FAs from negative to positive ion mode without compromising sensitivity when implemented in a DESI workflow.[131,137] In this approach, the anionic carboxylate group present on the FA structure binds electrostatically with the DC possessing a fixed 2+ charge, generating a DC-FA complex with a net +1 charge. Although collisional activation of non-covalent DC●lipid complexes is dominated by neutral losses from the dication group,[131] 193 nm UVPD has been shown to yield product ions that retain non-covalent interactions. Additionally, reactive DESI-MS of mouse brain tissue sections with DC molecules doped into the spray solvent, as outlined in Lostun *et al*., enables formation of the DC●FA complexes with high efficiency.[131] We thus explored reactive DESI-MS imaging of a tissue section in tandem with UVPD of the DC●FA complexes to acquire spatially correlated information regarding the distribution of FA isomers within heterogenous biological tissues.

4.3.2 DESI-UVPD MS imaging of isomers in monounsaturated fatty acids

DESI-MS was coupled to an Orbitrap Fusion Lumos mass spectrometer equipped with a 193 nm excimer laser to perform UVPD-MS imaging of a human ovarian tumor tissue sample containing a region of high grade serous ovarian carcinoma adjacent to a region of normal ovarian tissue. The molecular profile of the ovarian tissue acquired in the full *m/z* 500-1000 range showed high abundance of FA species complexed with DC (Figure 4.1, Table 4.1), including various saturated, mono- and polyunsaturated FA species normally detected from biological tissues using DESI-MS imaging in the negative ion mode of biological tissues. DC complexed to other GP species, primarily glycerophosphoethanolamines, were also observed in the mass spectra, but UVPD of

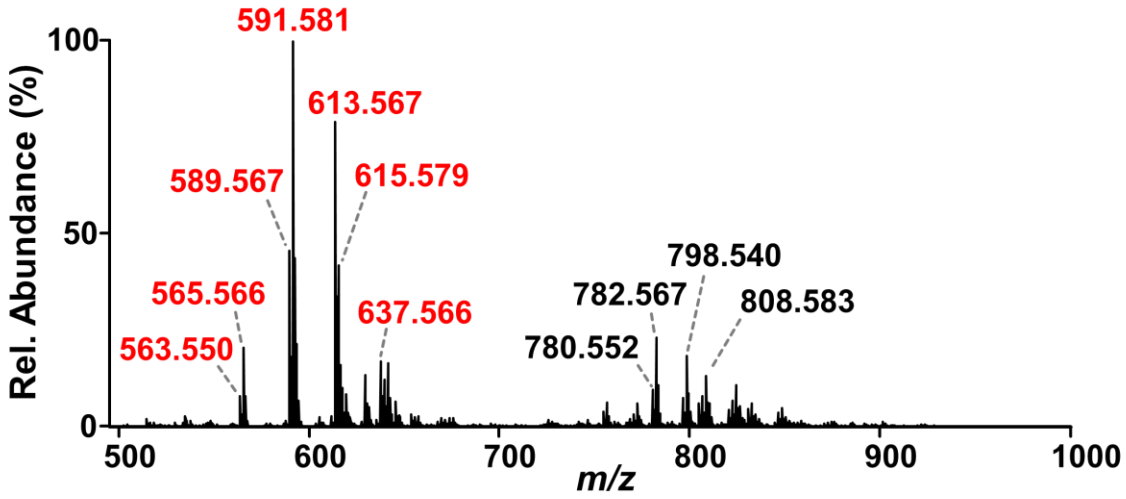

Figure 4.1. Full MS profile of ovarian tumor tissue analyzed by DESI-MS in the positive ion mode

Table 4.1. DC●FA complexes detected from ovarian tissue

Fatty Acid	Theoretical mass [M]	Observed mass (m/z) $[M+DC]^+$	Theoretical m/z $[M+DC]^+$	Mass error (ppm)
FA 16:1	254.2246	563.5503	563.551	-1.24
FA 16:0	256.2402	565.5657	565.5666	-1.59
FA 18:3	278.2246	587.5528	587.551	3.06
FA 18:2	280.2402	589.5669	589.5666	0.51
FA 18:1	282.2559	591.5812	591.5823	-1.86
FA 20:5	302.2246	611.5495	611.551	-2.45
FA 20:4	304.2402	613.5664	613.5666	-0.33
FA 20:3	306.2559	615.5795	615.5823	-4.55
FA 20:2	308.2715	617.5943	617.5979	-5.83
FA 20:1	310.2872	619.612	619.6136	-2.58
FA 22:6	328.2402	637.5661	637.5666	-0.78
FA 22:5	330.2559	639.5804	639.5823	-2.97
FA 22:4	332.2715	641.5967	641.5979	-1.87
FA 22:2	336.3028	645.6254	645.6292	-5.89
FA 22:1	338.3185	647.6444	647.6449	-0.77
FA 22:0	340.3341	649.6568	649.6605	-5.70

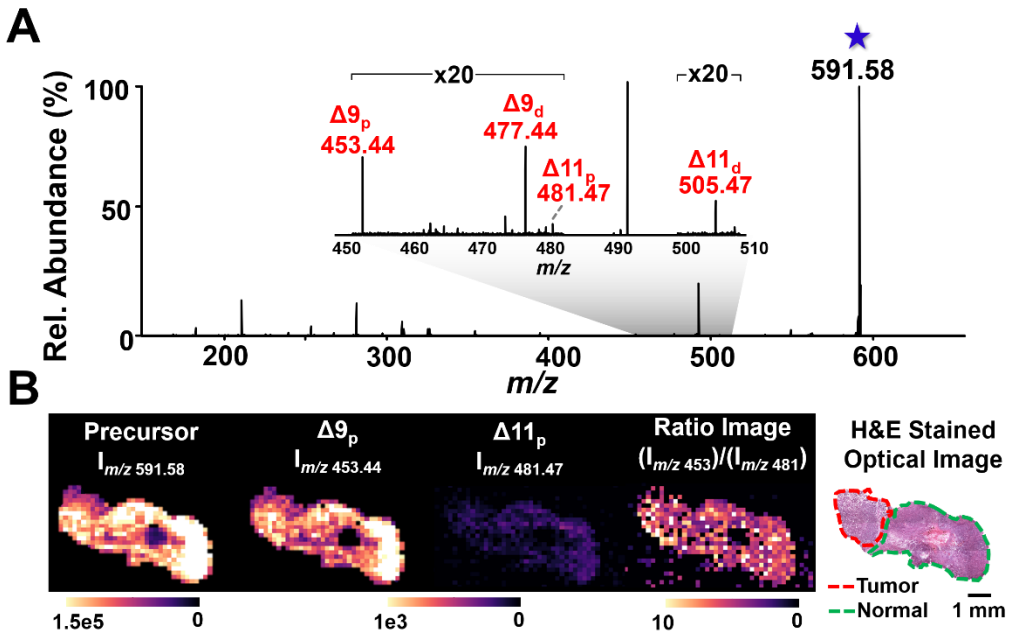

Figure 4.2. DESI-UVPD MS imaging of the distribution of the FA 18:1 double bond isomers within an ovarian tumor tissue.

(A) The DESI-UVPD spectrum shows two pairs of diagnostic ions resulting from the fragmentation of the 9Δ and 11Δ positional isomers. (B) The ion images from the precursor ion (*m/z* 591.58), the proximal fragment peaks for each isomer ($9\Delta_p$ at m/z 453.44 and $11\Delta_p$ at *m/z* 481.47), and the $9\Delta_p$:$11\Delta_p$ ratio, illustrating that there is no observable difference in the isomer distribution when comparing the tumor and normal ovary tissue regions for this patient.

these species were not explored in this study. The most abundant complex of *m/z* 591.581 identified as DC●FA 18:1 was targeted for UVPD. Figure 4.2A shows an average UVPD mass spectrum of the *m/z* 591.581 complex acquired during DESI-MS imaging across the tissue section, resulting in two pairs of diagnostic products characteristic of a mixture of 9Δ and 11Δ FA 18:1 isomers. The relative abundance of the 9Δ ions of *m/z* 453.44 and *m/z* 477.44 was approximately one order of magnitude higher than those from the 11Δ ions of *m/z* 481.47 and *m/z* 505.47 across the tissue section. To investigate the spatial distribution of the isomers more closely, ion images of the precursor ion, the proximal isomeric fragments ($9\Delta_p$ and $11\Delta_p$), and the $9\Delta_p$:$11\Delta_p$ ratio were generated (Figure 4.2B). All images showed consistent signal intensity across the tissue section, including the normal and tumor ovarian tissue regions, with the normal region having a log mean ratio of 0.779 ± 0.123 and the cancer region having a log mean ratio of 0.832 ± 0.164. This suggests that any alterations in the isomeric distribution of FA 18:1 between tumor and normal ovarian tissues from this patient are minimal and, if present, are less prominent than the random fluctuations in signal intensity associated with DESI-UVPD MS analysis (17.8% RSD for precursor ion signal and an average 27.9% RSD for Δ9 and Δ11 fragment ions).

4.3.3 DESI-UVPD-MS imaging of polyunsaturated fatty acid isomers

Although UVPD of polyunsaturated FA anions was ineffective, charge inversion via DC complexation promoted rich UVPD mass spectra suited for double bond localization. UVPD fragmentation of a DC●FA 18:2 (9Z,12Z) ion by ESI yielded diagnostic product ion pairs at *m/z* 453.44/477.44 and *m/z* 493.47/517.47 for the 9Z and 12Z double bonds, respectively. Similarly, 193 nm UVPD of the DC●arachidonic acid (FA 20:4(5Z,8Z,11Z,14Z)) complex produced four pairs of diagnostic fragments with a

mass difference of 24 Da (*m/z* 397.38/421.38 for 5Z; *m/z* 437.41/461.41 for 8Z; *m/z* 477.44/501.44 for 11Z; *m/z* 517.47/541.47 for 14Z), in addition to produces resulting from cleavage of all C-C bonds in the acyl chain. Spectra resulting from polyunsaturated FA were much more complex due to photoinduced excitation and production of radicals, presenting challenges for application in imaging a complex sample.[126] However, as UVPD produces ion pairs, the risk of misidentification of a double bond is reduced as both diagnostic products from the fragmentation on either side of the double bond would need to be present to suggest confident identification of the double pond positional isomer. Considering this limitation, DESI-UVPD MS was utilized to image polyunsaturated FA isomers within biological tissue sections.

Applying DESI-UVPD MS imaging to analyze DC●FA 18:2 (*m/z* 589.56) directly from ovarian tissue confirmed that polyunsaturated FAs can also be characterized from biological samples. While polyunsaturated FAs within mammalian tissues have less varied isomeric double bond positions than monounsaturated FAs, there is diversity in the abundance of ω-9, ω-6, and ω-3 FAs in the human diet that may be detected in tissue samples. DESI-UVPD-MS imaging of DC●FA 18:2 consistently displayed the pair of double bond diagnostic products that would arise for FA 18:2 (9Δ,12Δ), suggesting a homogeneous presence of this FA within the sample (Figure 4.3). Only one fragment ion, at most, was observed per double bond that would correspond to the hypothetical diagnostic products for FA 18:2 (12Δ,15Δ) and FA 18:2 (6Δ,9Δ), as shown in Table 4.2, thus providing no positive confirmatory evidence for these isomers in the samples.

DESI-UVPD-MS imaging of DC●FA 20:4 from ovarian tissue also yielded a complex mass spectrum, yet, all double bond diagnostic pairs of fragments for FA 20:4(5Δ,8Δ,11Δ,14Δ), the most prominent isomer of 20:4 in nature, were observed in the mass spectra and the ion images, as shown in Figure 4.4. As seen for the imaging of DC-

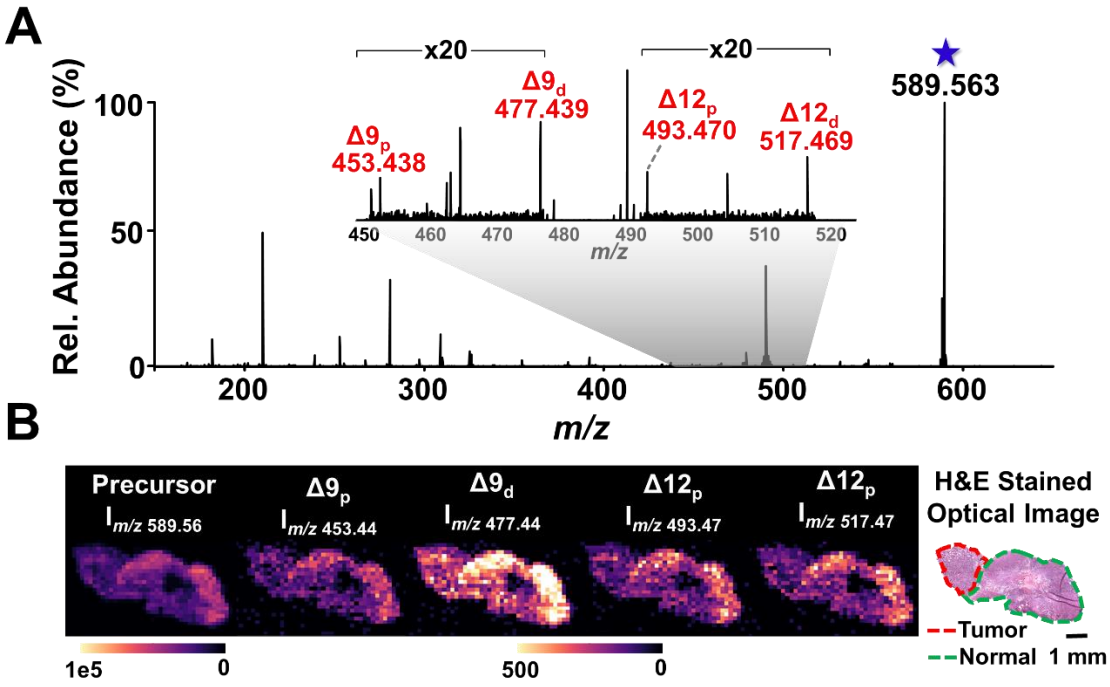

Figure 4.3. DESI-UVPD-MS imaging of FA 18:2 from an ovarian tissue section

(A) DESI-UVPD mass spectrum from the fragmentation of FA18:2 precursor ion of m/z 589.56 (B) Ion images of the precursor and double bond diagnostic peaks, showing the distribution of the isomers within the ovarian tumor tissue section.

Table 4.2. Hypothetical diagnostic fragments that would result from UVPD of FA 18:2 isomers

Fatty Acid	Hypothetical diagnostic fragment	Theoretical *m/z*	Observed *m/z*
18:2 (6Δ,9Δ)	$6\Delta_p$	411.395	--
	$6\Delta_d$	435.395	435.392
	$9\Delta_p$	451.426	452.424
	$9\Delta_d$	475.426	--
18:2 (9Δ,12Δ)	$9\Delta_p$	453.442	453.440
	$9\Delta_d$	477.442	477.440
	$12\Delta_p$	493.473	493.470
	$12\Delta_d$	517.473	517.470
18:2 (12Δ,15Δ)	$12\Delta_p$	495.488	--
	$12\Delta_d$	519.488	--
	$15\Delta_p$	535.520	--
	$15\Delta_d$	559.520	559.516

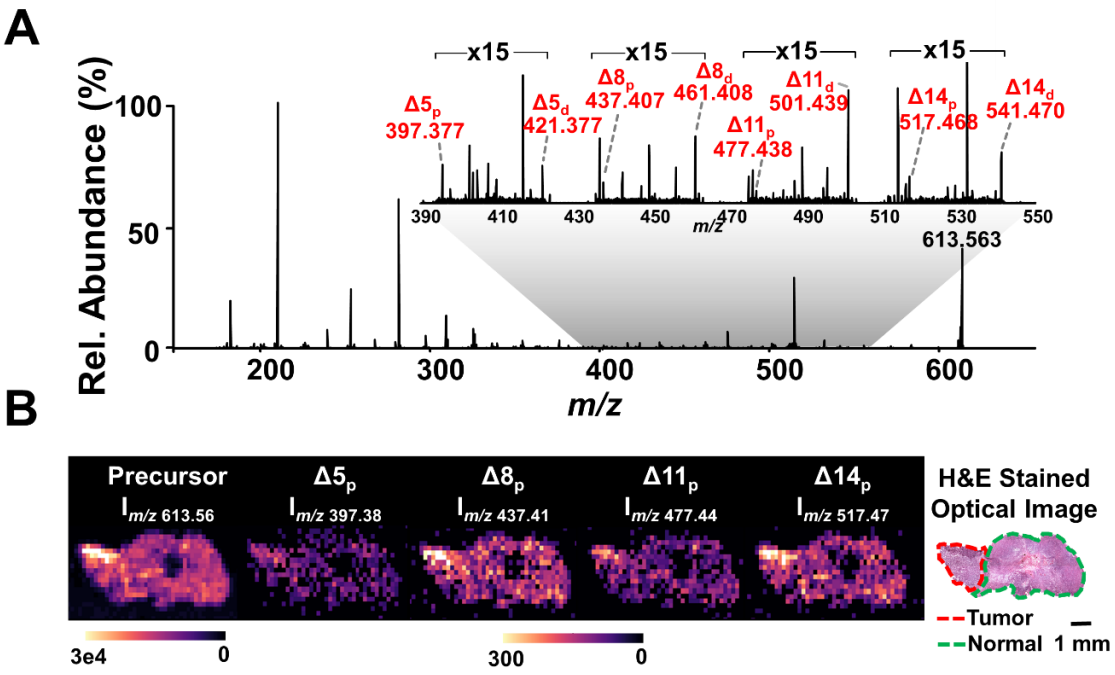

Figure 4.4. DESI-UVPD-MS imaging of FA 20:4 from an ovarian tumor tissue section

(A) DESI-UVPD mass spectrum from the fragmentation of FA 20:4 precursor at *m/z* 613.56 (B) Ion images of the precursor and select double bond diagnostic peaks, showing the distribution of the isomers within the ovarian tumor tissue section.

Table 4.3. Hypothetical diagnostic fragments that would result from UVPD of FA 20:4 isomers

Fatty Acid	Hypothetical diagnostic fragment	Theoretical *m/z*	Observed *m/z*
20:4 (5Δ, 8Δ, 11Δ, 14Δ)	$5\Delta_p$	397.380	397.377
	$5\Delta_d$	421.380	421.377
	$8\Delta_p$	437.410	437.408
	$8\Delta_d$	461.410	461.408
	$11\Delta_p$	477.442	477.440
	$11\Delta_d$	501.442	501.439
	$14\Delta_p$	517.473	517.470
	$14\Delta_d$	541.473	541.470
20:4 (8Δ, 11Δ, 14Δ, 17Δ)	$8\Delta_p$	439.426	--
	$8\Delta_d$	463.426	463.424
	$11\Delta_p$	479.457	--
	$11\Delta_d$	503.457	503.455
	$14\Delta_p$	519.488	--
	$14\Delta_d$	543.488	--
	$17\Delta_p$	559.520	--
	$17\Delta_d$	583.520	583.516

FA 18:2, possible diagnostic fragment ions for the ω-3 FA 20:4 isomer were detected within the mass spectra (Table 4.3) but only one diagnostic ion corresponding to the cleavage of each double bond position was detected, therefore preventing confident identification of the presence of this isomer.

Fragmentation of polyunsaturated FA differed from monounsaturated FA in the relative abundance of proximal and distal peaks. Both diagnostic fragments from monounsaturated lipids and FAs have typically exhibited similar ion abundances within each pair, but both ESI and DESI-MS results from the fragmentation of polyunsaturated FA show unequal relative abundances of the proximal and distal fragment ions.[144] For example, the $9\Delta_p$ fragment of *m/z* 453.44 is consistently more abundant than the $9\Delta_d$ fragment of *m/z* 477.44. As the ovarian tissue section is more molecularly complex than FA standards used in optimization experiments, there is a higher chance that interfering fragment ions from co-isolated species overlap with the diagnostic fragment ions and alter their observed abundance. To evaluate if these differences in the relative abundances are due to interfering ions, the ratio of the proximal and distal fragment ions was calculated for both ESI-MS and DESI-MS modes for both FA 18:2 and FA 20:4 (Figure 4.5). The proximal:distal ratio for every double bond pair produced upon UVPD was consistent between ESI and DESI analysis, suggesting these altered ratios do not originate from interfering isobars but rather represent preferential cleavages across the FA chain or overlapping fragmentation pathways of the DC●FA complexes.

4.3.4 Relative quantitation of double bond isomers with DESI-MS imaging

Previous UVPD analyses of unsaturated FAs within GPs demonstrated a linear relationship between the abundances of the diagnostic ions and the relative concentration of double bond isomers.[118,145] To evaluate if DESI-MS also allowed relative quantitation

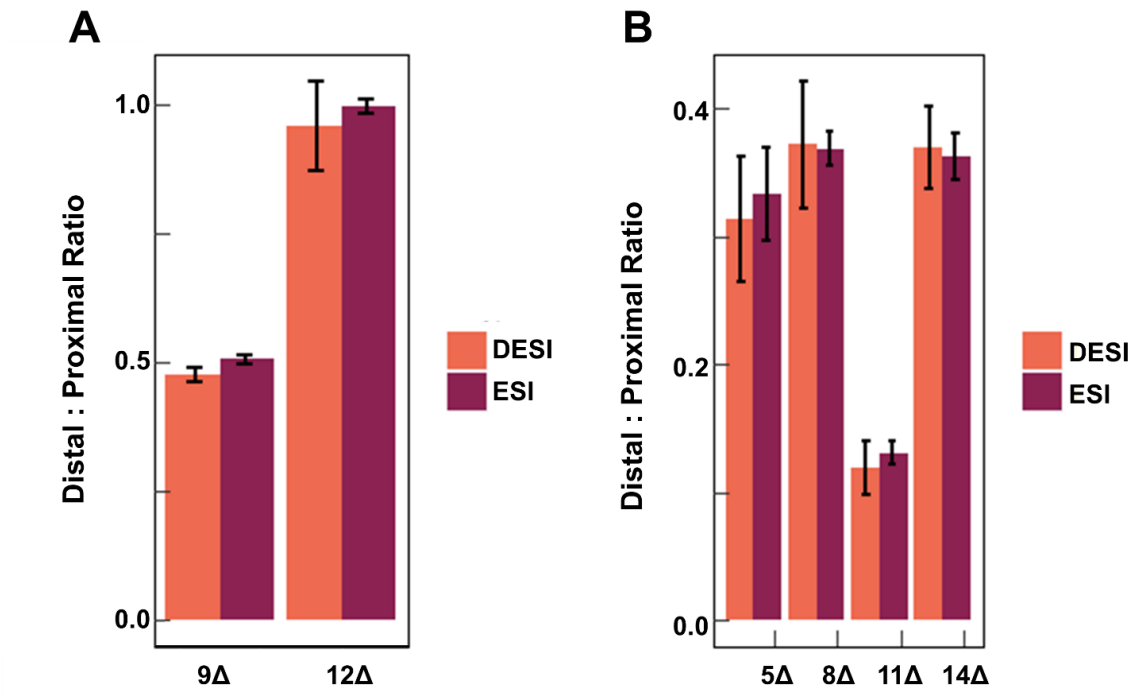

Figure 4.5. Comparison of distal:proximal fragment ion abundance ratios for each double bond for DC complex

(A) FA 18:2(9Z,12Z) and (B) FA 20:4(5Z,8Z,11Z,14Z) analyzed using FA standards in an ESI workflow and from ovarian tumor sections via reactive DESI.

of the FA isomers, mixtures containing various molar ratios of monounsaturated FA 18:1 (9Z) and FA 18:1 (11Z) were spotted on a PTFE surfaced and imaging of the surface was performed in tandem with UVPD of the FA 18:1 precursor ion (Figure 4.6). Ion images from the precursor ion show a consistent intensity across all sample spots at a similar absolute intensity value (NL≈1E5 during UVPD) to what was detected from the ovarian tissue sections (NL≈8E4 – 2E5 during UVPD), allowing extrapolation of calibration results to biological tissue sections. In previous studies, the abundances of diagnostic ions corresponding to each isomer were summed together in order to increase sensitivity. However, UVPD of DC-FA 18:1 (9Z) resulted in an ion of *m/z* 505.47 that is isomeric with the distal fragment of FA 18:1 (11Z) (Figure 4.7A,B). The added abundance from the confounding product disrupts the linear relationship between the concentration ratio of the isomers and signal abundance of the diagnostic ions (Figure 4.7C). To circumvent this challenge, a calibration curve was built excluding the distal fragments from both isomers. Plotting ion intensities for the 9Z and 11Z proximal diagnostic ions (*m/z* 453.44 and *m/z* 481.47, respectively) showed a clear gradient of intensities associated with altered concentration ratios. Plotting absolute concentration of the isomers against the average ion signal intensity of the respective proximal diagnostic peak for all spots (Figure 4.8) illustrated a linear relationship for both isomers ($9Z_p$ R2=0.9953, $11Z_p$ R2=0.9965). The calculated limits of detection for the isomers were 0.568 μM and 0.492 μM for the 9Z and 11Z diagnostic fragments, respectively, indicating that spots featuring the lowest concentrations of the isomers (0.5 μM) were not reliable. A DESI-MS imaging calibration curve was then constructed based on the ratio of isomer concentrations within the spots and the ratio of their resulting diagnostic fragment peak intensities for every pixel, excluding the 19:1 and 1:19 9Z:11Z ratios (Figure 4.6). The resulting curve showed

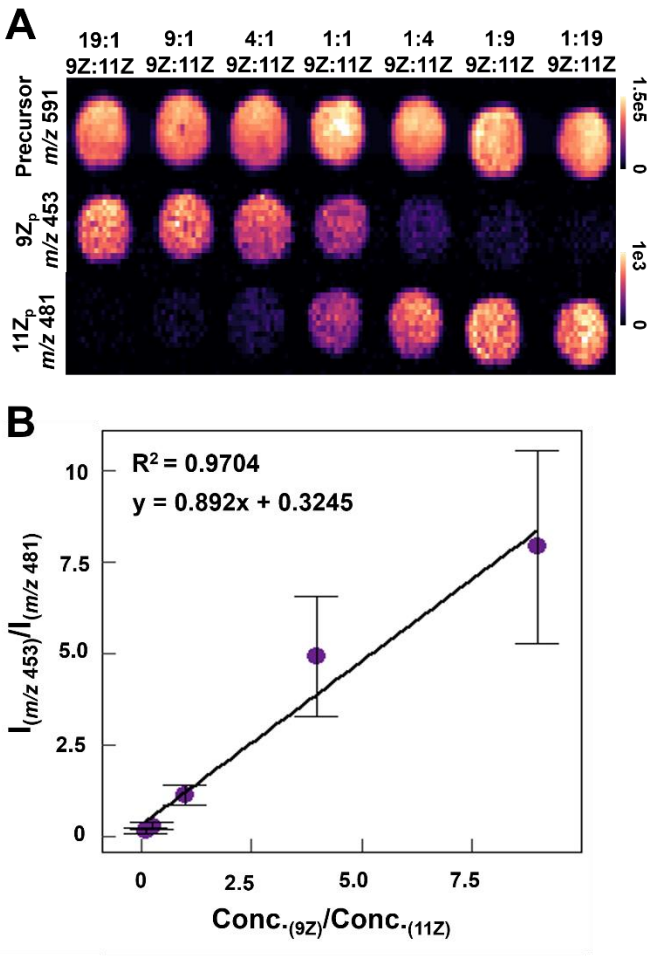

Figure 4.6. Relative quantification of DESI-UVPD-MS imaging of monounsaturated FA●DC complexes

(A) DESI-UVPD MS ion images of DC●FA 18:1 varying FA 18:1(9Z)/FA 18:1(11Z) rations. (B) Plot of the concentration ratio of FA 18:1(9Z):FA 18:1(11Z) versus the ratio of the intensity of 9Z:11Z proximal diagnostic ions.

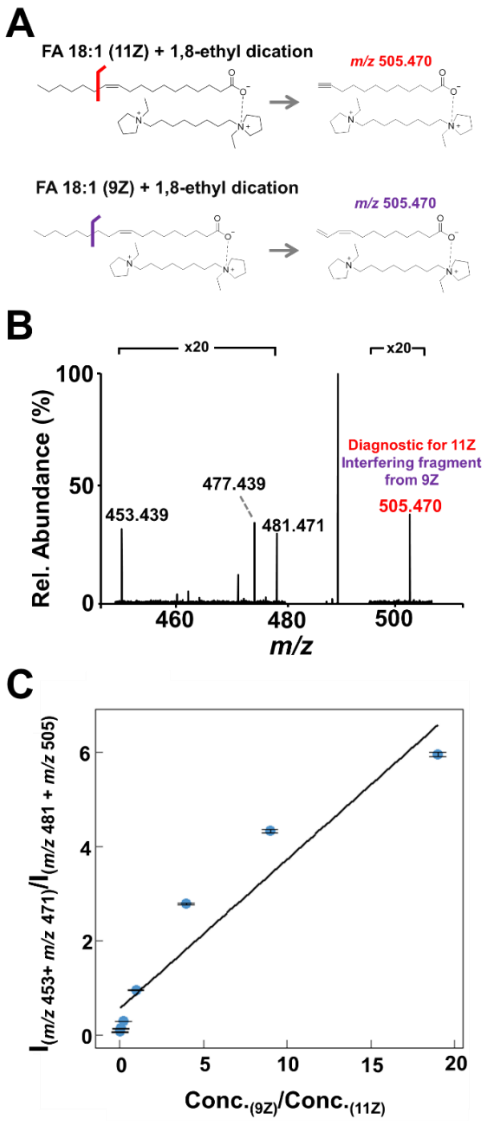

Figure 4.7. Evaluation of interfering fragments during UVPD of FA 18:1

(A) Illustration of isomeric fragment ion structures that preclude the use of *m/z* 505 as a diagnostic product for quantitative analyses of double bond location in DC - FA 18:1 complex. (B) Representative UVPD mass spectrum for DC●FA 18:1 complex arising from a mixture of FA 18:1(9Z) and FA 18:1(11Z) standards, highlighting the *m/z* 505 product composed of interfering signals from the two isomers. (C) Calibration curve built from the ratio of the sum diagnostic ion intensities ($I_{(m/z\ 453+\ m/z\ 471)}/I_{(m/z\ 481\ +\ m/z\ 505)}$) versus concentration ratio of FA 18:1(9Z) to FA 18:1(11Z) ($Conc._{(9Z)}/Conc._{(11Z)}$) displays poor linearity.

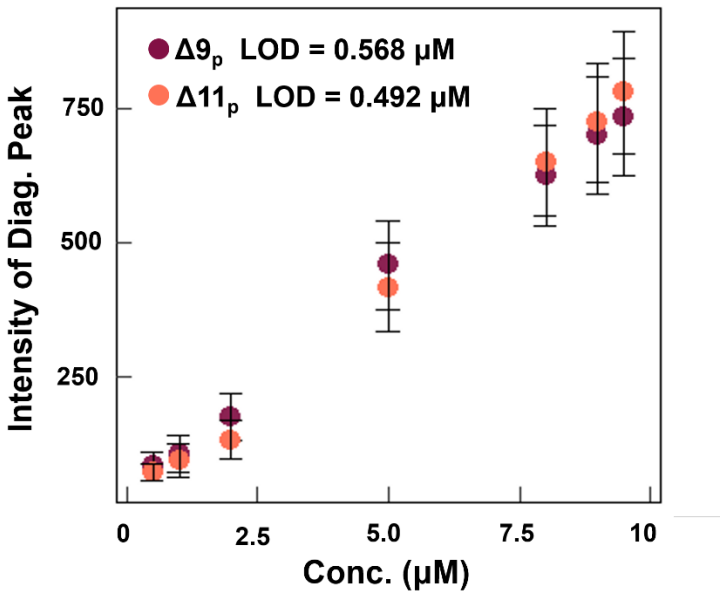

Figure 4.8. Calibration curves for the 9Z and 11Z proximal ions to determine limits of detection for reliable relative quantification of FA isomers during DESI-UVPD-MS.

an increasing linear response with increasing concentration of the 9Z isomer in the mixture, as would be expected if the fragmentation efficiency of the two isomers is equal. Deviations from linearity can be primarily attributed to lower overall signal intensity of diagnostic peaks within the DESI-MS data, which is ~5% of the signal intensity achieved by ESI. Additionally, as no averaging was used in order to more closely resemble DESI-MS imaging data where each pixel represents one mass spectrum, the standard deviation of the 9Z:11Z ratio within each spot is higher than what was obtained by direct infusion. Nevertheless, the linearity of the ratio concentration suggests DESI-UVPD of FA●DC complexes can be used for relative quantification of double bond isomers, as demonstrated in the next section.

4.3.5 Investigation of double bond localization in human breast cancer subtypes

Dysregulation of FA synthase resulting in overexpression of free FA has been associated with a variety of cancers, including breast carcinomas.[94,146] A few MS studies on mouse and human breast tissues have investigated the altered FA 18:1 isomer distribution within normal and cancerous breast tissue. For example, Xia and coworkers found significant differences in the 9Δ:11Δ ratio in FA 18:1 containing glycerophospholipids between normal and cancerous human breast tissues as well as alterations in the free FA 18:1 9Δ:11Δ ratio from mouse breast tissue.[106,134] However, further evidence has suggested that FA metabolism is altered with respect to other factors within breast cancer, including subtype, receptor status, and lymphatic system invasion.[95,147] Therefore, we aimed to use DESI-UVPD-MS to evaluate the FA 18:1 isomer distribution within breast carcinoma tissues related to various molecular and clinical features, including ER status, PR status, and metastatic status (invasion seen in sentinel lymph nodes).

A sample set of 18 breast tumors with detailed diagnosis and molecular subtyping information was used to classify samples into groups (Table C.2). Note that ER and PR status were not available for two samples, yielding a smaller sample set for those analyses. DESI-UVPD-MS imaging was performed while targeting the DC●FA 18:1 complex. Samples were subsequently H&E stained and evaluated by a pathologist to determine areas of breast tumor. Breast tissue is notoriously heterogeneous, displaying normal, cancerous, necrotic, and fat tissue within each section, but the use of DESI-MS imaging allows extraction of mass spectra from tissue regions with predominant tumor content to ensure unambiguous correlation between molecular information and histologic diagnosis. The log 9Δ:11Δ ratio was calculated for each pixel and separated by three distinguishing features of the sample: metastatic vs. non-metastatic to sentinel lymph nodes, ER+ vs. ER-, and PR+ vs. PR-. Per-pixel density plots for each of these evaluations are shown in Figure 4.9A, B, and C**.** The means for each sample distribution and the mean difference for each evaluated parameter were calculated. All three sample sets showed separation in mean difference between the two groups (-0.018 for metastatic vs. non-metastatic, 0.109 for ER+ vs ER-, and 0.211 for PR+ vs PR-), but both the metastatic and ER status density plots contained shoulders that suggested incomplete separation of the groups. Non-parametric permutations of the samples were performed for each parameter to generate a random sampling of the possible mean difference values for these sample sets and determine the significance of the observed mean differences. Histograms of the randomly generated mean differences with the observed difference value shown as a red dotted line for each sample set are provided in Figure 4.9D, E, and F. Interestingly, PR status was the only mean difference that was statistically significant ($\alpha = 0.0187$) from the generated distribution with a p value of 0.003, showing an increased relative abundance of the Δ11 isomer within PR+ samples compared to PR-

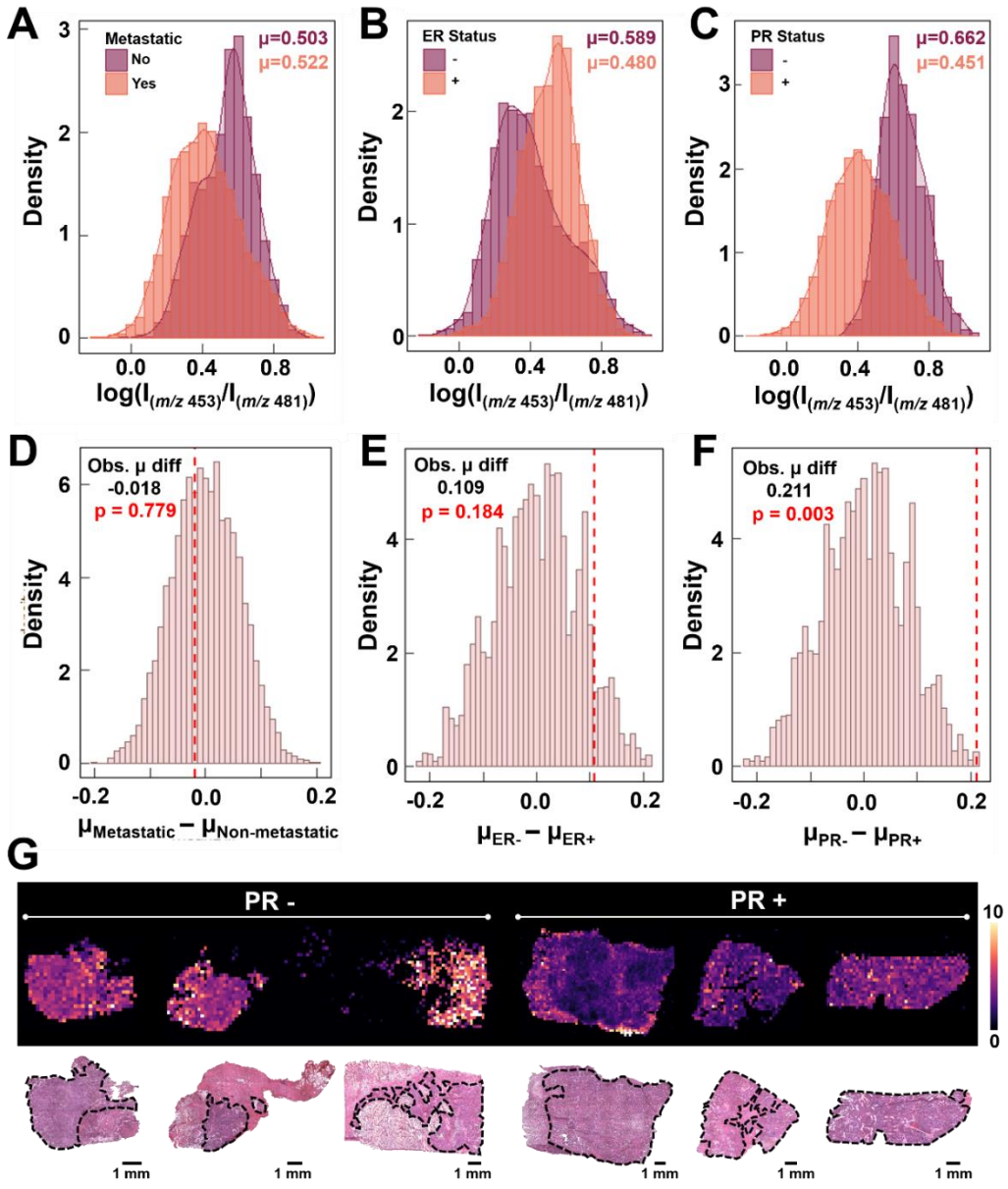

Figure 4.9. DESI-UVPD-MS imaging of FA 18:1 isomers in breast cancer tissue subtypes Density plots of the log of the $9\Delta_p$:$11\Delta_p$ diagnostic peak intensities for (A) metastatic (B) ER and (C) PR statuses. Histograms from the non-parametric permutation of the mean difference of the $9\Delta_p$:$11\Delta_p$ diagnostic ion abundances and the observed mean difference (red line) for the (D) metastatic, (E) ER, and (F) PR groupings. (G) DESI-UVPD MS $9\Delta_p$:$11\Delta_p$ ratio ion images of three PR- and three PR+ breast cancer samples, showing an increased ratio for the PR- samples.

samples. The ion images of the $9\Delta_p$:$11\Delta_p$ ratio from 6 representative samples, 3 PR+ and 3 PR-, allows for visual confirmation of this difference (Figure 4.9G), with PR+ samples exhibiting a decreased $9\Delta_p$:$11\Delta_p$ ratio and thus an increased relative abundance of the 11Δ isomer. For example, the two images within the center for Figure 4.9G have drastically different $9\Delta_p$:$11\Delta_p$ ratios, with the PR- sample having an average ratio of 7.3 while the PR+ sample had an average ratio of 2.2. This increase in the relative abundance of the 11Δ isomer in PR+ samples is consistent with previous studies correlating positive PR status with FA synthase overexpression.[96] These results suggest that FA isomer distribution is not only related to molecular alterations between normal and cancerous breast tissues as suggested in studies performed with other MS methods, but may also correlate with aberrations in molecular processes that occur in breast cancer subtypes as determined by receptor status. Further studies are being performed to validate these trends and expand our sample set to include a larger sample cohort to adjust for patient-to-patient variability and diverse sample populations.

4.4 CONCLUSIONS

Mounting evidence correlating subtle structural variations in lipids with disease state demands development of methods capable of both distinguishing isomeric biomolecules and identifying the biosynthetic dysregulation of the molecules in question. To this end, UVPD was coupled with reactive DESI to enhance structural lipidomics in an imaging workflow. Synergistic charge inversion via reactive DESI augmented the capabilities of UVPD for FA isomer distinction, while permitting the distribution of structural isomers to be spatially resolved without time-consuming off-line chemical derivatization. When applied to unravel FA composition of diseased tissues, this technique revealed molecular trends that are directly tied with molecular properties of the

sample. Using this method for the analysis of human breast tumor tissues suggested that alterations in the FA isomer abundance may be correlated to other clinically relevant factors in breast cancer such as PR receptor status, an outcome that merits further investigation. Further exploration of the relationship between FA synthase, FA isomer abundance ratios, and the importance of these factors within breast cancer and breast cancer subtypes is necessary to further understand the role FAs play in disease progression and patient outcome. A drawback of the current implementation of this methodology is the limited sensitivity when compared to that achieved through ESI infusion-based workflows. Alternate strategies to maintain the sensitivity of ESI without compromising the histological certainty that MS imaging allows such as a laser capture microdissection-LCMS workflow, however, could be implemented to further explore the tissue dependent isomer abundances detected in this study. Nevertheless, DESI-UVPD-MS allows for spatially resolved FA isomer information without significant deviations from a traditional DESI-MS workflow, presenting a useful tool for the exploration of isomeric alterations within tissue samples.

Chapter 5: Molecular Imaging of Endometriosis Tissues using Desorption Electrospray Ionization Mass Spectrometry[4]

5.1 INTRODUCTION

Endometriosis is a debilitating disorder affecting approximately 10% of women within their reproductive years.[148,149] The disease is characterized by the uncontrolled growth of endometrial tissue that lines the uterine walls into other areas of the body, typically within the abdominal cavity.[150] Endometriosis often causes severe and chronic abdominal pain and subfertility, resulting in decreased quality of life for the patient and increased healthcare costs.[151] Despite its prevalence and the detrimental effects this disease has on patients and the healthcare system, endometriosis remains an extremely perplexing disease.[152] Compelling theories on the cause of endometriosis have been proposed, although the biological mechanisms driving endometriosis development are not entirely known, making disease diagnosis and management challenging.[153,154] Further, as diagnostic biomarkers have not been identified and validated, patients are typically diagnosed at the time of laparoscopic surgery, which is the main treatment option for endometriosis patients.[155,156] Endometriosis diagnosis is confirmed by post-operative pathologic evaluation of excised tissue upon visualization of two of the three characteristic histological features: endometrial glands, endometrial stroma, and hemosiderin. Endometrial glands and stroma found in lesions are direct evidence of endometrial tissue outside the uterine cavity and are histologically indistinguishable from the glands and stroma found within healthy uterine endometrium.[157] Conversely,

[4] Adapted with permission from "Feider, C. L.; Woody, S.; Ledet, S.; Zhang, J.; Sebastian, K.; Breen, M. T.; Eberlin, L. S., Molecular Imaging of Endometriosis Tissues using Desorption Electrospray Ionization Mass Spectrometry. *Scientific Reports* **2019,** *9* (1), 15690.Copyright 2019 Springer. C.L. Feider performed data collection and analysis and prepared the manuscript. S. Woody performed statistical analysis of the data. S. Ledet performed pathological evalutation of samples. J. Zhang assited with data collection. K Sebastian and M.T. Breen performed sample collection. L.S. Eberlin assisted with editing and preparation of the manuscript. All authors revised the manuscript.

hemosiderin is an iron-storage complex typically observed in tissue following hemorrhage and is associated with various diseases. Thus, hemosiderin is typically considered as a supporting but not a confirmatory histologic feature of endometriosis.[158]

Several studies have suggested that dysregulation of biochemical pathways is a significant factor in endometriosis.[159-161] Chan and coworkers, for example, reported upregulation of sphingolipid metabolism in endometriosis, leading to an accumulation of glucosylceramides and ceramides within the serum and peritoneal fluid of endometriosis patients.[160] Further investigation of molecular alterations of endometriosis tissues could yield new insights into the pathophysiology of the disease while identifying potential biomarkers for preoperative diagnosis and therapy. To this end, mass spectrometry (MS) provides a powerful platform to investigate the molecular composition of biological samples and alterations occurring in a variety of diseases.[162-164] In particular, MS has been used to determine alterations in metabolites, lipids, and proteins in serum, plasma, follicular fluid, urine, peritoneal fluid, and tissue biopsies obtained from endometriosis patients.[165-171] For example, Cordeiro *et al.* recently used electrospray ionization to analyze lipids extracted from follicular fluid of ten endometriosis patients as well as ten healthy controls and determined significant alterations between the lipid profiles of the two groups.[165] Similarly, Li *et al.* applied liquid chromatography (LC) coupled to MS to analyze lipid extracts of eutopic endometrial biopsies from 21 patients with endometriosis and 20 patients with unrelated infertility, and identified 5 potential lipid biomarkers that were capable of identifying endometriosis with 90.5% sensitivity and 75.0% specificity.[171] Nevertheless, the intricacies of endometriosis often complicate identification of biomarkers causally related to the disease. Endometriosis patients often suffer from other diseases such as autoimmune and endocrine disorders, and present increased risk of gynecological cancers[172-174] This comorbidity typically results in poor

sensitivity and specificity of endometriosis biomarkers, making biomarker discovery difficult.[175] Additionally, the heterogeneous histologic nature of endometriosis lesions presents a challenge for traditional MS analysis, as homogenization of tissue specimens prior to MS analysis leads to mixing of lesions with surrounding tissues, potentially affecting the assay specificity for biomarker identification.

MS imaging presents an intriguing approach to study endometriosis tissues. MS imaging enables two dimensional analysis of biological samples, yielding spatially resolved molecular information that can be unambiguously correlated to histologic features.[176] In particular, MS imaging is powerful for the analysis of heterogeneous tissues, as pixel-by-pixel analysis allows segregation of tissue regions, thereby increasing statistical power to investigate discerning molecular features within regions of interest.[177] The most widely used MS imaging technique, matrix assisted laser desorption/ionization (MALDI),[178] has been successfully implemented towards the analysis of biological tissues and the detection of various diseases. Alternatively, desorption electrospray ionization (DESI) is an ambient ionization MS imaging method in which a spray of charged solvent droplets is directed towards a sample surface to desorb, ionize, and transport molecules to the mass spectrometer for analysis.[179] DESI requires minimal to no sample pretreatment and as a soft ionization technique enables ionization and detection of intact molecular ions.[18] Further, histologically compatible DESI solvent systems allow direct comparison of molecular ion images with histological tissue features on the same tissue section for improved data correlation.[21] Here, we describe a MS imaging study utilizing DESI-MS to spatially and chemically characterize ectopic endometrium from endometriosis lesions and eutopic endometrium prospectively collected from endometriosis patients with the aim of investigating the metabolic differences between eutopic and ectopic endometrial tissues.

5.2 Materials and Methods

5.2.1 Tissue sample collection

Human endometriosis lesions (n = 234) and eutopic endometrial tissue (n = 35) were prospectively collected from 89 patients undergoing both conservative and radical endometriosis surgeries by Dr. Michael T. Breen at Dell Medical School. Tissues were collected under approved IRB protocols from both the University of Texas IRB and the Seton Family of Hospitals IRB. Informed consent was obtained from all patients participating in this study. All endometriosis lesions samples were excised using unipolar electrical scissors during a laparoscopic procedure, while eutopic endometrium samples were collected only from patients undergoing full hysterectomy using a standard scalpel after the completion of the procedure. Samples were stored at 4 °C in airtight containers atop moist gauze until they could be flash frozen in liquid nitrogen, typically within 6 hours of excision. Samples were then stored in a freezer until sectioned. Tissue samples were sectioned at 16 µm thick sections using a CryoStar NX50 cryostat (Thermo Scientific, Waltham, MA) and thaw mounted onto glass microscope slides. After sectioning, the glass slides were stored in a −80 °C freezer. Prior to MS imaging, the glass slides were dried in a desiccator for ~15 min.

5.2.2 Chemicals

The acetonitrile and dimethylformamide used for the DESI-MS spray solvent were purchased from Fisher Scientific (Waltham, MA) and Sigma Aldrich (St. Louis, MO), respectively. All solvents used for histological staining, including methanol, hematoxylin, bluing reagent, eosin y, ethanol, and xylenes were purchased from Fisher Scientific (Waltham, MA).

5.2.3 DESI-MS imaging parameters

All experiments performed were carried out in accordance with the approved IRB protocol. A DESI 2D system (Prosolia Inc., Indianapolis, IN) was used for tissue imaging at a pixel size of 100 μm. DESI-MS imaging was performed in the negative ion mode from *m/z* 100–1500, using a hybrid LTQ-Orbitrap Elite mass spectrometer (Thermo Scientific, San Jose, CA) at 60,000 resolving power (at *m/z* 200) using dimethylformamide:acetonitrile 1:3 (v/v) at a flow rate of 1.4 μL/min unless otherwise stated. The approximate time-per-scan was 1.24 seconds with a stage speed of 94.3 μm/s. The mass accuracy obtained was <10 ppm. All DESI-MS spectra shown throughout the manuscript are an average of approximately 5 scans. Ion images were assembled using Biomap (Novartis) software. The ion images were made using the absolute ion intensity counts from the spectra, with 6000 counts corresponding to 100% relative abundance. The ion images were smoothed using the interpolate function within BioMap. All DESI-MS imaging data is available on METASPACE.[180]

5.2.4 Histopathology and light microscopy

The same tissue sections analyzed by DESI-MS imaging were stained using standard hemotoxilyn and eosin (H&E) staining protocol. Pathologic evaluation was performed by Dr. Suzanne Ledet. Regions of definite and probable endometrial stroma, endometrial glands, and hemosiderin were located within the endometriosis lesions. Eutopic endometrial tissue was confirmed by pathology and regions containing pure endometrial tissue were noted. Light microscopy images of the H&E stained slides were taken using the EVOS FL Auto Cell Imaging System (Invitrogen, Thermo Fisher Scientific, Waltham, Massachusetts, USA).

5.2.5 Identification of molecular ions

Metabolite and lipid species were identified using high mass accuracy measurements and collision induced dissociation (CID) and high-energy collision induced dissociation (HCD) tandem MS analyses, performed using the Orbitrap as the mass analyzer of the LTQ-Orbitrap Elite mass spectrometer. Fragmentation was performed by rastering the DESI source over serial tissue sections at an increased flow rate (3 µl/min). The isolation window used was 1 *m/z* with an energy ranging from 10–30 normalized collision energy for CID and 40–90 for HCD. Fragmentation patterns were compared to literature reports and compared to data from Lipidmaps (www.lipidmaps.org) and Human Metabolome Databases (www.hmbd.ca). Lipids were characterized by fatty acid composition, but the stereochemistry of the chains and double bond position is unknown.

5.2.6 Statistical analysis

A total of 22 of the 35 eutopic endometrial tissue sections analyzed and 76 of the 196 ectopic endometriosis tissue sections analyzed from a total of 51 patients (Table D.1) contained endometrial stroma and thus could be used for statistical analysis. Lasso statistical analysis of the DESI-MS imaging data was performed to build a classification method capable of distinguishing between eutopic and ectopic endometrial tissue, identify biological features of greatest importance within this classification model, and evaluate if the molecular alterations of endometriosis are independent of lesion location. MS imaging data was converted to an mzML format using MS Convert (version 3.9.11748) and imzML format using imzMLConverter (version 1.3) opensource software programs without the addition of any data filters.[181,182] DESI-MS imaging data from pure histological regions of endometrial glands and stroma from endometriosis lesions and

endometrial tissue were extracted using MSiReader software.[183] The *m/z* range was discretized by performing hierarchical clustering and cutting the resulting dendrogram at distance 0.05. Peaks appearing in more than 10% of the pixels were retained for analysis, and intensities for each spectrum were normalized by their median non-zero intensity. The samples were randomly divided into training, validation, and test sets of samples. A logistic regression model was constructed using lasso regularization36 with the glmnet package in the R programming language,[184] and the lasso complexity penalty was selected using five-fold CV. The first penalization parameter selected yielded a model containing 6 background ions, potentially due to batch effects incurred during the analysis. To alleviate this, we considered models using a larger complexity penalization parameter resulting in fewer selected features, even if their performance in CV was lower than the original selected model. The final model was selected to optimize the overall PPA, NPA, and accuracy of the training and validation sets, while minimizing the ratio of background ion to tissue-specific features. To evaluate the performance of the final selected model, PPA, NPA, and overall agreement of the test set is reported. In our study, PPA describes the true positive rate for the identification of ectopic endometrial tissue while NPA describes the true negative rate.

The same preprocessing methods used for the lasso statistical analysis were also used for the bootstrap empirical Bayes analysis, including hierarchical clustering, peak filtering, and normalization. After preprocessing, we calculated the log-ratio of mean intensities between the two groups. Then, we used the bootstrap method to estimate standard errors for these log-ratios. Specifically, for one bootstrap sample of the log-ratio of mean intensities for one feature, we resampled with replacement the intensities for that feature from all pixels, retaining the group label. The z-values were calculated as the observed log-ratio of mean intensities, divided by their standard error. The observed test

statistics and their standard errors are shown in Figure D.1, and it is clear that the vast majority of features are statistically significantly different from zero, when considering the traditional sharp null hypothesis of no difference in mean intensity between the two groups of pixels. Therefore, we then carried out an empirical Bayes analysis to detect "interesting" features.[185] Briefly, this approach assumes a two-groups model for observed test statistics, that features are either "interesting" or "uninteresting," and that both groups of features have a corresponding distribution, called the alternative and null distributions, respectively. This deviates from the usual approach of sharp hypothesis tests of no difference in expression level. We estimate the null distribution empirically, assuming it is normally distributed, and we use moment matching from the middle two quartiles of test statistics to estimate the mean and variance of this normal distribution. The full mixture density is estimated using a spline interpolation of a histogram of all the test statistics (Figure D.2). The prior probability of features being "uninteresting" is estimated using these two estimated densities. From these components we calculate the local FDR, or posterior probability of being "uninteresting," for each feature, and report features for which the local FDR is less than 20%.

Principal component analysis (PCA) was used to evaluate quantitative differences in the data owing to subtype. Intensities for each mass spectra were normalized by the median-log non-zero intensity to account for higher intensity peaks showing higher variance, and thus poorly representing the overall variance in the spectra.[186]

5.3 Results and Discussion

5.3.1 Molecular imaging of endometriosis lesions and eutopic endometrium

A total of 269 samples from 89 patients undergoing endometriosis resection laparoscopies were collected for our study: 234 endometriosis lesions excised from a

variety of locations within the abdominal cavity including the peritoneum, serosal regions of organs such as the rectum, ligaments, ovaries, and fallopian tubes as well as 35 eutopic endometrial tissues collected from a subset of patients undergoing full hysterectomies. The tissues were obtained from patients ranging in ages from 19 to 54 years old. Summaries of the patient demographics are provided in Tables D.2 and D.3. No patient exclusions criteria were applied, therefore samples from patients taking hormonal contraceptives to alleviate endometriosis symptoms were included, as well as patients at different time within their menstrual cycles. Of the 234 endometriosis samples, 38 were not analyzed with DESI-MS due to quality control issues such as small sample size (<50 mg) or incorrect gross anatomy tissue diagnosis during surgery.

Figure 5.1A shows selected DESI mass spectra of endometrial stroma from an ectopic endometriosis tissue collected from rectum and eutopic endometrial stroma obtained from two different patients. DESI-MS imaging of the tissue sections allowed detection and subsequent identification of a variety of small metabolites and lipids including free fatty acids (FA), sphingolipids such as ceramides (Cer), and glycerophospholipids, such as glycerophophatidic acid (PA), glycerophosphoethanolamine (PE), glycerophosphoglycerol (PG), glycerophosphoinisitol (PI), glycerophosphoserine (PS), and cardiolipin (CL). Note that lipids species are annotated to reflect the number of carbons within their FA chains followed by their level of unsaturation. Example MS/MS data of glycerophospholipids and metabolites is provided in Figure D.3 and D.4. As observed in the mass spectra, DESI-MS imaging revealed differences in the relative abundances of a variety of molecular ions between eutopic and ectopic tissues. Within the low mass-to-charge (*m/z*) range, the most notable difference between the two tissue types was the intensity of *m/z* 126.905, tentatively identified as iodide, which was considerably higher in the eutopic endometrial sample

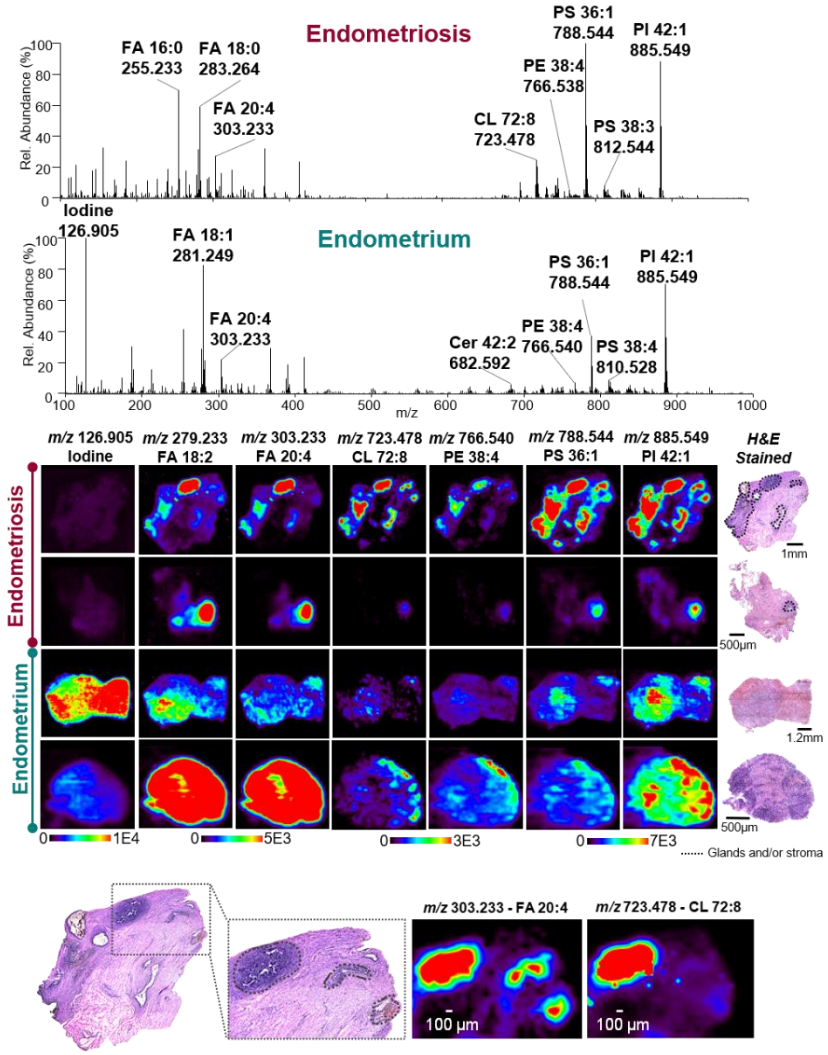

Figure 5.1. Negative ion mode DESI-MS imaging data acquired from endometriosis and eutopic endometrium tissues obtained from different patients.

(A) Selected DESI-MS profiles from the endometrial glands within ectopic endometrial tissue collected from endometriosis lesions (top) and eutopic endometrial tissue from inside the uterus (bottom). The spectra shown are an average of 10 scans. (B) Selected DESI-MS ion images of endometriosis and endometrium tissues. Regions of endometrial glands and stroma within the lesions are outlined in black on the optical images of the H&E stained tissue sections. (C) High magnification view of an endometriosis tissue showing outlined regions of endometrial glands and stroma that spatially correlate to the distributions of various molecular ions detected by DESI-MS imaging, as exemplified by *m/z* 303. 233 and *m/z* 723.478 shown.

when compared to endometriosis lesions. In the higher *m/z* range, the most dominant peak within the mass spectra for the endometriosis lesions is at *m/z* 788.544, identified as PS 18:1_18:0, whereas the most abundant peak in the eutopic endometrium is at *m/z* 885.549, identified as PI 18:0_20:4.

DESI-MS imaging data obtained from eutopic endometrial tissues typically presented a homogenous distribution of molecular ions and thus ion images, reflecting the uniform distribution of endometrial glands and stroma within these tissues. In contrast, DESI-MS imaging of tissues containing endometriosis lesions yielded more heterogeneous images (Figure 5.1B). Upon pathological evaluation of the endometriosis tissues, it was determined that areas containing endometrial glands and stroma as small as 50 µm in size were distributed throughout various tissue types including peritoneum and connective stroma. Endometrial glands presented as hollow structures within the tissue sections surrounded by endometrial stroma and therefore exhibited no lipid or metabolite data. Hemosiderin was also observed with high ion signal intensity in a subset of the endometriosis tissue sections analyzed, further contributing to the spatial heterogeneity in the ectopic endometrial tissues. As seen in the selected ion images in Figure 5.1B, the most intense ion signal observed from various biological molecules in the DESI-MS ion images typically correlated to tissue regions that contained endometrial glands and stroma, while surrounding connective tissue regions presented low cellular density as well as lower ion signal intensity (Figure D.5). Figure 5.1C, for example, shows a higher magnification of an endometriosis tissue obtained from the rectum of a patient, in which high intensities of *m/z* 303.233, identified as FA 20:4, and *m/z* 723.478, identified as CL 72:8, are observed in tissue regions that spatially overlap with endometrial cells (glands and stroma) found within the surrounding serosal connective tissue. There were other tissues and cell types distributed throughout the samples obtained, including

inflammatory and ovarian cells, that yielded higher intensities of lipids and metabolites (Figure D.6) Thus, to assure molecular information from only endometrial cells was being evaluated, we relied on pathological determination of endometrial glands and stroma to precisely locate regions of endometrial cells within endometriosis lesions tissue for comparison to eutopic endometrial tissue. Due to the histological complexity of the tissues and the need to precisely identify regions of pure endometrial cells to extract molecular information, we applied DESI-MS at a spatial resolution of 100 µm. DESI-MS imaging studies using large sample cohorts are often performed at a lower spatial resolution, typically between 150–250 µm.[187] In our study, a spatial resolution of 200 µm was also tested but was not sufficient to clearly define regions of endometrial tissue from the surrounding thus, 100 µm was used.

To evaluate if differences in molecular profiles were potentially related to patient-to-patient variability, eutopic endometrial tissue as well as ectopic endometriosis tissues from various locations within the abdominal cavity were obtained from the same patient and compared. One patient, identified as #98, provided an eutopic endometrial sample as well as four endometriosis tissues collected from the bladder, rectum, left ovary, and an endometrioma. Qualitatively, the trends in molecular profiles detected from eutopic and ectopic endometrial tissues from the same patient appeared to follow similar trends as described for samples from different patients, including an increased abundance of iodide within the eutopic endometrium and higher relative abundance of PS 18:1_18:0 within the endometriosis lesions (Figure 5.3A). The molecular patterns detected in endometriosis lesions also appeared to be consistent and independent of the organ from which the sample was collected. To evaluate and visualize intra-patient molecular differences between the eutopic and ectopic endometrial tissues, principal components analysis (PCA) was performed on the data collected for these five samples. As observed

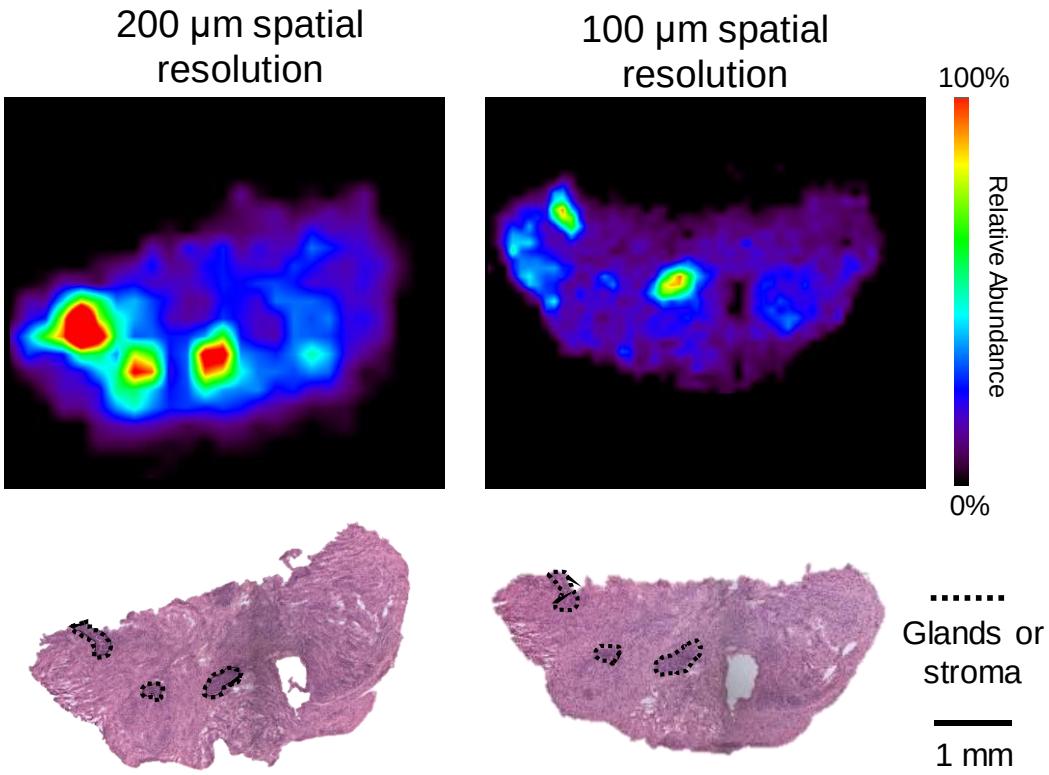

Figure 5.2. Comparison of 2D DESI-MS ion images of *m/z* 885.549 of an endometriosis lesion tissue section at 200 µm and 100 µm spatial resolution.

The solvent used for the 200 µm imaging was 1:1 ACN:DMF at 1.2 µL/min, while the solvent used for the 100 µm imaging was 3:1 ACN:DMF at 1.4 µL/min.

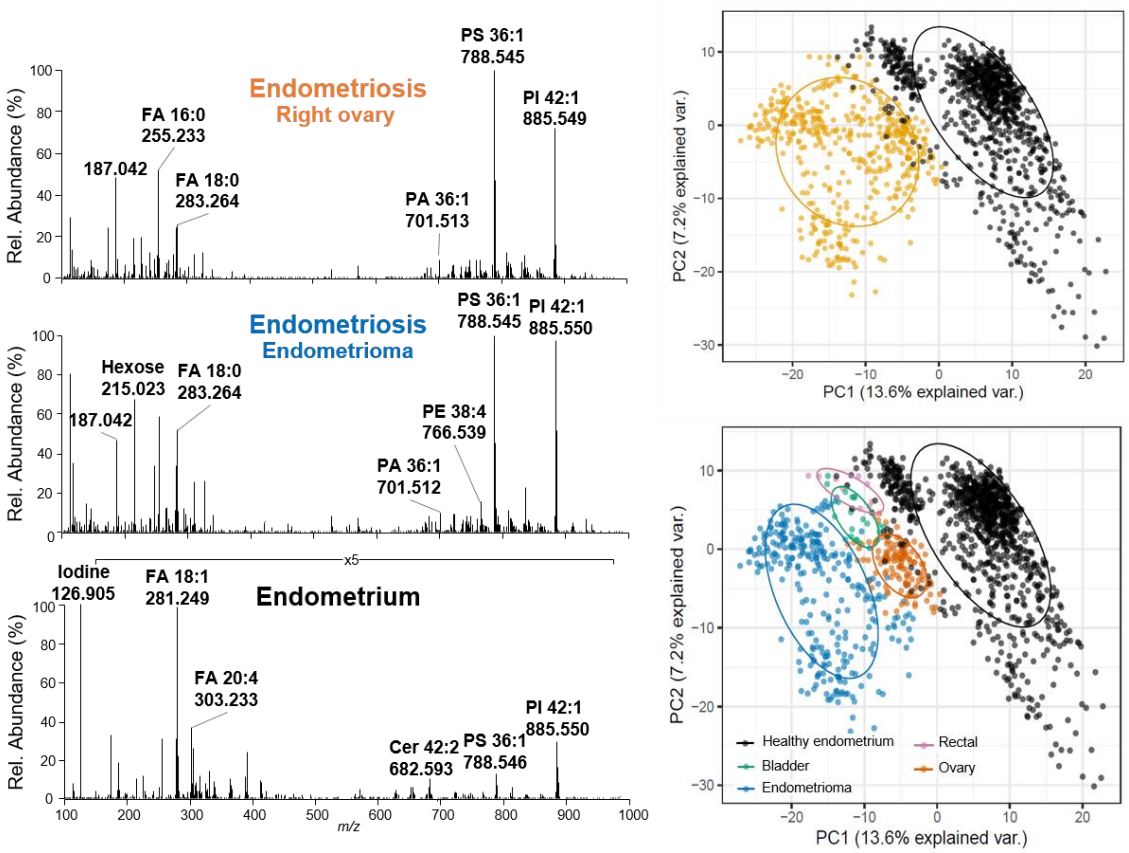

Figure 5.3. Intra-patient analysis of eutopic endometrium and four endometriosis tissues collected from ovary, rectal, bladder and endometrioma (patient #98).

(A) Selected DESI mass spectra obtained from three samples, including endometriosis from both the right ovary and an ovarian cyst (endometrioma), and eutopic endometrium. (B) PCA score plots of the per-pixel data extracted from all endometriosis tissues (yellow) versus eutopic endometrium tissue (black). (C) PCA results of the per-pixel data extracted from endometriosis tissues per region of excision (ovary in orange; rectal in pink, bladder in green, endometrioma in blue) versus eutopic endometrium tissue (black). Ellipses are calculated by a one-sigma ellipse (68% probability) of an estimated bivariate Gaussian distribution for each group.

in Figure 2B, the first two principle components allowed for separation between the data obtained from eutopic and ectopic endometrial tissues. Interestingly, separation was also observed within the data obtained for endometriosis lesions collected from different organs. Similar results were observed from tissues collected from different patients (Figure D.7 and D.8) and analysis of eutopic and ectopic endometrium from the same patient showed clear differences in the molecular pattern yielded by DESI-MS (Figure 5.4), thus suggesting that the molecular changes are associated to biological events rather than patient-to-patient variability such as diet or environmental factors.

DESI-MS imaging experiments further revealed a unique mass spectrum in specific regions of many endometriosis lesion samples. While this mass spectrum was not correlated to any particular histological feature as determined by histopathologic evaluation, it appeared to co-localize to regions of blood deposits in the tissue. The mass spectra exhibited a unique molecular pattern from any other observed in this study with an unusual high relative abundance of ions that are not typically detected from mammalian tissues (Figure 5.5). Ions detected in the higher mass region *m/z* 950–1050 were identified as n-acylphosphatidylethanolamines (NAPE), rare complex lipids that are formed when the amine group on the PE phospholipid headgroup forms an amide bond with a fatty acid. NAPE lipids were observed within this unique mass spectrum among high abundance of PA, PG, and PI lipids that were also detected throughout the rest of the tissue sample although at lower relative abundances. NAPEs constitute about0.01% of mammalian cell membranes and are often correlated to cellular stress conditions such as ischemia and Parkinson's disease.[188] Previously, NAPE lipids were detected by DESI-MS imaging in rat brains tissues that had been subjected to focal brain ischemia, showing the slow increase of these lipids in the ischemic area within24 hr of the stroke, suggesting that these species accumulated during cell death.[189] In our study, these unique molecular

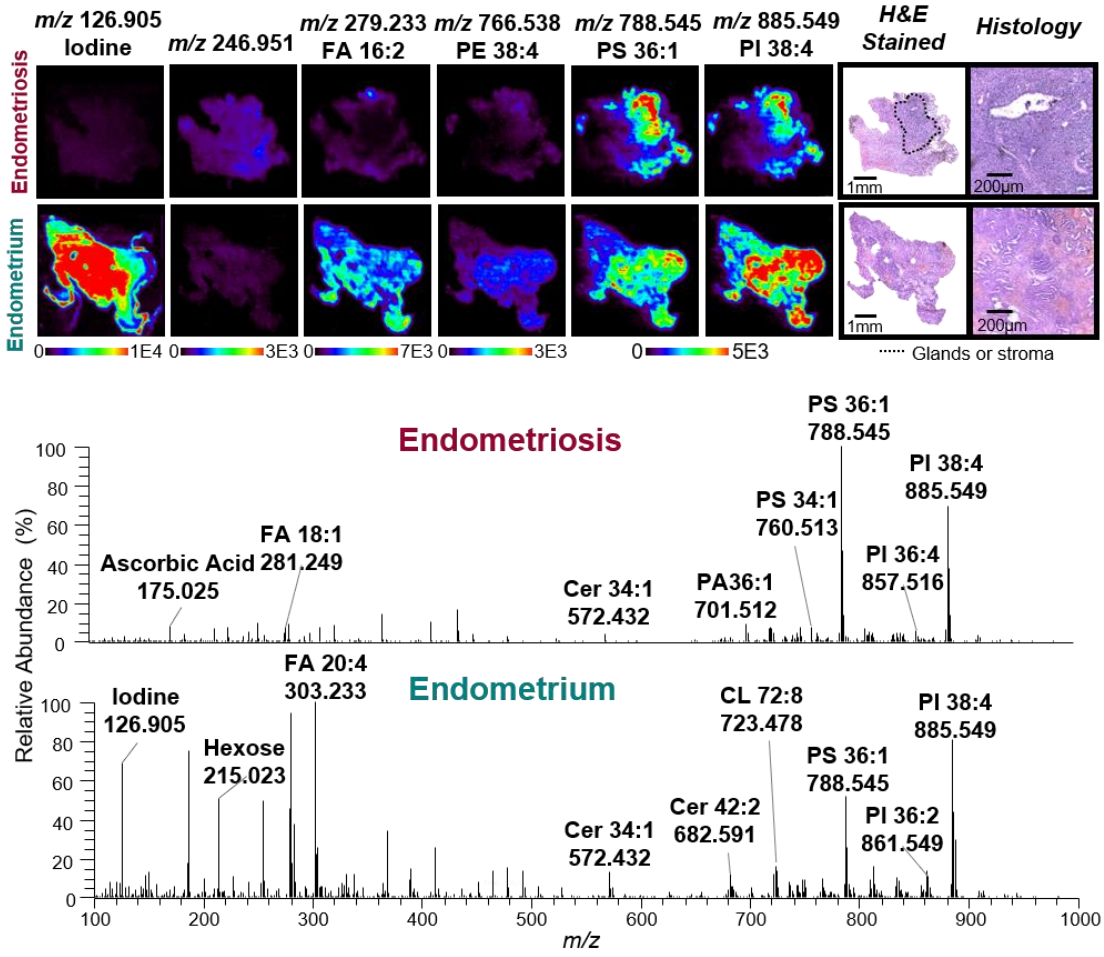

Figure 5.4. DESI-MS imaging data for endometriosis lesions and eutopic endometrium collected from the same patient.

(A) Ion images of endometriosis and endometrial tissue. For the endometriosis lesions, the regions of endometrial glands and stroma within the lesions have been outlined in black on the H&E stained optical images. (B) Lipid and metabolite profiles for ectopic endometrial tissue collected from endometriosis lesions (Top) and eutopic endometrial tissue from inside the uterus (Bottom).

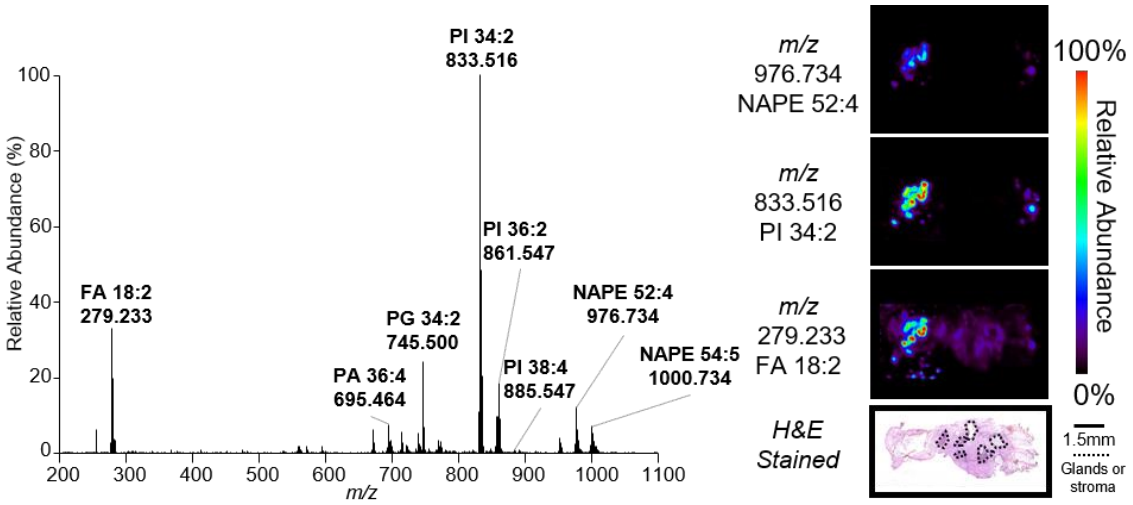

Figure 5.5. Representative DESI-MS spectrum and ion images corresponding to an endometriosis lesion tissue section.

The regions with this unusual molecular profile were characterized by a high abundance of PI, PG, and the rare NAPE lipid species. The regions of endometrial glands and stroma within the lesions have been outlined in black on the H&E stained optical images.

patterns were observed in areas presenting cautery damage incurred during the endometriosis surgery. We thus hypothesize that the cellular damage endured through the electrocautery process induced cell death and caused accumulation of NAPEs and other phospholipid species within the cauterized tissue regions. The localization of these unique mass spectra to areas consisting of blood deposits also suggests the cells affected may be related to the vascular system. While very interesting, the accumulation of NAPE species detected are likely not causally correlated to the presence or absence of endometriosis lesions but rather an external factor and thus were not considered in our statistical analysis, although further investigation is needed.

5.3.2 Statistical classification of endometriosis and eutopic endometrium with lasso

We next used the lasso statistical method to develop classification models that are predictive of the endometrial stroma from endometriosis and eutopic endometrium, identified by pathological evaluation after DESI-MS imaging. Please note that we analyzed 35 eutopic endometrial samples and 196 endometriosis lesions using DESI-MS imaging. However, upon pathological evaluation of the stained tissue sections after DESI imaging, only 22 of the 35 eutopic endometrial tissue sections and 76 of the 196 ectopic endometriosis samples from 51 patients contained endometrial stroma and were used for statistical analysis (Figure 5.6A). A summary of cycle information has been provided for patients whose samples were used for statistics in Table D.4. The distribution of menstrual cycle information was similar for eutopic endometrial samples and endometriosis samples, and thus we do not believe this factor will have a significant impact on our statistical analysis. Some patients contributed multiple samples including tissues of a variety of endometriosis subtypes as well as eutopic endometrial tissues, as described in detail in Table D.1. The MS imaging dataset used for statistical analyses was

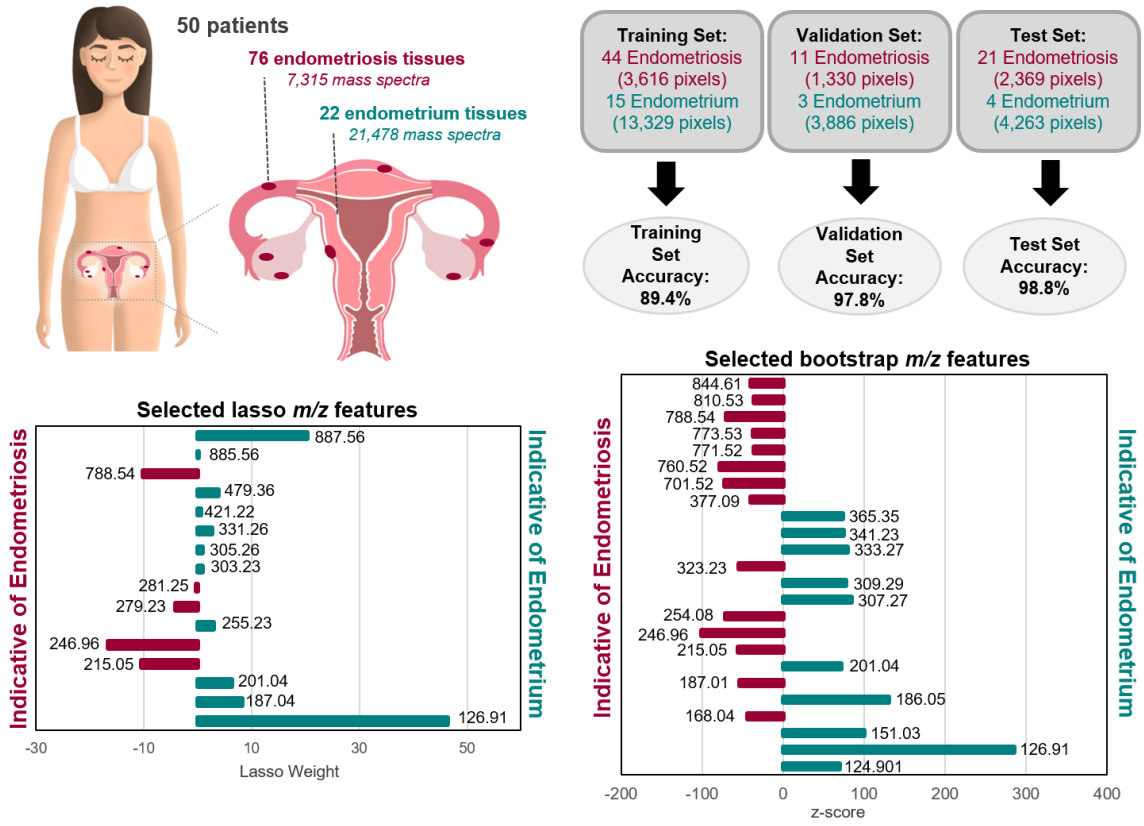

Figure 5.6. Results of statistical analyses performed on DESI-MS imaging data.

(A) A total of 98 tissues including 76 tissues with endometriosis lesions and 22 eutopic endometrium tissues were prospectively collected from 51 different patients. (B) Lasso per-pixel accuracy results for the training, test, and validation sample sets. (C) Features selected by lasso as discriminatory for endometriosis and endometrial tissue, where negative weights are more indicative of endometriosis and positive weights are more indicative of endometrial tissue. (D) Features selected by bootstrap analysis of the same sample set that are indicative of endometriosis or endometrial tissue, where negative z-scores indicate increase abundance in endometriosis and positive z-scores indicate increased abundance in endometrial tissue.

therefore comprised of 28,793 pixels extracted from endometrial glands and stroma within 22 eutopic tissues (21,478 pixels) and 76 ectopic tissues (7,315 pixels). Considering the large number of molecular species detected, we chose to utilize the lasso regularization to construct a logistic regression classifier based on a sparse set of features.[190] The lasso technique has been previously used to create parsimonious and interpretable models with MS imaging data sets that are based on a subset of molecular features that effectively differentiate tissue types.[177] In our study, the samples were split into a training set (n = 59), a validation set (n = 14), and an independent test set (n = 25). The training set was used to train the lasso classification model for distinguishing endometriosis and eutopic endometrium using five-fold cross validation (CV). Optimization of the classifier was performed by optimizing the overall positive percent agreement (PPA), negative percent agreement (NPA), and overall accuracy of the training and validation sets, while maximizing the number of biological features selected.

In the training set evaluation, the lasso model provided a PPA of 96.9% and NPA of 87.3% for diagnosis of ectopic endometrial tissue, yielding an overall accuracy of 89.4% per-pixel. To evaluate possible model overfitting, we then applied the model to a validation set of samples and achieved 93.8% PPA, 99.2% NPA, and an overall agreement of 97.8% per-pixel. Next, we used the model to predict on a withheld, independent test set to further evaluate its robustness. The test set prediction yielded 96.7% PPA, 100% NPA and an overall accuracy of 98.8% per-pixel. Detailed per-pixel and per-sample classification results are provided in Table 5.1, and a summary of the per-pixel results is provided in Fig. 5.6B. On a per-sample basis, where a majority vote from pixel classification within a sample determines the sample diagnosis, four samples were misclassified: one eutopic endometrial sample from the training set and three ectopic endometriosis samples, one from each of the sample sets. Upon further pathologic review

Table 5.1. Confusion matrix of the per-pixel and per-patient statistical results provided by the lasso model for the training, validation, and test sets of samples.

	Analysis	Pathology	Endometriosis	Endometrium	Agreement (%)	Overall Agreement (%)
Training Set	Per Pixel	Endometriosis	3505	111	96.9	89.4
		Endometrium	1689	11640	87.3	
	Per Sample	Endometriosis	43	1	97.7	96.6
		Endometrium	1	14	93.3	
Validation Set	Per Pixel	Endometriosis	1248	82	93.8	97.8
		Endometrium	33	3853	99.2	
	Per Sample	Endometriosis	10	1	90.9	92.9
		Endometrium	0	3	100.0	
Test Set	Per Pixel	Endometriosis	2290	79	98.8	98.8
		Endometrium	0	4263	100.0	
	Per Sample	Endometriosis	20	1	95.2	96.0
		Endometrium	0	4	100.0	

Agreement is the PPA for our model for endometriosis and NPA for our model for the endometrium tissue.

of these samples, the misclassified ectopic endometriosis sample from the test set was determined to be mesothelium rather than endometriosis. Additionally, the misclassified endometriosis sample from the validation set was mixed with hemosiderin tissue. No atypical histologic features were found in the misclassified eutopic endometrial sample or the misclassified endometriosis sample from the training set.

A benefit of the lasso logistic regression method is the selection of predictive features that contribute most heavily to the classification model. The selected endometriosis model consists of 16 tissue specific molecules that allowed for optimal differentiation between these tissue types with varying mathematical weights that signify their contribution to the model (Figure 5.6C). Note that a total of 18 features were selected, but 2 of those were determined to be background peaks and thus not biologically relevant. Of the 16 tissue specific features, 5 were selected as indicative of endometriosis while 11 were more indicative of eutopic endometrial tissue. A list of the selected features, their statistical weights in the model, and their tentative identifications are provided in Table 5.2.

Statistical analyses of the data obtained from eutopic and ectopic endometrial tissues from 51 patients allowed for clear differentiation of these two tissue types and identification of statistically significant molecular markers, thus indicating occurrence of inherent molecular differences between these tissue types despite the histologically similar nature of the stromal cells (Figure D.9).[191]

5.3.3 Selection of interesting molecular features by bootstrap empirical Bayes analysis

While the lasso logistic regression performs feature selection during the construction of the predictive model, it does not necessarily select all features within the

Table 5.2. Lasso weight, detected *m/z* value, proposed identification and mass error for the tissue specific features selected by the lasso model.

Selected feature	Lasso Weight	Observed *m/z* value	Theoretical Mass	Identification	Mass error (ppm)
Indicative of endometriosis					
215.05*	-10.46	215.033	215.0322	Hexose [M+Cl]	-2.3
279.23	-4.07	279.233	279.2330	FA 18:2	-2.1
281.25	-0.27	281.249	281.2486	FA 18:1	-1.8
788.54*	-10.19	788.544	788.5447	PS 18:1_18:0	-0.1
Indicative of eutopic endometrium					
126.91*	46.34	126.905	126.9045	Iodine [M]	-5.5
187.04*	8.21*	187.041		--‡	--
201.04*	6.32	201.038	201.0375	Lactate [2M+Na-2H]	-2.5
255.23	3.01	255.233	255.2330	FA 16:0 [M-H]	-2.4
303.23	0.94	303.233	303.2330	FA 20:4 [M-H]	-2.0
305.26	0.92	305.249	305.2486	FA 20:3 [M-H]	-0.3
331.26	2.67	331.264	331.2643	FA 22:4 [M-H]	-1.8
421.22	0.55	421.226	421.2260	Dioctyl sulfosuccinate [M-H]	-1.9
479.36	3.79	479.356		--	--
885.56	0.19	885.549	885.5499	PI 18:0_20:4 [M-H]	-1.0
887.56	20.34	887.557	887.5566	PI 18:0_20:3 [M-H]	-0.5

‡ Indicates isotope.

Features that were also selected by the nonparametric bootstrap analysis are denoted with an *. Features without a proposed identification, denoted by a – in the "Identification" column, are of unknown origin and may not be biologically relevant, but have been included for transparency.

data set that are significantly different between the two groups if these features do not improve the classification performance. Judging by the out-of-sample predictive accuracy of the final selected lasso model, there appears to be a large number of signals present to distinguish the two groups. Because lasso favors parsimony, the final selected set of features likely does not fully encompass the molecular differences between the groups.

To more comprehensively evaluate these molecular differences between eutopic and ectopic endometrial tissues, we next performed a nonparametric bootstrap analysis using the same extracted data used for the lasso analysis. Here the goal is to search for features that are marginally different in abundance between the groups rather than to build a parsimonious predictive model. As nearly all features were found to be statistically significantly different in mean intensity between the two groups (Figure D.1), with p-values nearly all approximately zero, we carried out an empirical Bayes analysis to find the most "interesting" features, or those that are outliers when compared to the entire population of features in terms of difference in mean intensities.[185] We hypothesize that each feature is either "uninteresting" or "interesting," and each of these two groups of features has a corresponding distribution of test statistics, the null and alternative distributions, respectively. Once these distributions are estimated, as illustrated in Figure D.2, we calculate the posterior probability of each feature being in the "interesting" group of features. We set the target false discovery rate to 20%, yielding the selection of 49 features, 37 of which were determined to be tissue specific (Figure 5.6D). A list of tissue specific selected features, along with their z-scores, posterior probabilities, and tentative identifications are provided in Table 5.3.

Table 5.3. Z-score, detected *m/z* value, proposed identification and mass error for the tissue specific features selected by the nonparametric bootstrap method.

Selected feature	z-score	Observed *m/z* value	Theoretical Mass	Identification	Mass error (ppm)
Increased abundance in endometriosis					
168.04	-44.10	168.031	168.0297	2-furoylglycine [M-H] §	-4.8
187.01	-53.32	187.007	187.0065	P-Cresol Sulfate [M-H] §	-3.7
215.05*	-55.17	215.033	215.0322	Hexose [M+Cl]	-3.7
216.03	-38.29	216.036	216.0356	Hexose [M+Cl] ‡	-3.2
217.03	-52.88	217.030	217.0293	Hexose [M+Cl] ‡	-2.3
254.08	-71.44	254.079	--	--	--
323.23	-54.93	323.220	323.2198	MG 14:0 [M+Na-2H]§	-0.6
377.09	-39.09	377.085	377.0851	Disaccharide [M+Cl]	-1.3
701.52	-72.69	701.512	701.5127	PA 18:1_18:0 [M-H]	-0.4
702.51	-70.29	702.516	702.5161	PA 18:1_18:0 [M-H+1]‡	-0.1
760.52	-77.71	760.512	760.5134	PS 16:0_18:1 [M-H]	-0.5
761.52	-55.92	761.517	761.5168	PS 16:0_18:1 [M-H+1]‡	-0.8
771.52	-36.15	771.518	771.5182	PG 18:1_18:2 [M-H]	-1.8
773.53	-36.72	773.533	773.5338	PG 18:1_18:1 [M-H]	-3.6
788.54*	-70.31	788.544	788.5447	PS 18:0_18:1 [M-H]	-0.1
789.55	-67.87	789.547	789.5481	PS 18:0_18:1 [M-H+1]‡	-0.3
790.55	-67.87	790.550	790.5514	PS 18:0_18:1 [M-H+2]‡	-0.5
791.55	-52.22	791.552	791.5548	PS 18:0_18:1 [M-H+3]‡	-0.8
810.53	-36.11	810.528	810.5291	PS 18:0_20:4 [M-H]	-0.6
811.532	-36.04	811.532	811.5326	PS 18:0_20:4 [M-H+1]‡	-0.6
844.61	-39.92	844.607	844.6073	PS 18:1_22:0 [M-H]	-1.2
845.61	-39.26	845.611	845.6107	PS 18:1_22:0 [M-H+1]‡	-1.1

Table 5.3. (cont.)

Increased abundance in eutopic endometrium					
124.01	69.70	124.008	124.0068	Taurine [M-H]	-6.5
126.91*	285.56	126.905	126.9045	Iodine [M]	-5.5
151.03	100.60	151.026	151.0256	Xanthine [M-H]	-5.3
186.05	130.60	186.046	--	--	--
187.04*	129.78	187.042	--	--‡	--
188.06	114.72	188.062	--	--	--
189.05	90.63	189.058	--	--‡	--
201.04*	71.70	201.038	201.0375	Lactate [2M+Na-2H]	-2.0
307.27	84.25	307.264	307.2643	FA 20:2 [M-H]	-1.6
308.26	69.88	308.268	308.2675	FA 20:2 [M-H+1]‡	-1.3
309.29	77.48	309.280	309.2799	FA 20:1 [M-H]	-1.3
333.27	79.55	333.280	333.2799	FA 22:3 [M-H]	-0.3
341.23	74.55	341.225	341.2245	FA 20:3 [M+Cl]	-3.8
365.34	73.80	365.343	365.3420	Tetracosanedione [M-H]	-1.6

‡ Indicates isotope
§ Identified with exact mass alone due to low abundance or interference with other species

Features that were also selected by the lasso analysis are denoted with an *. Features without a proposed identification, denoted by a – in the "Identification" column, are of unknown origin and may not be biologically relevant, but have been included for transparency.

5.3.4 Biological significant of features selected by lasso and empirical bootstrap analyses

Lasso and bootstrap empirical Bayes analyses allowed identification of 53 tissue specific features as important in characterizing endometriosis and eutopic endometrial tissue. Note that six features were selected by both the lasso and the bootstrap and are noted in Tables 5.2 and 5.3. Additionally, the models selected 13 values that were isotopes of already selected molecular ions and were excluded from the final number of features. Therefore, the total number of distinct molecular features selected by both methods not including duplicates or isotopes is 34. Evaluation of the ions selected revealed trends in the molecular information that may give insights into the biological processes occurring in these tissues. Interestingly, fatty acids play a significant role in our models; shorter acyl chain FA (FA 18:1 and FA 18:2) were more characteristic of endometriosis tissue while longer fatty acid chains with higher levels of unsaturation (FA 20:2, FA 20:3, FA 20:4, FA 22:3, and FA 22:4) were more characteristic of eutopic endometrium. Previous studies have evaluated the effect of polyunsaturated FA, and more specifically omega-3 FA, on the survival of endometrial cells in culture and determined that the presence of certain highly saturated fatty acids suppressed endometrial cell survival. Similarly, serum from women with endometriosis was found to have lower levels of the same polyunsaturated FA, eicosapentaenoic acid (FA 20:5), than the serum of healthy controls.[192] While FA 20:5 was detected at very low relative abundance at *m/z* 301.217 by DESI-MS imaging, a number of polyunsaturated FA with the same acyl chain length were selected as indicative of eutopic endometrium. While we are currently unable to determine if the polyunsaturated FA within our data are omega-3 fatty acids due to inability of traditional MS fragmentation methods to determine double

bond position, this strengthens the hypothesis that highly unsaturated FA may be at decreased levels in endometriosis lesions.

Studies have suggested that molecular events related to dysregulated phospholipid and sphingolipid metabolism play a role in endometriosis pathogenesis.[160,165,169,170,193-195] In particular, glycerophosphocholine (PC) species have been detected at altered levels in biological specimens from endometriosis patients when compared to healthy controls.[169,193-195] For example, Vouk et al. found the upregulation of 5 PC lipids in the serum of patients with endometriosis but later found 4 different PC species downregulated in the peritoneal fluid of endometriosis patients compared to controls. Most of these studies were performed using MS in the positive ion mode, in which zwitterionic PC, sphingomyelins, and PE lipids are more easily detected, while our study was performed in the negative ion mode, which favors detection of phospholipids with negatively charged headgroups. A previous study reported higher abundance of a potassium adducted PS species within the follicular fluid of control patients compared to patients with endometriosis.[165] In contrast, multiple PS species including PS 16:0_18:1, PS 18:1_18:0, PS 18:0_20:4, and PS 18:1_22:0 were selected as indicative of endometriosis tissue rather than eutopic endometrium in our statistical models. PS are typically confined to the inner membrane of eukaryotic cells but are known to be involved in multiple cellular processes including homeostasis and programmed cell death.[196] The upregulation of PS in endometriosis lesions could be a result of increased blood coagulation of the endometrial tissue during or after a woman's menstrual cycle, when the endometrial lining within the uterus is expelled from the body due to a decrease in estrogen levels. Endometriosis tissues respond similarly to hormonal levels but are trapped within the adhesions, which could potentially signal coagulation cascades, triggering exposure of PS on the outer surface of blood platelets.[197] In addition to PS,

multiple PA and PG species were selected by the bootstrap empirical Bayes analysis as having increased relative abundance within the ectopic endometriosis tissue while PI 18:1_20:4 was selected as a feature more indicative of eutopic endometrium.

A variety of small metabolites were also selected as features within our models for endometriosis and eutopic endometrium. For example, hexose, presumed to be glucose due to its abundance within tissue, was selected in its chlorine adducted form as a feature indicative of endometriosis lesions in both models. Previous studies have shown alterations in the glucose transporter proteins in the eutopic endometrium of women with endometriosis and their matching endometriosis lesions, likely associated to different glucose uptake between these cell types.[198] As expected from qualitative evaluation of the mass spectra, iodine was also selected as a feature indicative of eutopic endometrium in both our statistical analyses. The presence of this ion within the eutopic endometrium may be related to the proximity of this tissue to the cervix which is known to contain a high concentration of iodine when compared to other body areas.[199] Additionally, some research studies also suggest that endometriosis is an iodine-deficiency disease and thus would account for the lower levels of iodine within the ectopic endometrium detected in our study.[200] An ion at *m/z* 246.951 was also selected by both the lasso and the nonparametric bootstrap models as indicative of endometriosis. Interestingly, an ion at *m/z* 246.951 has been previously visualized in other DESI-MS imaging studies and suggested a potential indicator of normal tissue when compared to squamous cell carcinoma and lung adenocarcinoma tissues.[201] Based on tandem MS (Figure D.10) and exact mass measurements, we identified *m/z* 246.951 as a heavily fluorinate compound with the molecular formula $C_3HF_6SO_4$. Due to the fluorinated nature of this compound, we hypothesize that this ion corresponds to a drug metabolite from the breakdown of the surgical anesthetic commonly used during endometriosis surgery, rather than an

endogenous molecule. Its presence within our statistical models, while undesirable, is not unexpected considering the untargeted nature of MS imaging analyses and emphasizes the importance of retroactive investigation of the molecules selected by the statistical models using these data sets. Due to its exogenous nature, we have removed this feature from the list of tissue-specific features shown in Tables 5.2 and 5.3.

5.3.5 Clustering of endometriosis lesions by disease subtype

Our statistical analyses were performed under the assumption that all endometriosis lesions would have similar molecular patterns. However, endometriosis subtypes characterized by region of excision may contribute to heterogeneity within the collective data, as suggested by our intra-patient analyses. Endometriosis lesions may be separated into three categories: ovarian, peritoneal, and deep infiltrating endometriosis, depending on where the lesion was located within the body.[202] Researchers have suggested that these categories should be treated as separate entities with potentially different causes, symptoms, and treatments.[175] To address the potential for heterogeneity due to lesion subtype, PCA was performed on all the ectopic endometrium. Figure 5.7 shows the PCA results, with different colors representing different tissue subcategories based on their location within the patients. No separation was seen based on endometriosis subcategory, with extensive amount of data overlap. Further, when faceting the PCA score plot to isolate pixels originating from the same patient sample (Figure D.11), any clustering observed could be attributed to data from the same tissue sample and not subtypes, an observation that was not surprising considering biological variance between patients. These results suggest that the molecular data acquired by DESI-MS imaging in this study does not allow for subtyping based on tissue location

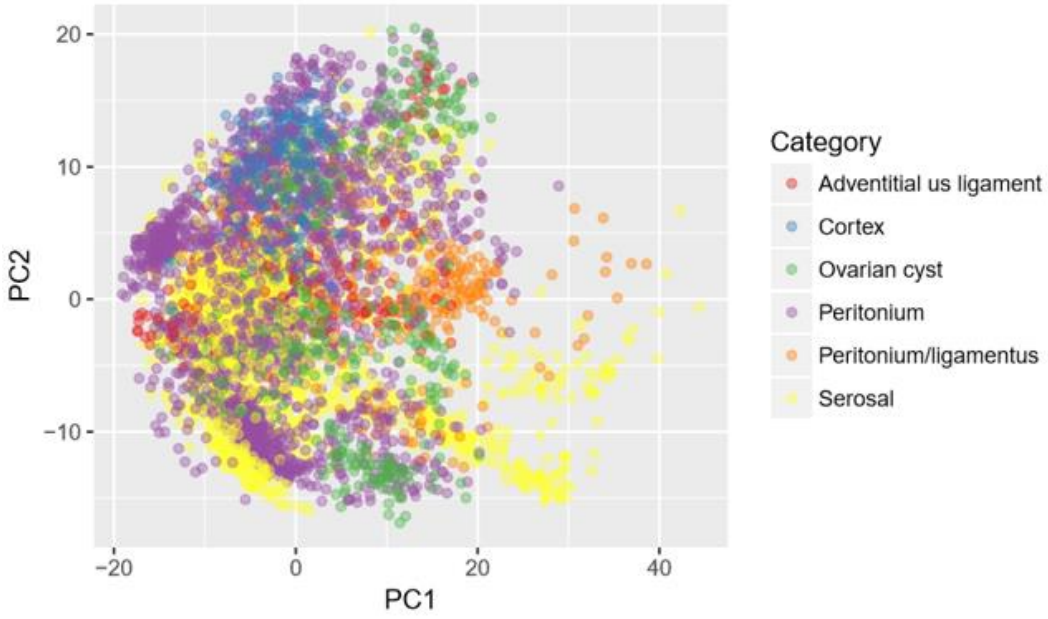

Figure 5.7. PCA score plot of ectopic endometrial tissue, grouped by region of excision, showing minimal clustering based on where the lesion was located in the patient.

across different patients. This observation is also partially supported by the high predictive accuracy achieved by our lasso model in which the data were collectively combined into a single endometriosis class.

5.5 CONCLUSIONS

DESI-MS imaging was used to investigate the spatial distribution and metabolic profiles of the eutopic endometrium and endometrial stroma from endometriosis lesions. While greatly less metabolic coverage is achieved with DESI-MS imaging than traditional MS techniques such as LCMS, the spatial resolution provided by DESI-MS imaging (100 μm) allowed collection of spatially-resolved metabolic information and showcase the usefulness of MS imaging in segregating endometriosis lesions within complex tissues. Despite being histologically similar, DESI-MS imaging and statistical analyses allowed identification of distinct chemical differences between the two tissue types, which could be indicative of biological changes associated with differences between eutopic endometrium and endometriosis lesions. While the biological processes that may be driving these differences are unclear, our results suggest that metabolic differences between these two tissue types exist which could potentially be translated to future discoveries of clinical biomarkers of endometriosis. However, it remains a possibility that these differences between eutopic and ectopic endometrium are due to their immediate environment rather than inherent differences between eutopic and ectopic endometrial tissues. Further, as patients on hormonal treatment were included in our study to maximize sample accrual, metabolic alterations due to hormonal treatment, as previously observed in plasma and serum,[203,204] could have potentially affected the results obtained in our analyses. Although inclusion of tissues from patients on hormonal treatment is a limitation of our study, statistical analysis of the data obtained from tissues

of patients both on and off hormonal treatment for endometriosis should allow selection of metabolic markers that occur within both groups, independent of hormonal treatment. Further studies are planned to evaluate metabolic changes in tissues from endometriosis patients depending on hormonal treatment. Additionally, our study does not determine if the eutopic endometrium from endometriosis patients is molecularly similar to eutopic endometrium from healthy women, as these samples were not available for our study. Future studies to validate and elaborate these findings, including integration of healthy controls, symptom correlation to specific molecular features, and evaluation of other semi-invasive or non-invasive methods for endometriosis detection are currently being pursued.

Chapter 6: Conclusions and Perspectives

Throughout the last two decades, ambient ionization MS methods have proved to be excellent tools for the molecular characterization of biological samples *in situ*, revolutionizing the way in which MS can be used in a clinically relevant context. By allowing for analysis of metabolites, lipids, and proteins directly from clinical specimens, including tissue biopsies, we are closer than ever to being capable of monitoring biological alterations due to disease in real time without harm to patients. However, there remains limitations in ambient ionization techniques that have yet to be fully addressed, preventing further adoption of these technologies outside of an academic setting. The goal of this dissertation was to begin addressing some of these constraints and provide insights into potential avenues for continued advancement so that these technologies may one day be used for the improvement of patient care.

Reliability and consistent performance of technologies used for clinical research applications is of the utmost importance as clinicians rely on accurate and timely results to administer appropriate treatment and ensure positive outcomes for their patients. As with any new methodology, ambient ionization MS techniques must be rigorously tested and validated to ensure that data quality to maintained in a variety of situations. As alluded to in chapter two, the environmental factors that influence the performance and reliability to ambient ionization MS technologies have not been fully explored. Our results suggest that DESI-MS data quality and consistency fluctuate with relative humidity, a previously unexplored factor in the field. As the sampling and ionization of analytes occurs in the open atmosphere for ambient ionization techniques, environmental factors such as relative humidity in addition to temperature, elevation, and ambient air flow may be overlooked variables that need to be controlled. Systematic evaluation of these parameters, as was performed for changes in relative humidity described here,

could reveal insights into the environmental conditions necessary to obtain optimal results when performing ambient ionization MS on biological tissue samples. Additionally, to ensure these technologies are robust and can be relied upon despite alterations in the environment, larger studies performed at multiple sites that include a variety of patient populations must be completed. Differences between healthy and diseased tissue must be large enough to overcome intra-laboratory variable that will be present if these technologies are applied on a larger scale. While some multicenter studies evaluating the performance of ambient ionization techniques for disease discrimination have been performed,[22] a stronger emphasis must be placed on this fact in future work to prove these technologies can truly be applied for clinical problems.

Further advances in the field of ambient ionization MS will most likely be focused on increasing the breadth of information that can be obtained with these technologies. Two approaches towards this objective were discussed within this dissertation. The first was to improve the detection of molecules that are typically detected in low abundance from biological samples by integrating ambient ionization with gas-phase separation techniques. As discussed in chapter three, coupling of a FAIMS separation to both DESI and LMJ-SSP MS facilitated the detection of an increased number and intensity of large, multiply charged biomolecules directly from human tissue. However, this improvement in detection comes with the disadvantage of decreased overall ion signal intensity due to the filtering of ions prior to mass analysis. As many ambient ionization MS methods already suffer from low ion signal intensity, further reduction of the ion abundance is not ideal for many applications. Improvements in sensitivity of mass spectrometers could alleviate some of the effects from this signal reduction, increasing the number of applications that could benefit from FAIMS separation prior to analysis. Improved mass spectrometers have allowed for 7 to 10-fold

increases in the number of protein species detected from biological tissue sections when coupled liquid extraction ambient ionization techniques, and even further improvements were observed with the addition of FAIMS.[205] Increases in the sensitivity of mass spectrometers will allow for the use of ambient ionization techniques in a wider variety of biological applications where sensitivity is an issue. Additionally, while current ion mobility methods allow for gas phase separation of ions to achieve some level of chromatographic separation, the efficiency of these separations is far below that of what can be achieved using more traditional liquid chromatography methods. Further improvements in the separation capabilities of ion mobility technologies would be a significant advancement for the field, particularly if they could allow for the separation of isobars and isomers. Recently, advancements have been made in ion mobility technology that allows for separation of some lipid and peptide isomers with promising results.[206-208] These high-resolution ion mobility systems have yet to be coupled to imaging modalities and have not been applied for the analysis of samples with extremely complex matrices such as tissue sections, but their potential for integration with ambient ionization technologies remains an intriguing avenue for future studies.

Another method for increasing the amount of available information yielded during an MS imaging experiment is to perform fragmentation of an analyte of interest to determine if isomers are present at the same exact mass. As discussed in chapter 4 of this dissertation, tandem MS imaging that can uncover structural information regarding the molecules within a tissue sample can yield new insights into the dysregulation of cellular pathways occurring in diseased tissue. Fragmentation by UVPD has shown particularly useful due to its ability to produce fragments that are diagnostic of structurally relevant components of lipids that traditional collision-based activation methods do not provide. Through the integration of UVPD and DESI-MS imaging we have been successful in the

imaging of lipid isomers within several types of biological tissue sections, allowing for in-depth analysis of double bond positioning differences between normal and cancerous tissue as well as between cancer tissue subtypes.[135] Limitations in this technique, however, prevent application to large sample sets. For example, the combination of the low sensitivity of DESI-MS analyses and the inherent inefficiencies in UVPD fragmentation prevents analysis of lower abundance molecules within tissue samples and requires longer analysis times in order to obtain adequate signal for reliable double bond diagnostic information. This limits the number of ions that can be analyzed for double bond information. Additionally, the software that is currently available for MS imaging applications does not facilitate the separation of multiple tandem MS events during one experiment, thus preventing evaluation of multiple transitions simultaneously. Therefore, to investigate multiple lipids from one tissue sample replicate tissue sections need to be analyzed, greatly lengthening analysis time and preventing analysis of multiple molecules from the same cell populations. Despite these drawbacks, DESI-UVPD-MS imaging of tissue sections is one of a few tools that can allow for spatially resolved imaging of isomer distributions within a sample and limitations could be addressed with improvements in instrument performance and development of software programs capable of separating tandem MS events for imaging applications.

Since their invention in 2004, ambient ionization MS technologies have shown usability in a variety of fields but none more so than for use in clinical applications. Their ability to be implemented in many environments without need for high vacuum sample chambers and lengthy sample preparation steps spurred researcher that could one day be performed at hospitals and clinics. Cancer diagnostics, for example, has been an area of intense investigation with ambient ionization MS, with applications such as breast[22,209], thyroid[27,28,209], and ovarian cancers[25,51], among others, being explored within the last few

years. However, applications outside of oncology that have heterogenous tissue morphology could also be explored with MS imaging technologies. As described in Chapter 5 of this dissertation, DESI-MS imaging was applied for the investigation of metabolic alterations occurring in association with endometriosis. As endometriosis lesions are heterogeneously complex, DESI-MS imaging allowed for spatial targeting of the endometrial cells within the lesions and healthy endometrium tissue. This enabled the development of molecular classifiers that were built using pure cellular environments for direct comparison of these two tissue classes. DESI-MS data collected allowed for excellent distinction between the eutopic and ectopic endometrium tissue and for the identification of statistically significant differences in the metabolite and lipid abundances. Further work is needed to verify these alterations are biologically significant, however, as DESI-MS is typically used as a discovery tool and is not a quantitative technique. Imaging of the protein alterations between these two tissues would allow for an increased understanding of the exact biological pathways that may be dysregulated in endometriosis lesions. While DESI-MS imaging of proteins has recently been shown[210,211], analysis of less abundant protein molecules requires analysis with other MS technologies such as MALDI-MS. Additionally, the use of MALDI-MS would enable even higher spatial resolution during imaging experiments, potentially allowing for the investigation of lipid and metabolite alterations within endometrial glands that can be as small at 20µm. Further analysis of endometriosis stroma from ectopic and eutopic endometrium with quantitative MS techniques, such as LCMS, would also be a valuable exercise to verify metabolic markers selected in this work are significantly altered. These future studies are necessary to continue exploring if MS technologies can yield insights into disease pathogenesis and suggest potential therapeutic targets for disease management.

MS technologies, specifically ambient ionization MS techniques, have the potential to significantly disrupt the diagnostic space with potential applications both in and out of the clinic. As these techniques advance and methods are developed to tackle complex problems facing patients and health care professionals, MS will inevitably become an integral part of many clinical workflows due to the potential benefits these technologies will provide. This dissertation serves as a summary of a small subset of work being done in pursuit of implementation ambient MS methods in a wide variety of healthcare applications. Despite the challenges that remain, strides are being made throughout the field to make ambient ionization tools robust and versatile for routine use to facilitate and improve patient care.

Appendices

APPENDIX A: SUPPORTING MATERIAL TO ACCOMPANY CHAPTER 2

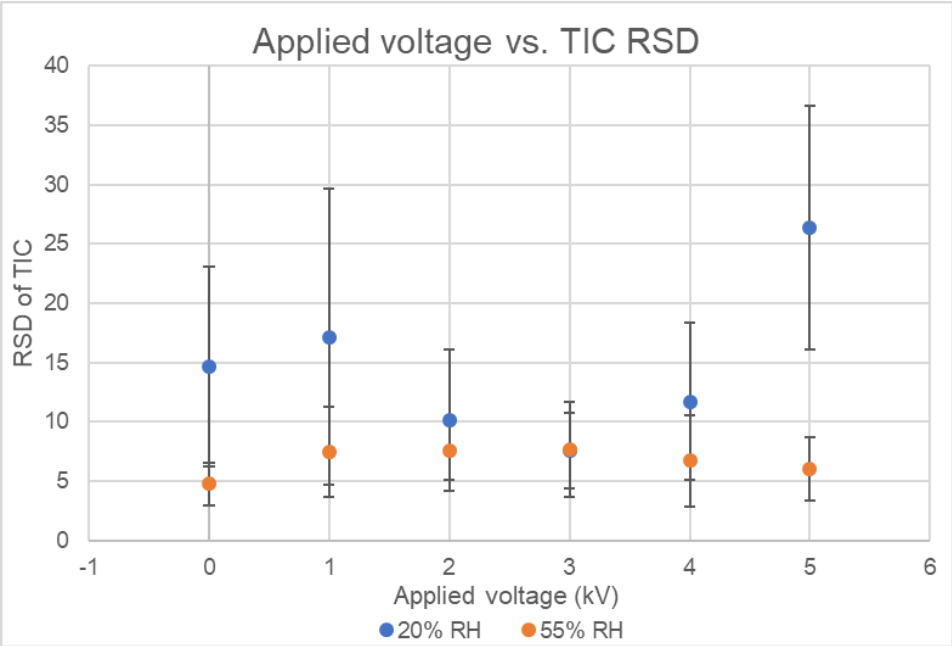

Figure A.1. Voltage vs relative standard deviation of the total ion count at both stable (RH 55%) and unstable (RH 20%) conditions.

The TIC RSD and error bars were determined with using an average of 9 groups of 5 scans from a DESI-MS line during mouse brain tissue analysis. The RSD of the TIC is generally higher and has higher error at low RH%, and the RSD of the TIC is greatest at 5 kV.

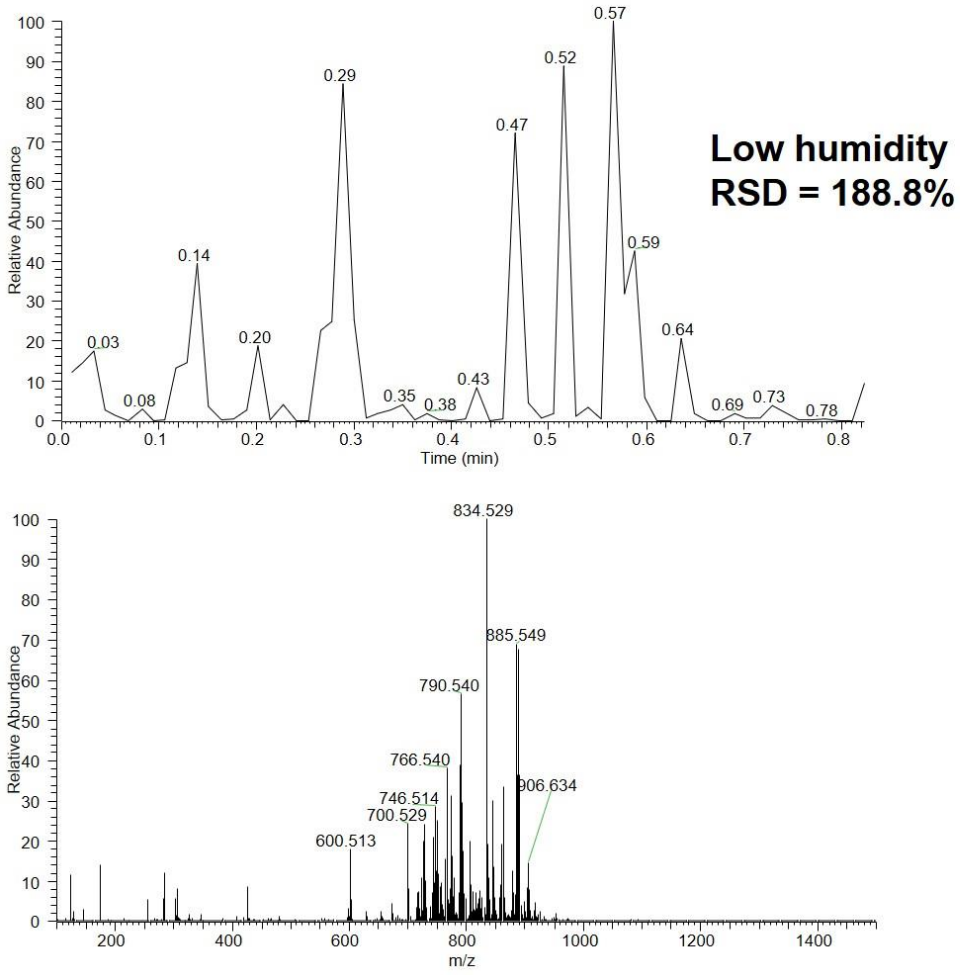

Figure A.2. TIC chromatogram and average spectrum from mouse brain tissue at low RH% using MeOH:H_2O at the DESI spray system

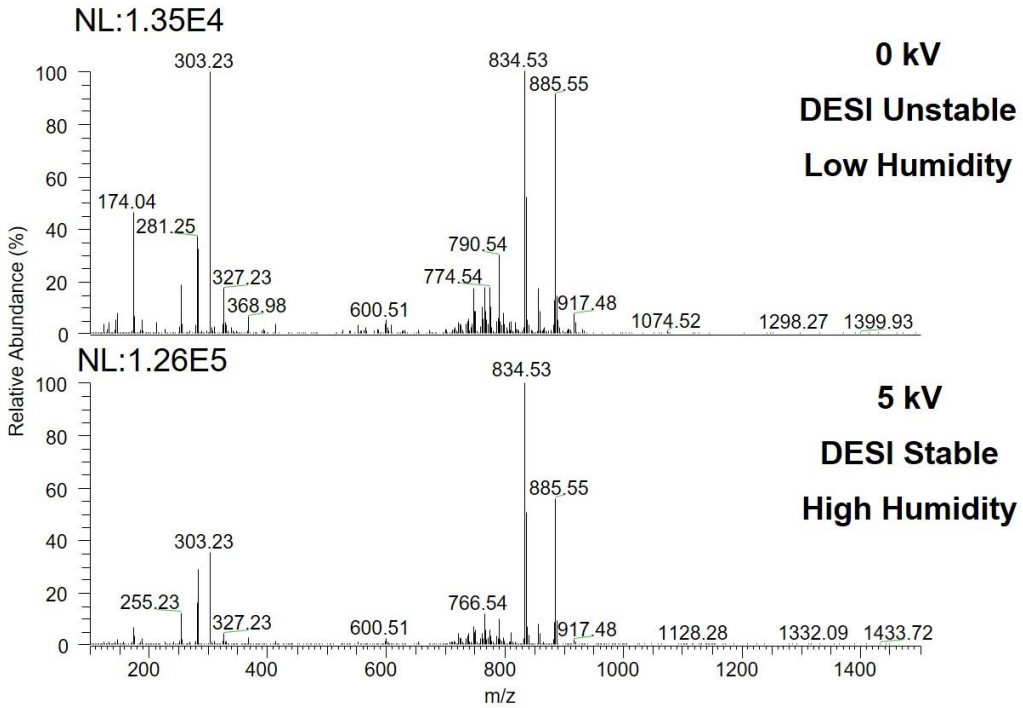

Figure A.3. DESI mass spectra from a mouse brain tissue section at low and high voltage (low RH, 15-30%)

Adjusting the voltage to 0 kV during times of low humidity/unstable DESI-MS improves the signal stability but reduces the overall ion signal intensity when compared to typical DESI-MS ion signal when operating at 5 kV during times of high humidity/stable DESI-MS.

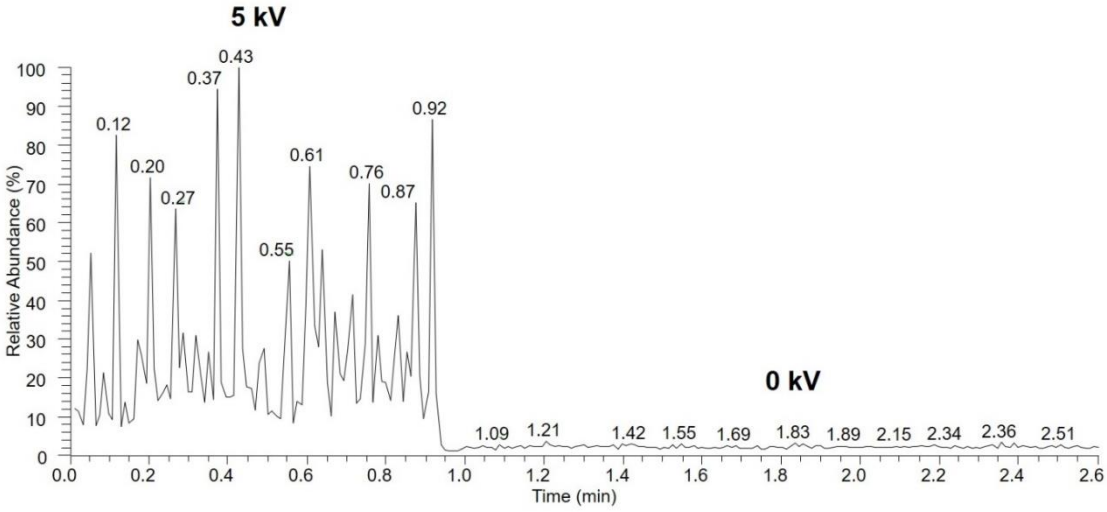

Figure A.4. TIC of RESI analysis of a standard calibration solution at high and low voltage.

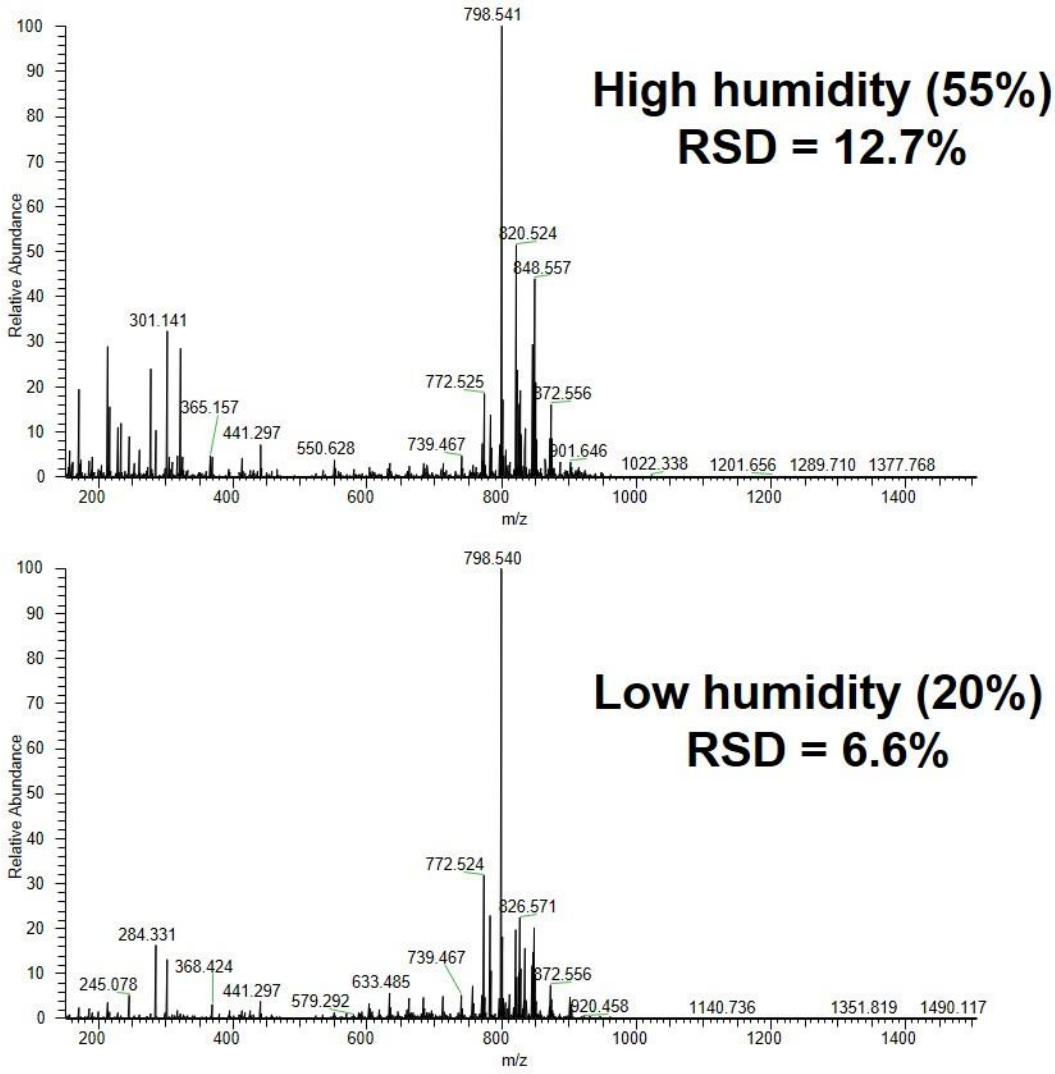

Figure A.5. Representative spectra of DESI-MS of mouse brain in the positive ion mode at both high and low humidity.

There is little difference in the spectra based on the change in humidity in the positive ion mode. However, there is a slight improvement in the signal intensity and RSD at low humidity, suggesting potential RH dependence at different RH levels than that which is seen for negative ion mode.

APPENDIX B: SUPPORTING MATERIAL TO ACCOMPANY CHAPTER 3

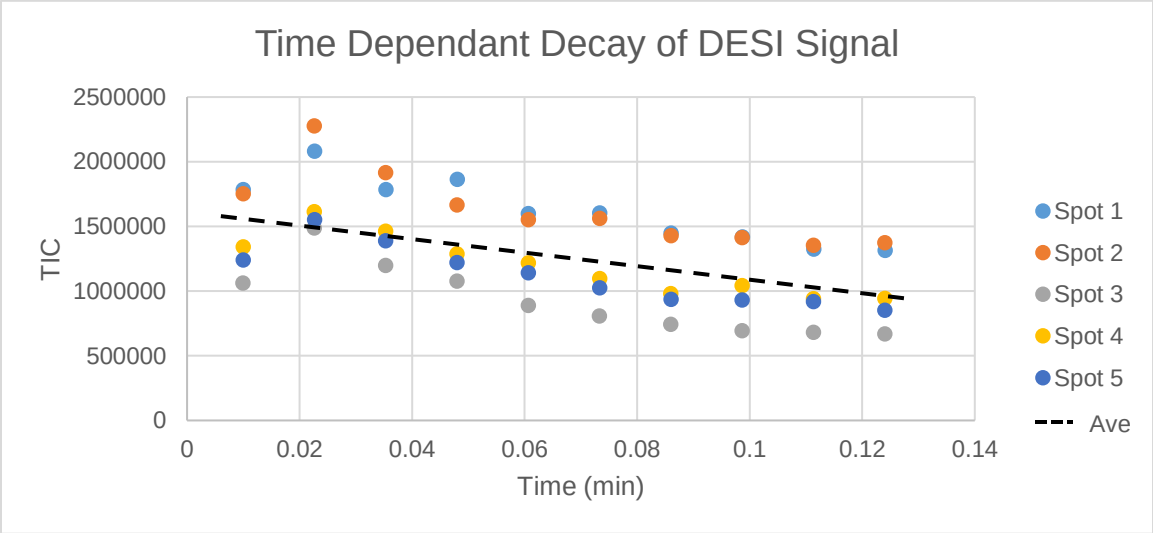

Figure B.1. Time-dependent decay of DESI signal for analysis of five representative spots for 6 seconds (0.10 min) each, without FAIMS sweep, and an average trend line for the total loss in ion intensity throughout the scan.

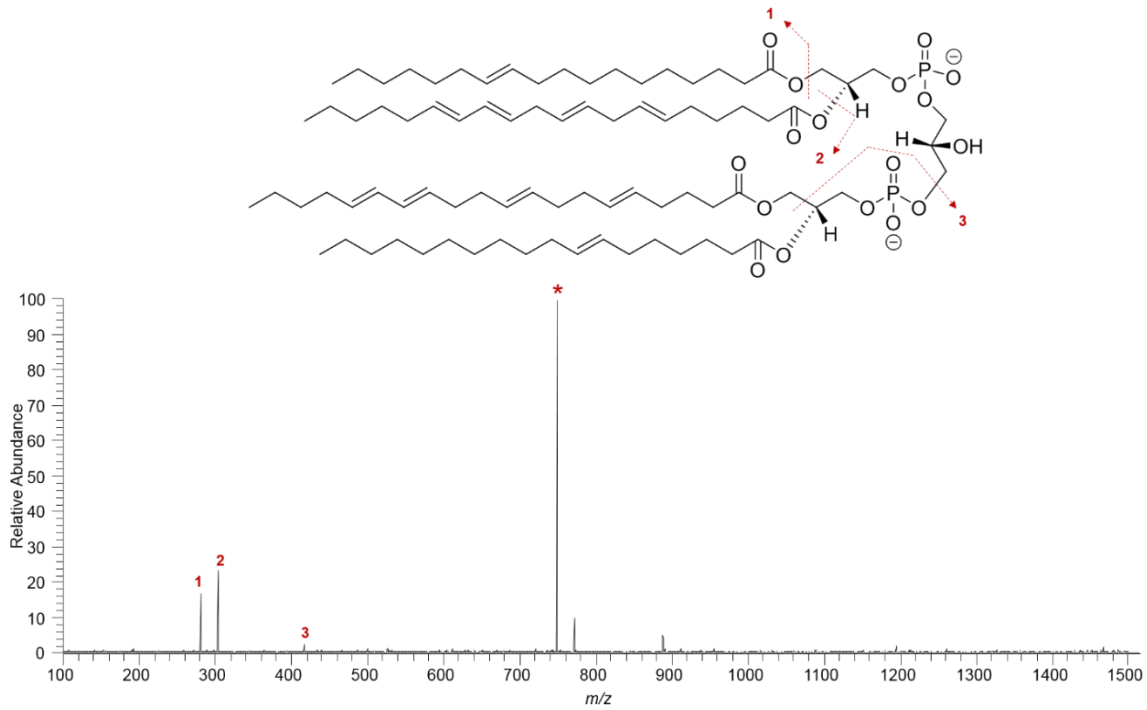

Figure B.2. MSMS of *m/z* 749.495, identified at CL (20:4/20:4/20:4/18:1)

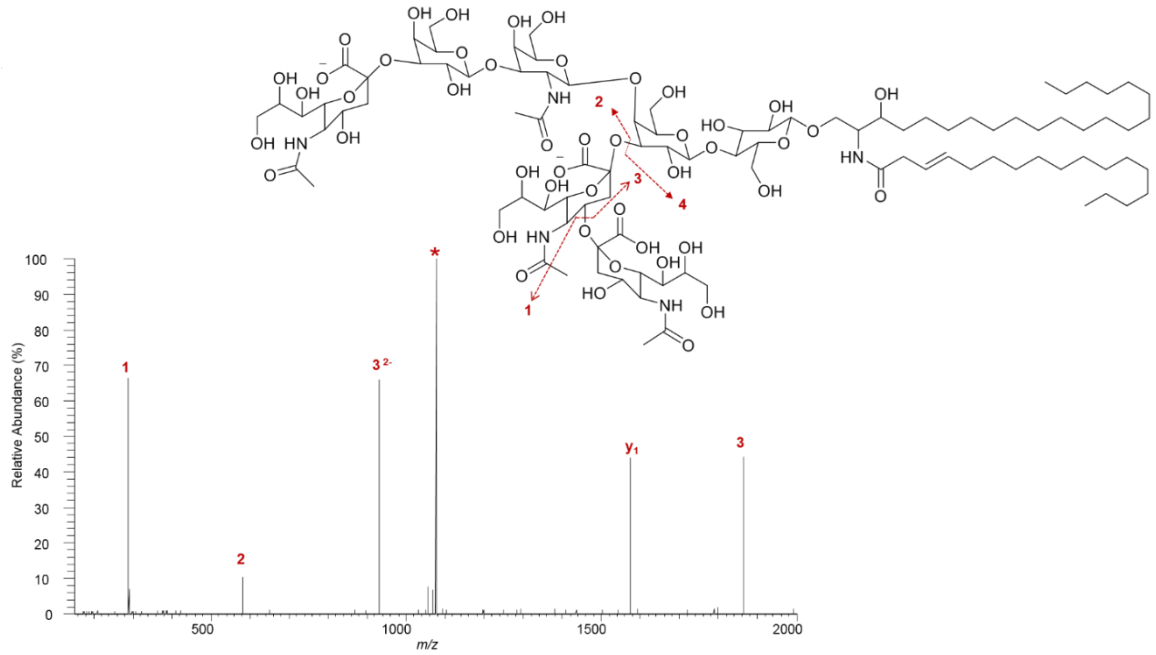

Figure B.3. MS/MS of *m/z* 1077.043, identified at GT1 d38:1 ganglioside

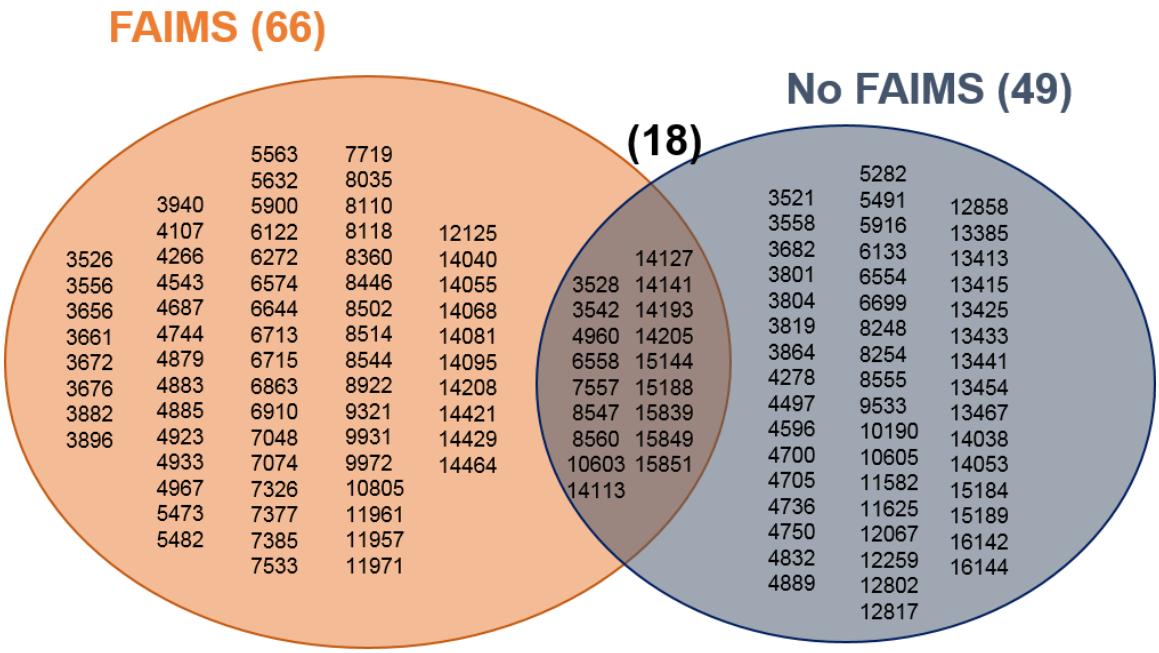

Figure B.4. Molecular weights of all protein, proteoforms, and protein fragment species detected during LMJ-SSP-MS and LMJ-SSP-FAIMS-MS profiling experiments of a rat brain tissue sections.

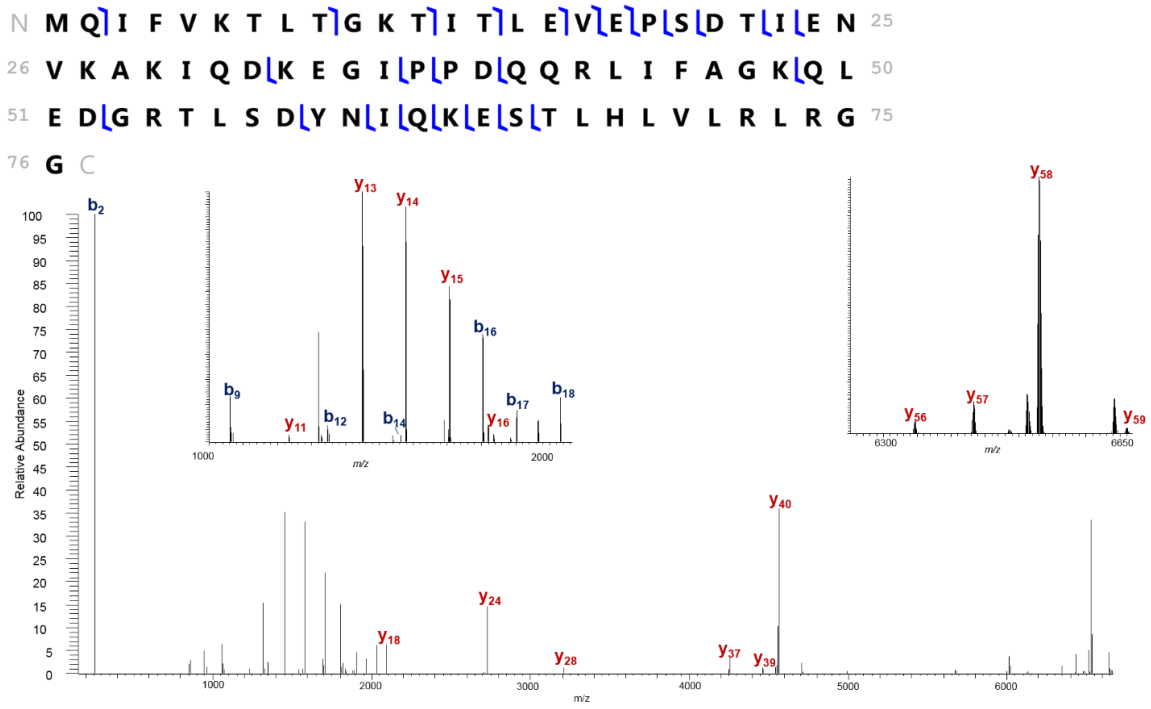

PCS	560.77
P-Score	4.1E-51
Fragments Explained	51%
Residue Cleavages	32%

Figure B.5. MS/MS of ion cluster at *m/z* 857.46 from a rat brain tissue section, identified at ubiquitin.

The sequence coverage map of the fragments compared to the sequence of rat ubiquitin is shown, as well as the ProSight Lite scores.

Table B.1. Matching fragment ions identified from MS/MS of ion m/z 857.46 compared with the sequence of rat ubiquitin.

Name	Ion Type	Theoretical Mass[a]	Observed Mass[a]	Mass Difference (Da)	Mass Difference (ppm)
B2	B	259.0991	259.0979	-0.0012	-4.50
B9	B	1061.5943	1061.5898	-0.0045	-4.28
B12	B	1347.7584	1347.7525	-0.0060	-4.43
B14	B	1561.8902	1561.8900	-0.0002	-0.11
B16	B	1804.0168	1804.0102	-0.0066	-3.68
B17	B	1903.0852	1903.0795	-0.0058	-3.02
B18	B	2032.1278	2032.1188	-0.0090	-4.43
Y11	Y	1233.7669	1233.7614	-0.0055	-4.46
Y12	Y	1320.7990	1320.7936	-0.0054	-4.05
Y13	Y	1449.8416	1449.8362	-0.0054	-3.71
Y14	Y	1577.9365	1577.9304	-0.0062	-3.90
Y15	Y	1705.9951	1705.9890	-0.0061	-3.58
Y16	Y	1819.0792	1819.0727	-0.0065	-3.56
Y18	Y	2096.1854	2096.1764	-0.0090	-4.28
Y24	Y	2725.4987	2725.4858	-0.0129	-4.74
Y28	Y	3210.7109	3210.6945	-0.0164	-5.09
Y37	Y	4252.3192	4252.3007	-0.0185	-4.35
Y39	Y	4464.3989	4464.3809	-0.0180	-4.02
Y40	Y	4561.4517	4561.4344	-0.0173	-3.78
Y44	Y	4988.6947	4988.6763	-0.0185	-3.70
Y53	Y	6014.2453	6014.2261	-0.0192	-3.18
Y54	Y	6127.3293	6127.3034	-0.0259	-4.23
Y56	Y	6343.4040	6343.3750	-0.0290	-4.56
Y57	Y	6430.4360	6430.3867	-0.0493	-7.67
Y58	Y	6527.4887	6527.4705	-0.0183	-2.79
Y59	Y	6656.5313	6656.5028	-0.0286	-4.29

[a] Calculated based on monoisotopic masses

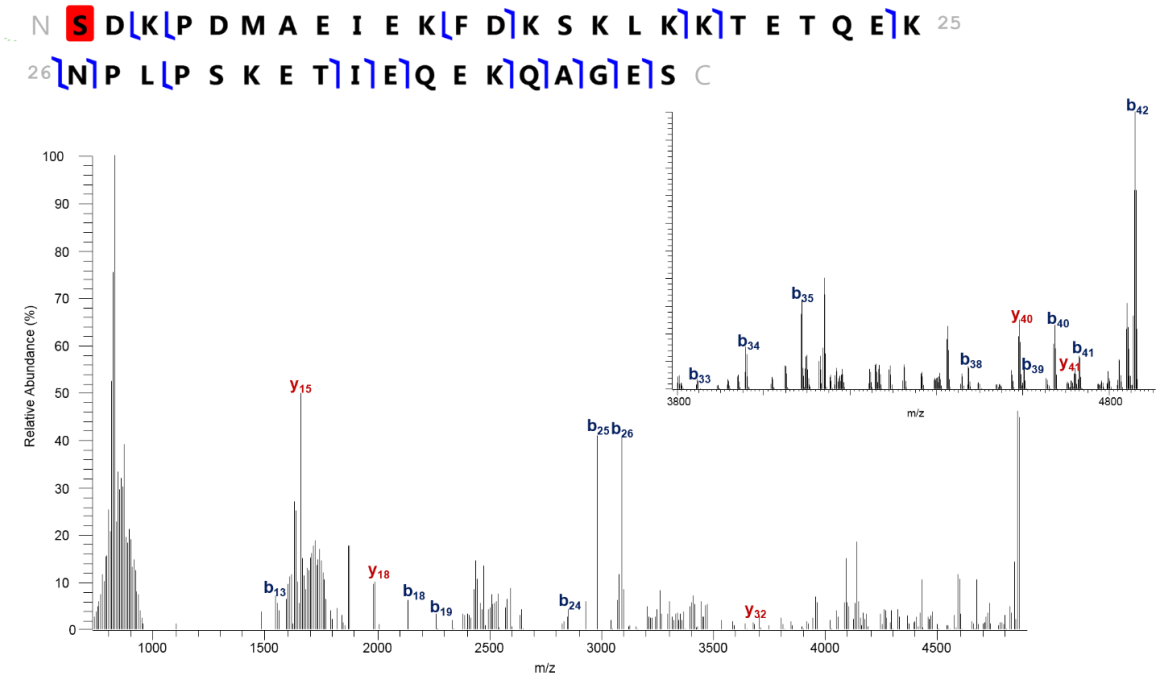

PCS	110.46
P-score	8.6E-15
Fragments Explained	2%
Residue Cleavages	43%

Figure B.6. MS/MS of ion cluster at *m/z* 828.06 from a rat brain tissue section, identified as thymosin β-4.

The sequence coverage map of the fragments compared to the sequence of rat thymosin β-4 is shown, as well as the ProSight Lite scores. The red highlight indicates an acylation.

Table B.2. Matching fragment ions identified from MS/MS of ion *m/z* 828.09 compared with the sequence of rat thymosin β-4.

Name	Ion Type	Theoretical Mass[a]	Observed Mass[a]	Mass Difference (Da)	Mass Difference (ppm)
B13	B	1547.6813	1547.6796	-0.0017	-1.13
B18	B	2132.0823	2132.0792	-0.0031	-1.45
B19	B	2260.1773	2260.1721	-0.0052	-2.28
B24	B	2848.4164	2848.4143	-0.0021	-0.72
B25	B	2976.5114	2976.5076	-0.0037	-1.24
B26	B	3090.5543	3090.5502	-0.0041	-1.33
B33	B	3842.9611	3842.9526	-0.0085	-2.21
B34	B	3956.0452	3956.0396	-0.0055	-1.40
B35	B	4085.0878	4085.0722	-0.0156	-3.82
B38	B	4470.2839	4470.2757	-0.0082	-1.83
B39	B	4598.3425	4598.3371	-0.0053	-1.16
B40	B	4669.3796	4669.3695	-0.0101	-2.16
B41	B	4726.4011	4726.3878	-0.0133	-2.81
B42	B	4855.4436	4855.4401	-0.0036	-0.74
Y15	Y	1659.7951	1659.7926	-0.0025	-1.51
Y18	Y	1983.9749	1983.9731	-0.0018	-0.90
Y32	Y	3674.9002	3674.8946	-0.0057	-1.54
Y40	Y	4588.3217	4588.3140	-0.0077	-1.68
Y41	Y	4716.4167	4716.4102	-0.0065	-1.37

[a] Calculated based on monoisotopic masses

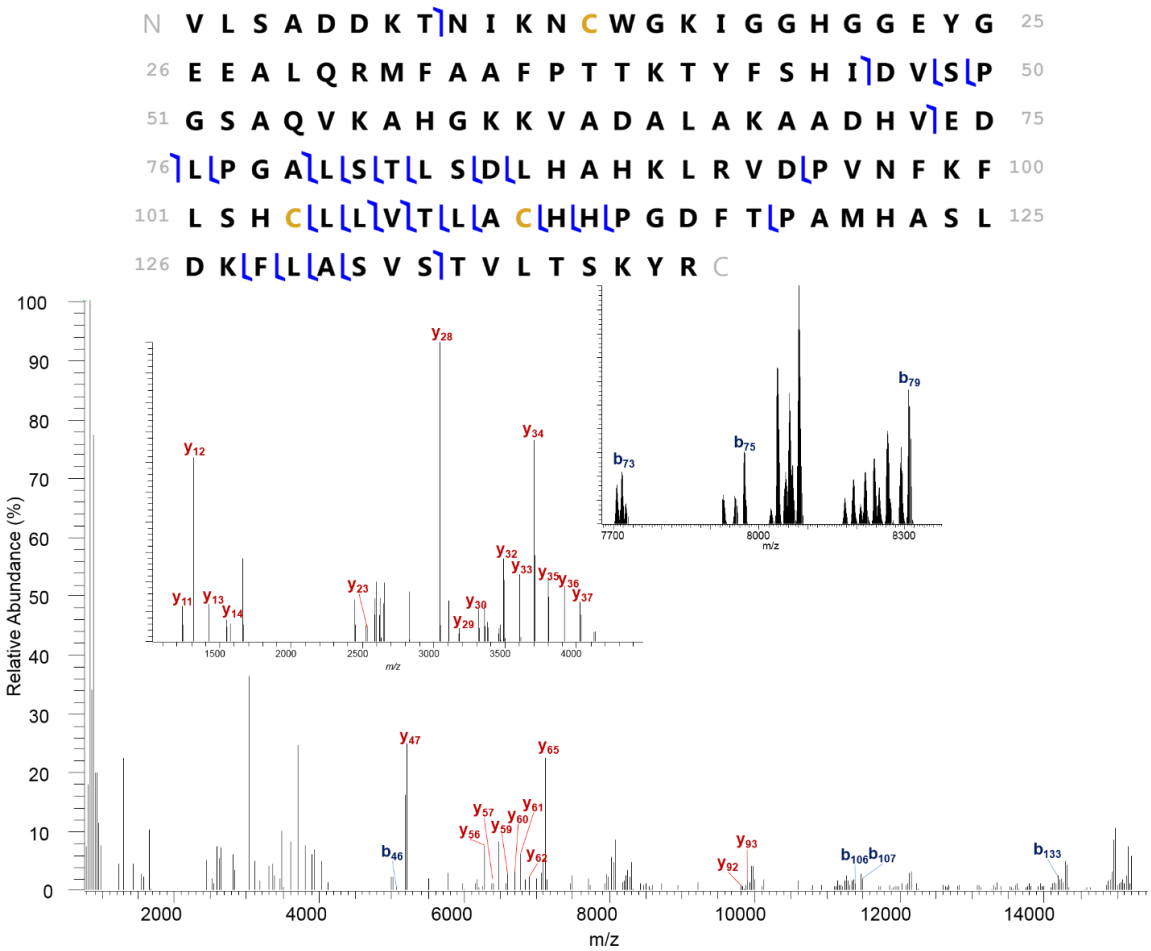

PCS	157.05
P-score	8.2E-19
Fragments Explained	5%
Residue Cleavages	21%

Figure B.7. MS/MS of ion cluster at *m/z* 845.27 from a rat brain tissue section, identified as hemoglobin-α subunit.

The sequence coverage map of the fragments compared to the sequence of rat hemoglobin-α subunit is shown, as well as the ProSight Lite scores.

Table B.3. Matching fragment ions identified from MS/MS of ion *m/z* 845.27 compared with the sequence of rat hemoglobin-α subunit.

Name	Ion Type	Theoretical Mass[a]	Observed Mass[a]	Mass Difference (Da)	Mass Difference (ppm)
B8	B	829.4181	829.4205	0.0024	2.86
B46	B	5069.4592	5069.449	-0.0099	-1.94
B73	B	7720.8735	7720.8734	-5.9E-05	-0.01
B75	B	7964.9430	7964.9293	-0.014	-1.71
B79	B	8303.1384	8303.1228	-0.015	-1.87
B106	B	11387.8078	11387.7304	-0.077	-6.79
B106	B	11387.8078	11387.7884	-0.019	-1.71
B107	B	11486.8763	11486.8228	-0.053	-4.65
B107	B	11486.8763	11486.8471	-0.029	-2.53
B133	B	14221.1758	14221.0836	-0.092	-6.48
Y11	Y	1239.6823	1239.6800	-0.0022	-1.81
Y12	Y	1310.7194	1310.7172	-0.0023	-1.71
Y13	Y	1423.8045	1423.8012	-0.0023	-1.60
Y14	Y	1570.8719	1570.8706	-0.0013	-0.82
Y23	Y	2521.3362	2521.3314	-0.0048	-1.91
Y28	Y	3038.5535	3038.5492	-0.0043	-1.41
Y29	Y	3175.6124	3175.6062	-0.0062	-1.96
Y30	Y	3312.6713	3312.6636	-0.0077	-2.32
Y32	Y	3486.7176	3486.7128	-0.0048	-1.36
Y33	Y	3599.8017	3599.8019	0.00025	0.06
Y34	Y	3700.8494	3700.8443	-0.0050	-1.36
Y35	Y	3799.9178	3799.9160	-0.0018	-0.47
Y36	Y	3913.0018	3912.9958	-0.0060	-1.53
Y37	Y	4026.0859	4026.0804	-0.0055	-1.37
Y47	Y	5198.6660	5198.6481	-0.0178	-3.42
Y56	Y	6268.2804	6268.2624	-0.0180	-2.87
Y57	Y	6383.3074	6383.2929	-0.0144	-2.26
Y59	Y	6583.4235	6583.3645	-0.0590	-8.95
Y59	Y	6583.4234	6583.3673	-0.0561	-8.52
Y60	Y	6684.4711	6684.4460	-0.0251	-3.75
Y61	Y	6771.5032	6771.4669	-0.0363	-5.36
Y62	Y	6884.5872	6884.5709	-0.0164	-2.37
Y65	Y	7109.6986	7109.6811	-0.0175	-2.45
Y92	Y	9817.1390	9817.1061	-0.0329	-3.35
Y93	Y	9904.1711	9904.1246	-0.0465	-4.69

[a] Calculated based on monoisotopic masses

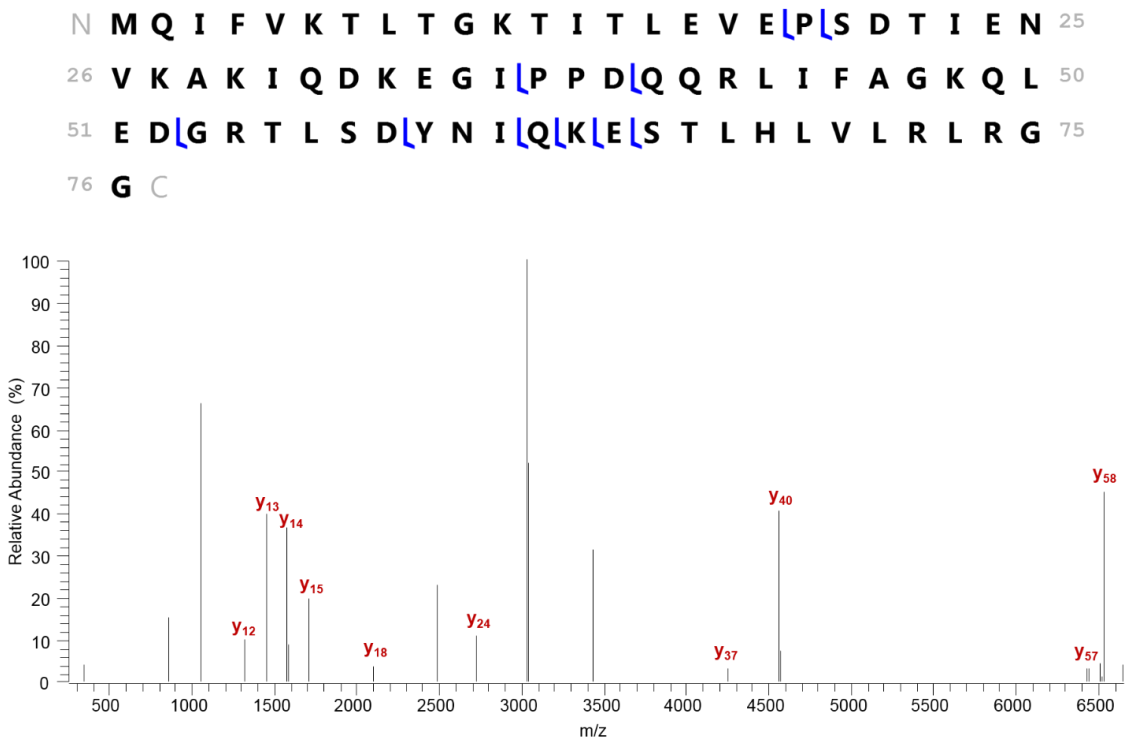

PCS	177.18
P-score	1.6E-20
Fragments Explained	50%
Residue Cleavages	13%

Figure B.8. MS/MS of ion cluster at *m/z* 857.96 from an ovarian tumor tissue section, identified at ubiquitin.

The sequence coverage map of the fragments compared to the sequence of human ubiquitin is shown, as well as the ProSight Lite scores.

Table B.4. Matchi.ng fragment ions identified from MS/MS of ion m/z 952.52 compared with the sequence of rat ubiquitin

Name	Ion Type	Theoretical Mass[a]	Observed Mass	Mass Difference (Da)	Mass Difference (ppm)
Y12	Y	1320.7990	1320.7944	-0.0046	-3.48
Y13	Y	1449.8416	1449.8371	-0.0045	-3.08
Y14	Y	1577.9365	1577.9314	-0.0051	-3.22
Y15	Y	1705.9951	1705.9895	-0.0056	-3.30
Y18	Y	2096.1854	2096.1789	-0.0065	-3.12
Y24	Y	2725.4987	2725.4897	-0.0090	-3.31
Y37	Y	4252.3192	4252.3037	-0.0155	-3.63
Y40	Y	4561.4517	4561.4315	-0.0202	-4.42
Y57	Y	6430.4360	6430.4162	-0.0197	-3.068
Y58	Y	6527.4887	6527.4627	-0.0260	-3.99

[a] Calculated based on monoisotopic masses

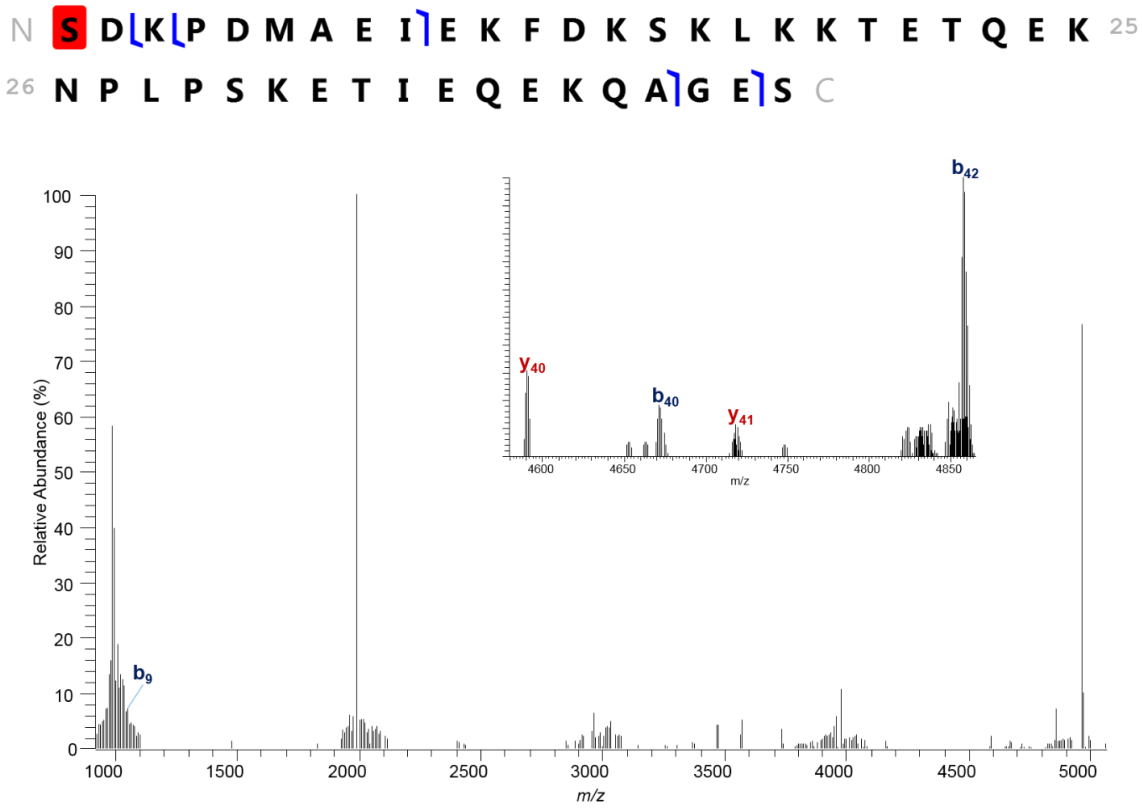

PCS	0.20
P-score	0.054
Fragments Explained	0%
Residue Cleavages	12%

Figure B.9. MS/MS of ion cluster at *m/z* 933.50 from an ovarian tumor tissue section, identified as thymosin β-4.

The sequence coverage map of the fragments compared to the sequence of human thymosin β-4 is shown, as well as the ProSight Lite scores. The red highlight indicates an acylation.

Table B.5. Matching fragment ions identified from MS/MS of ion *m/z* 933.50 compared with the sequence of human thymosin β-4.

Name	Ion Type	Theoretical Mass[a]	Observed Mass[a]	Mass Difference (Da)	Mass Difference (ppm)
B9	B	1028.4484	1028.4410	-0.0074	-7.21
B40	B	4669.3796	4669.3607	-0.0188	-4.03
B42	B	4855.4436	4855.4379	-0.0057	-1.17
Y40	Y	4588.3217	4588.3141	-0.0076	-1.65
Y41	Y	4716.4167	4716.4187	0.0020	0.42

[a] Calculated based on monoisotopic masses

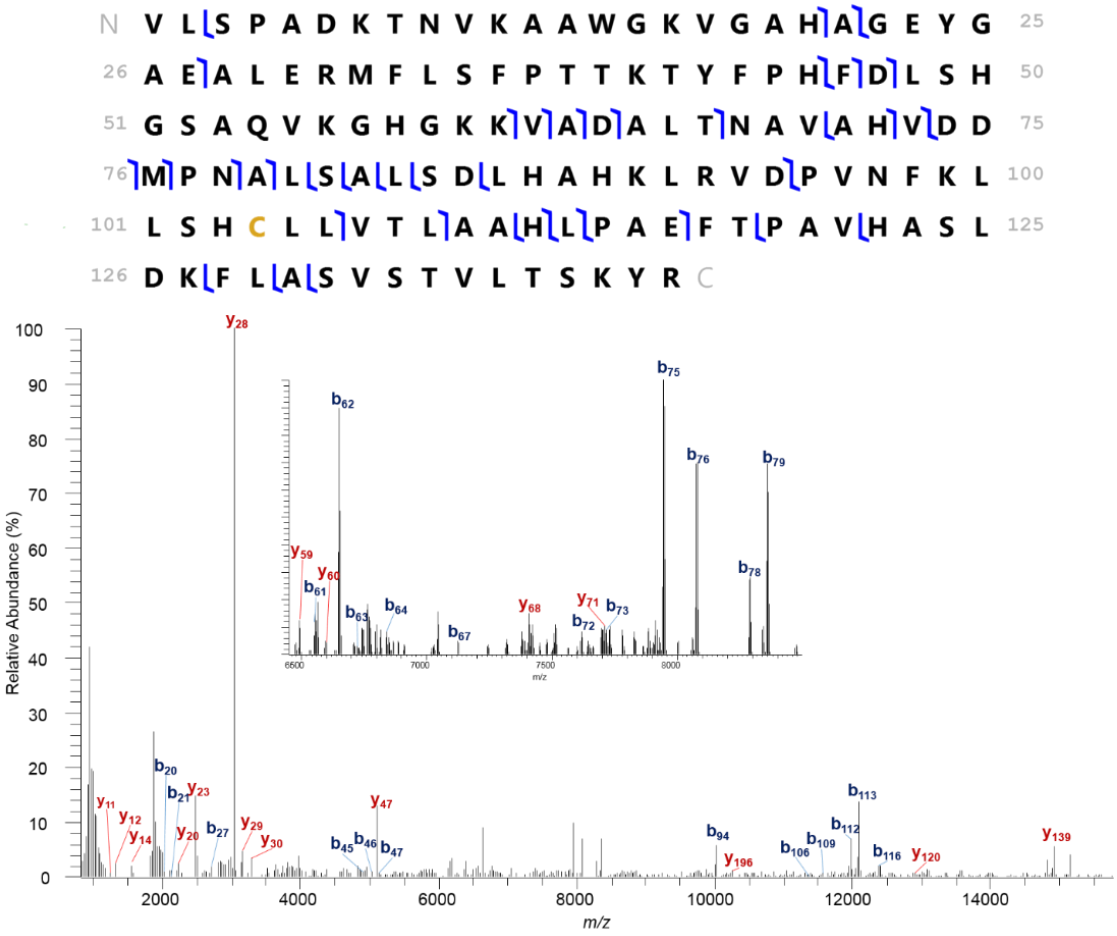

PCS	57.39
P-score	6.5E-10
Fragments Explained	2%
Residue Cleavages	26%

Figure B.10. MS/MS of ion cluster at *m/z* 946.31 from a rat brain tissue section, identified as hemoglobin-α subunit.

The sequence coverage map of the fragments compared to the sequence of rat hemoglobin-α subunit is shown, as well as the ProSight Lite scores.

Table B.6. Matching fragment ions identified from MS/MS of ion *m/z* 946.31 compared with the sequence of human hemoglobin-α subunit.

Name	Ion Type	Theoretical Mass	Observed Mass	Mass Difference (Da)	Mass Difference (ppm)
B20	B	2030.1061	2030.1035	-0.0026	-1.264
B21	B	2101.1432	2101.1404	-0.0028	-1.34
B27	B	2707.3717	2707.3642	-0.0075	-2.78
B45	B	4874.4642	4874.4595	-0.0047	-0.96
B46	B	5021.5326	5021.5280	-0.0046	-0.92
B47	B	5136.5595	5136.5548	-0.0047	-0.91
B61	B	6551.3388	6551.3535	0.0147	2.24
B62	B	6650.4072	6650.3999	-0.0073	-1.10
B63	B	6721.4444	6721.4323	-0.0120	-1.78
B64	B	6836.4713	6836.4537	-0.0176	-2.57
B67	B	7121.6401	7121.5968	-0.0433	-6.08
B72	B	7613.8846	7613.8668	-0.0178	-2.34
B73	B	7712.9530	7712.9369	-0.0161	-2.09
B75	B	7943.0069	7942.9961	-0.0108	-1.35
B76	B	8074.0474	8074.0317	-0.0157	-1.94
B78	B	8285.1431	8285.1516	0.0086	1.03
B79	B	8356.1802	8356.1595	-0.0207	-2.47
B94	B	10012.0909	10012.0861	-0.0048	-0.48
B106	B	11376.8547	11376.8189	-0.0359	-3.15
B109	B	11690.0549	11690.0228	-0.0321	-2.74
B112	B	11969.1880	11969.1629	-0.0251	-2.09
B113	B	12082.2721	12082.2634	-0.0087	-0.72
B116	B	12379.4045	12379.4518	0.0473	3.82
Y11	Y	1239.68230	1239.6811	-0.0011	-0.92
Y12	Y	1310.71941	1310.7178	-0.0016	-1.19
Y14	Y	1570.87188	1570.8688	-0.0031	-1.97
Y20	Y	2222.20589	2222.2096	0.0037	1.67
Y23	Y	2489.36417	2489.3615	-0.0026	-1.05
Y28	Y	3034.61272	3034.6095	-0.0032	-1.04
Y29	Y	3147.6968	3147.6990	0.0022	0.69
Y30	Y	3284.7557	3284.7497	-0.0059	-1.81
Y47	Y	5104.7939	5104.7913	-0.0026	-0.50
Y56	Y	6174.4084	6174.4043	-0.0041	-0.66

Table B.6. (cont.)

Y58	Y	6376.4673	6376.4641	-0.0032	-0.50
Y59	Y	6489.5514	6489.5603	0.0089	1.38
Y60	Y	6560.5885	6560.5929	0.0044	0.67
Y61	Y	6647.6205	6647.6159	-0.0046	-0.70
Y68	Y	7403.9318	7403.9260	-0.0058	-0.78
Y71	Y	7711.0962	7711.1057	0.0095	1.23
Y96	Y	10242.4206	10242.4138	-0.0068	-0.66
Y120	Y	13015.7416	13015.7447	0.0031	0.24
Y139	Y	14904.7323	14904.7339	0.0016	0.11

[a] Calculated based on monoisotopic masses

APPENDIX C: SUPPORTING MATERIAL TO ACCOMPANY CHAPTER 4

Table C.1. Structures, molecular weights, and synthetic reagents used to synthesize all dicationic compounds used in this study

Molecule	Molecular Weight (g/mol)	Synthetic reagent A	Synthetic reagent B	Structure
$C_6(mpy)_2$-Br	254.46	1,6-dibromohexane	1-methylpyrrolidine	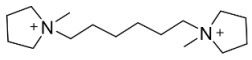
$C_8(mpy)_2$-Br	282.52	1,8-dibromooctane	1-methylpyrrolidine	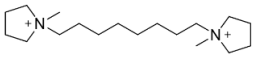
$C_6(epy)_2$-Br	282.52	1,6-dibromohexane	1-ethylpyrrolidine	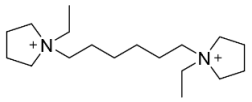
$C_8(epy)_2$-Br	310.57	1,8-dibromooctane	1-ethylpyrrolidine	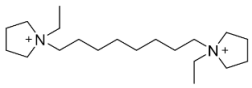

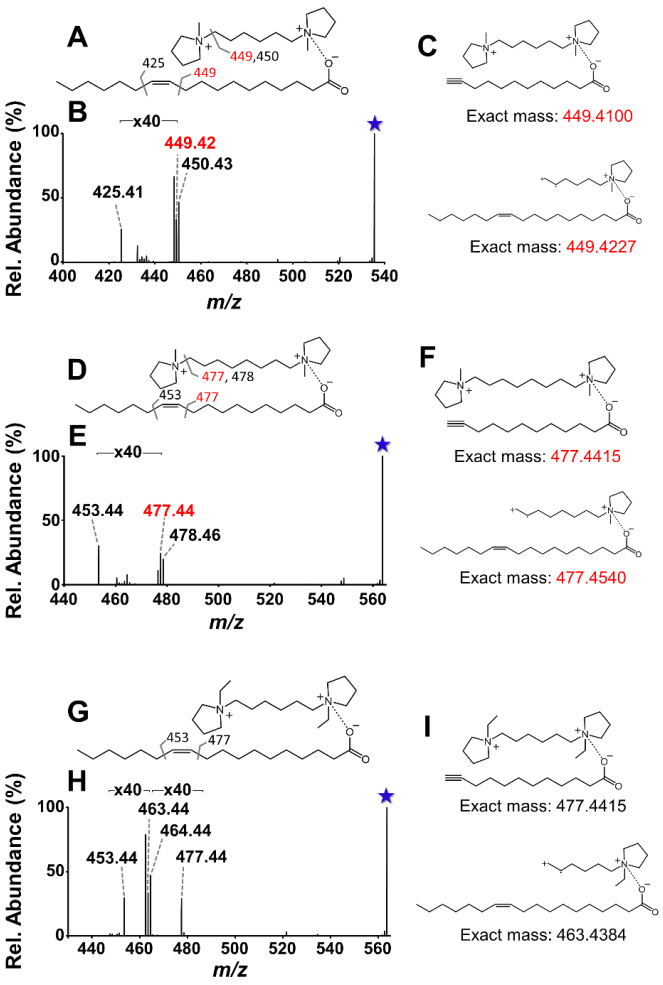

Figure C.1. 193 nm UVPD (20 pulses, 4 mJ) mass spectra for FA 18:1(11Z) complexed to various dicationic compounds. Dications were selected to minimize the presence of isobaric UVPD fragments from the dicationic and FA structures.

(A) Structure of 18:1(11Z) complexed to 1,6-methyl dication (*m/z* 535.52) with labelled fragments from corresponding (B) UVPD spectrum. (C) Isobaric fragment structures confounding interpretation are shown. (D) Structure of 18:1(11Z) complexed to 1,8-methyl dication (*m/z* 563.55) with labelled fragments from corresponding (E) UVPD spectrum. (F) Isobaric fragment structures confounding interpretation are shown. (G) Structure of 18:1(11Z) complexed to 1,6-ethyl (*m/z* 563.55) dication with labelled fragments from corresponding (H) UVPD spectrum. (I) Incorporation of an ethyl group on the quaternary amine results in separation of the confounding DC and FA fragment products in *m/z* space. Isobar signals and masses are highlighted in red font. Selected precursor ions are designated with a star.

Table C.2. Patient and sample demographics for breast cancer biopsies

Sample	Patient Age	Patient Race	Gender	Histological subtype	Metastatic	ER	PR
1121412	41	White	Female	IDC	Yes	+	+
1162617	53	White	Female	IDC	No	+	+
1181239	57	Asian	Female	IDC	Yes	-	-
1170374F	67	White	Male	IDC	Yes	+	+
A144g	58	White	Female	DCIS	No	N/A	N/A
1085255F	50	Asian	Female	IDC	No	+	+
A054a	58	Black	Female	DCIS	No	N/A	N/A
A060h	68	White	Female	IDC	No	+	+
A074cc	42	White	Female	DCIS	No	N/A	N/A
A121g	36	Black	Female	DCIS	Yes	+	+
A177p	60	White	Female	IDC	Yes	-	-
A187a	58	White	Female	DCIS	No	N/A	N/A
A479c	69	White	Female	DCIS	No	+	-
ED76628	63	Asian	Female	IDC	Yes	-	+
ED77376	70	White	Female	IDC	No	+	+
ED79797	72	White	Female	IDC	Yes	+	+
M411101A18	55	Black	Female	IDC	No	-	-
M1170681	56	White	Female	IDC	Yes	+	+

APPENDIX D: SUPPORTING MATERIAL TO ACCOMPANY CHAPTER 5

Table D.1. Information regarding the number/types of samples contributed by patient.

Patient number	Eutopic endometrial samples contributed	Ectopic endometrial samples contributed	Types of endometriosis lesions obtained
3	--	1	Peritoneum
4	--	1	Serosal
5	--	1	Serosal
12	--	1	Peritoneum
13	--	1	Peritoneum
16	--	2	Peritoneum
			Adventital us ligament
17	--	3	Peritoneum
			Peritoneum
			Serosal
19	2	--	--
21	--	3	Adventital us ligament
			Adventital us ligament
			Peritoneum
23	1	1	Adventital us ligament
24	1		--
25	1	1	--
27	--	3	Peritoneum and Ligamentous
			Peritoneum and Ligamentous
			Adventital us ligament
28	1	--	--
30	1	4	Serosal
			Serosal
			Adventital us ligament
			Peritoneum and Ligamentous
34	1		
36	--	8	Peritoneum
			Peritoneum
			Peritoneum
			Serosal
			Peritoneum
			Peritoneum
			Endometrioma
			Endometrioma

Table D.1. (cont.)

Patient number	Eutopic endometrial samples contributed	Ectopic endometrial samples contributed	Types of endometriosis lesions obtained
38	1	1	Peritoneum
40	--	3	Peritoneum
			Peritoneum
			Peritoneum
41	1	--	--
42	1	2	Peritoneum
			Endometrioma
45	1	3	Peritoneum
			Peritoneum
			Serosal
48	1	--	--
49	1	--	--
50	--	2	Endometrioma
			Peritoneum
51	--	2	Peritoneum
			Peritoneum
52	--	1	Serosal
53	1	--	--
54		3	Serosal
			Peritoneum
			Peritoneum
56	1	2	Serosal
			Peritoneum
59	1	--	--
65	--	3	Serosal
			Cortex
			Cortex
67	--	1	Peritoneum
68	1	--	--
69	--	1	Adventital us ligament
71	--	1	Peritoneum
72	--	1	Serosal
74	--	1	Peritoneum
75	--	1	Serosal
76	--	1	Cortex
77	--	2	Serosal

Table D.1. (cont.)

Patient number	Eutopic endometrial samples contributed	Ectopic endometrial samples contributed	Types of endometriosis lesions obtained
77	--	2	Peritoneum
78	--	1	Serosal
79	1	--	--
82	--	3	Peritoneum
			Adventital us ligament
			Serosal
85	--	2	Adventital us ligament
			Serosal
87	--	1	Peritoneum
88	--	1	Peritoneum
89	--	1	Fallopian tube
93	1	2	Peritoneum
			Adventital us ligament
96	1	--	--
98	1	4	Cortex
			Serosal
			Endometrioma
			Serosal

If patients contributed ectopic endometrial samples, information about the location of excision is provided in the fourth column. Eutopic endometrial samples were all obtain from the uterus.

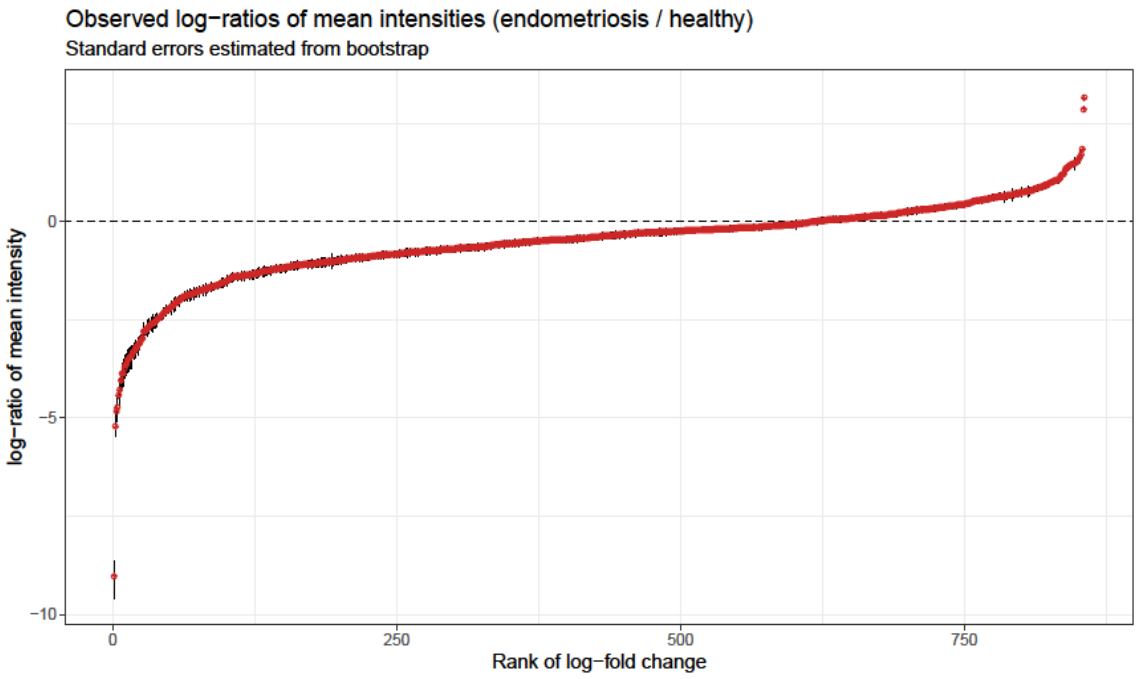

Figure D.1. Visual representation of the nonparametric bootstrapping analysis

The majority of features within our dataset differ significantly between the eutopic and ectopic endometrial tissue using a standard null hypothesis. All features with standard deviations (error bars) falling outside of a 0 value log-fold change will be returned with a p-value of approximately zero when using a traditional null hypothesis.

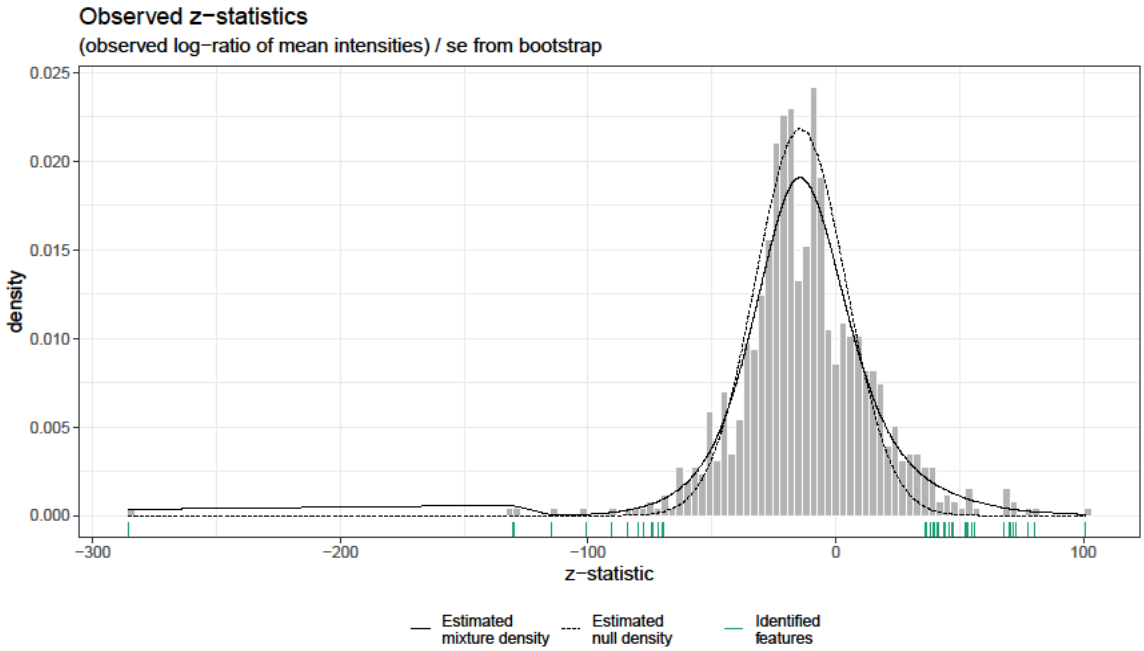

Figure D.2. Histogram of the *z*-values calculated from the observed log-ratio of mean ion intensities of the eutopic and ectopic endometrium tissue, divided by their standard error.

The black lines overlaid on the histogram represent the estimated mixture density and the estimated null density, and selected "interesting" features are signified by green lines below the histogram.

Table D.2. Summary of patient demographics for prospectively collected endometriosis samples.

Race						
African American	Asian	East Indian	Hispanic	White	Other	Unknown
8	1	1	9	53	1	3
Age						
≤20	20-29	30-39	40-49	≥50	Median	Mean
1	11	34	28	2	38	37.8

Note that some patients that contributed an endometriosis sample also contributed a eutopic endometrium sample, and thus the total number of patients (89) is not the sum of patients from Table D.2 and D.3.

Table D.3. Summary of patient demographics for prospectively collected endometrium samples.

Race						
African American	Asian	East Indian	Hispanic	White	Other	Unknown
4	0	0	2	15	1	0
Age						
≤20	20-29	30-39	40-49	≥50	Median	Mean
0	0	16	6	0	37	38.2

Note that some patients that contributed a eutopic endometrium sample also contributed one or more endometriosis samples, and thus the total number of patients (89) is not the sum of patients from Table D.2 and D.3.

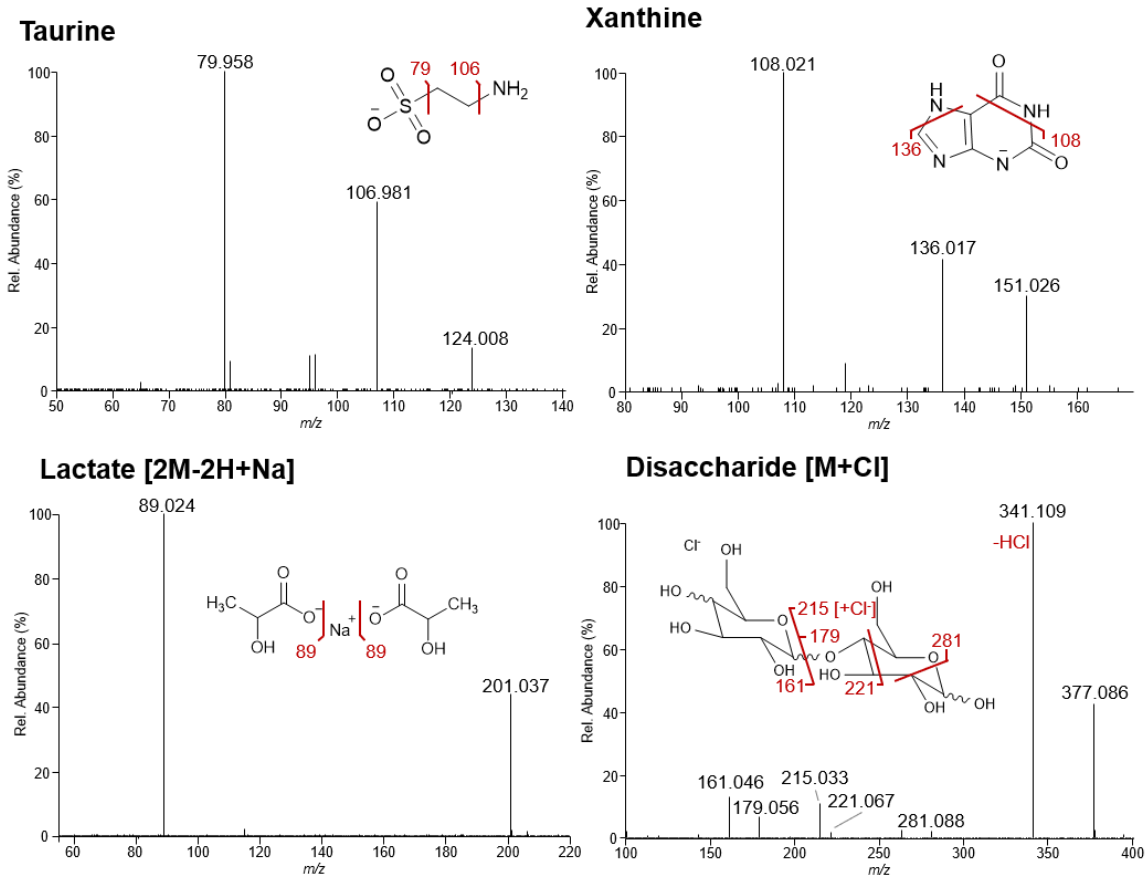

Figure D.3. Example MS/MS data collected to identify metabolite species detected during DESI-MS imaging experiments of endometrium and endometriosis lesions that were later selected as features within either lasso or empirical bootstrap analyses.

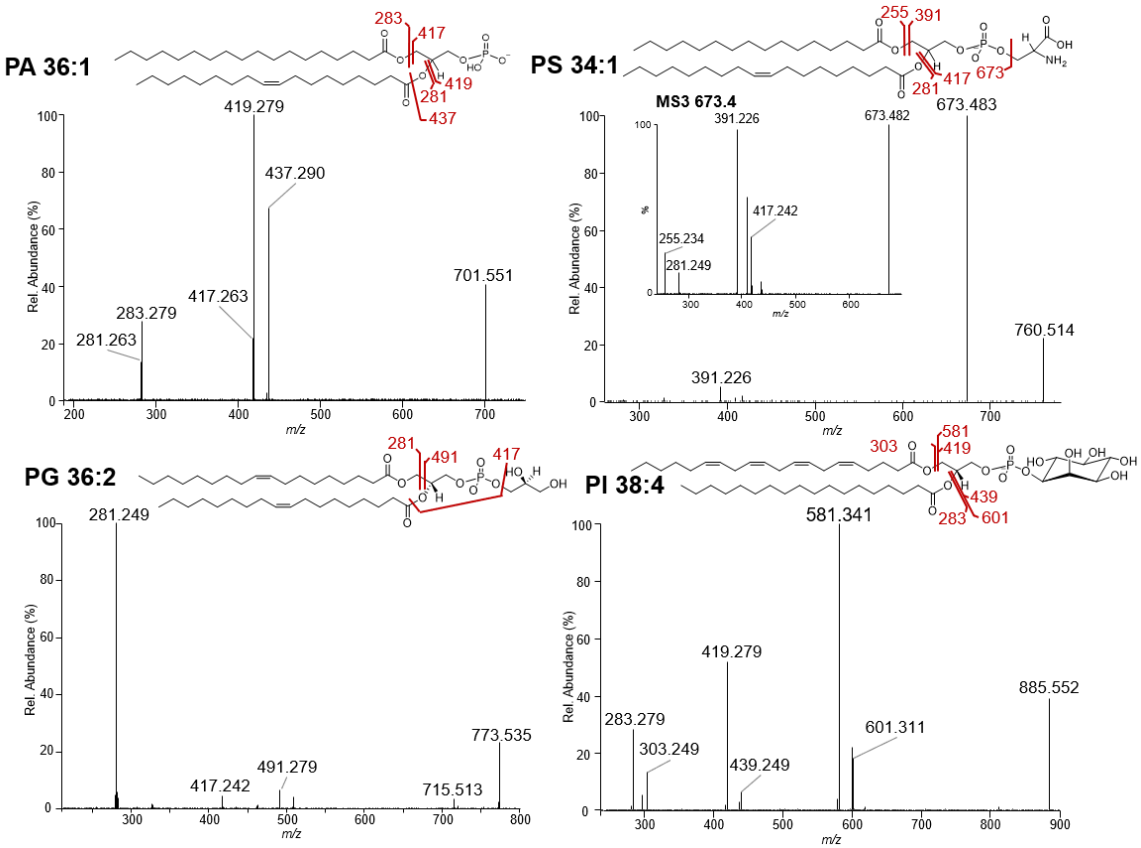

Figure D.4. Example MS/MS data collected to identify glycerophospholipid species detected during DESI-MS imaging experiments of endometrium and endometriosis lesions that were later selected as features within either lasso or empirical bootstrap analyses.

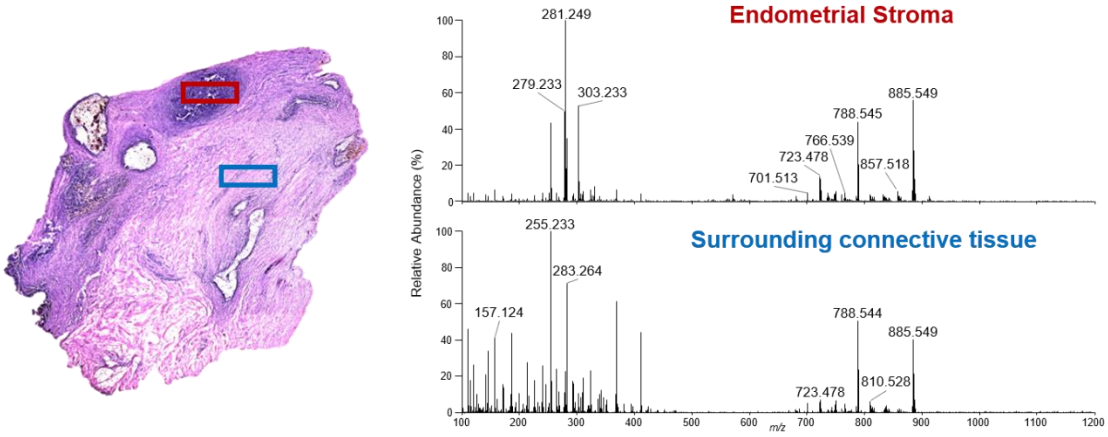

Figure D.5. DESI-MS imaging mass spectra from endometrial stroma region and surrounding connective tissue.

The colored boxes on the optical image (Left) correspond to the endometrial stroma (Red) and the connective tissue (Blue) from which 5 spectra were averaged to display. The relative abundance for the endometrial stroma is about one order of magnitude more intense (NL: 3.76E4) compared to the connective tissue (NL: 4.86E3), hence the lower overall signal intensity exhibited throughout the ion images shown in the manuscript.

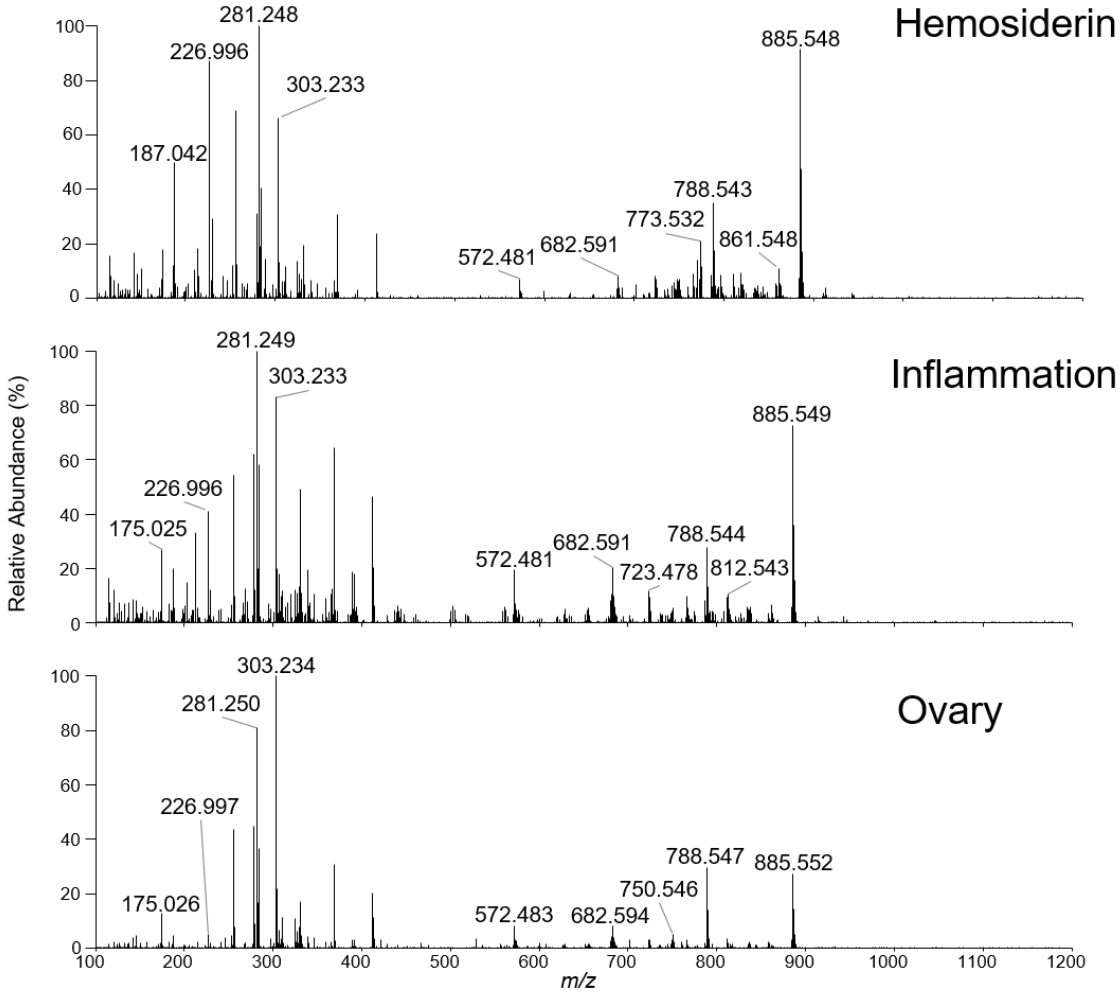

Figure D.6. DESI-MS imaging mass spectra from other regions of tissue involved in this study, including hemosiderin, inflammatory cells, and ovary.

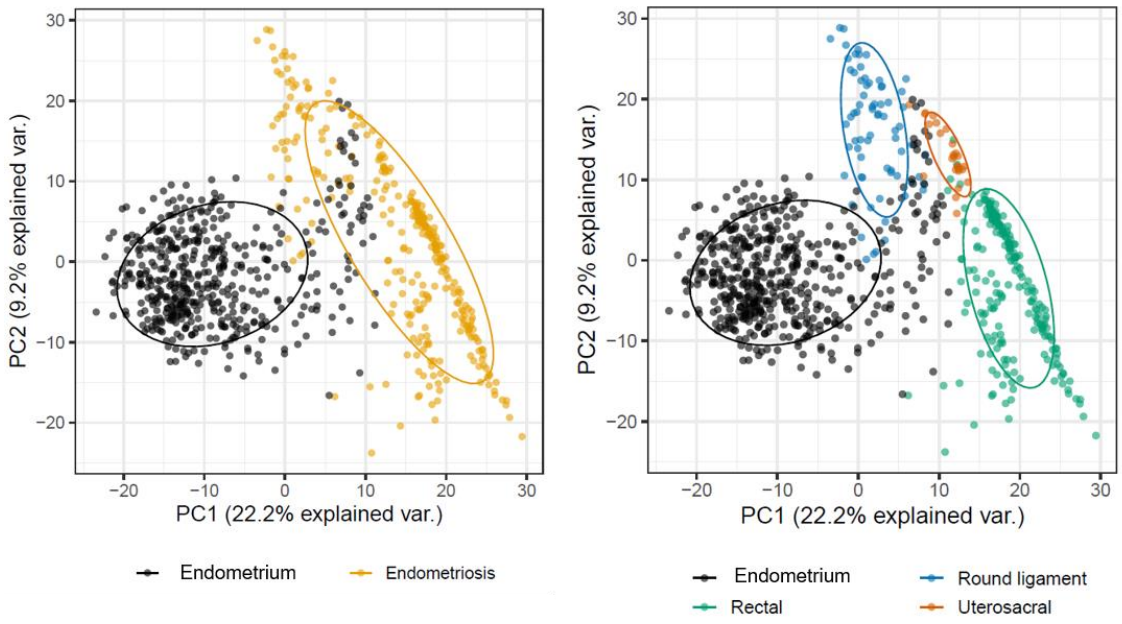

Figure D.7. Intra-patient PCA score plots of eutopic endometrium and three endometriosis tissues collected from round ligament, rectal, uterosacral area of patient #30.

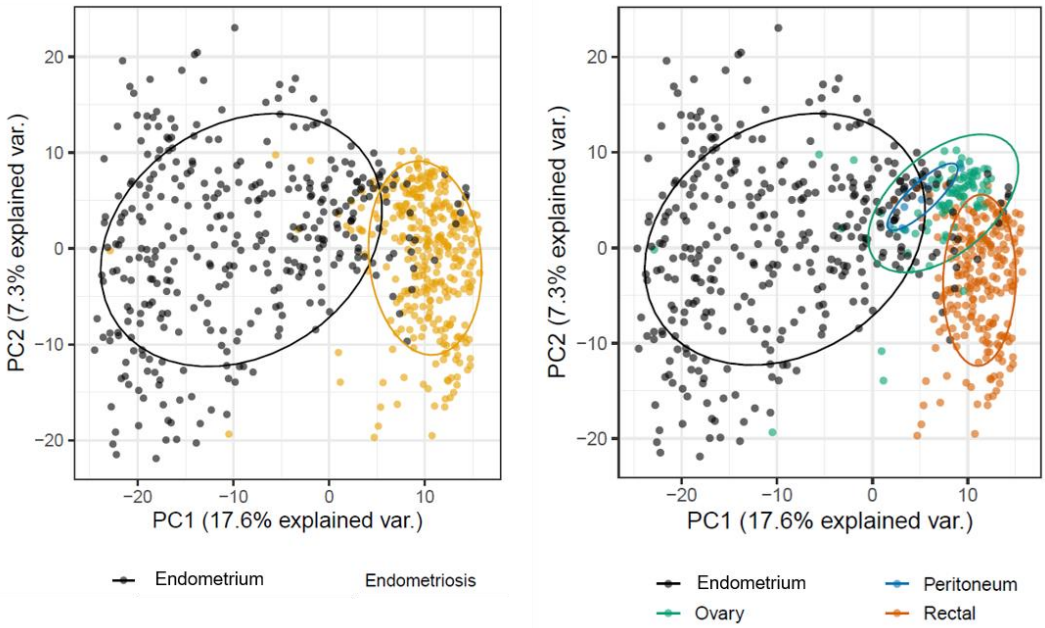

Figure D.8. Intra-patient PCA score plots of eutopic endometrium and three endometriosis tissues collected from round ligament, rectal, uterosacral area of patient #45.

Table D.4 Summary of menstrual cycle day information for samples used for the statistical analysis in this study.

Day 1-10	Day 11-20	Day 21-30	Day >30	Mean	Median	Not Applicable
Eutopic endometrium						
9	4	4	3	16.4	12.5	2
Endometriosis						
18	16	16	2	15.6	16	24

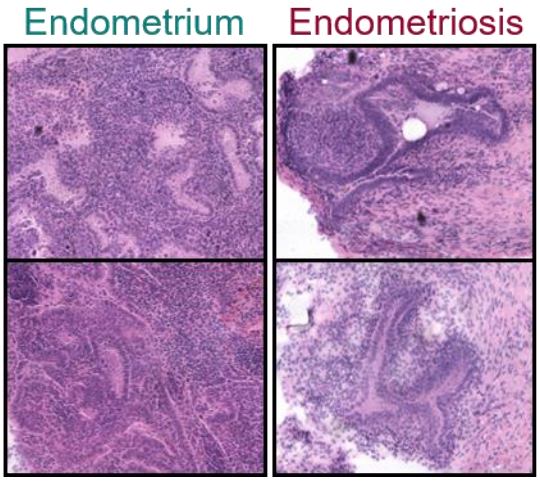

Figure D.9. Comparison of eutopic endometrium (left) and endometriosis (right) glands and stroma, showing their morphological and cellular similarity.

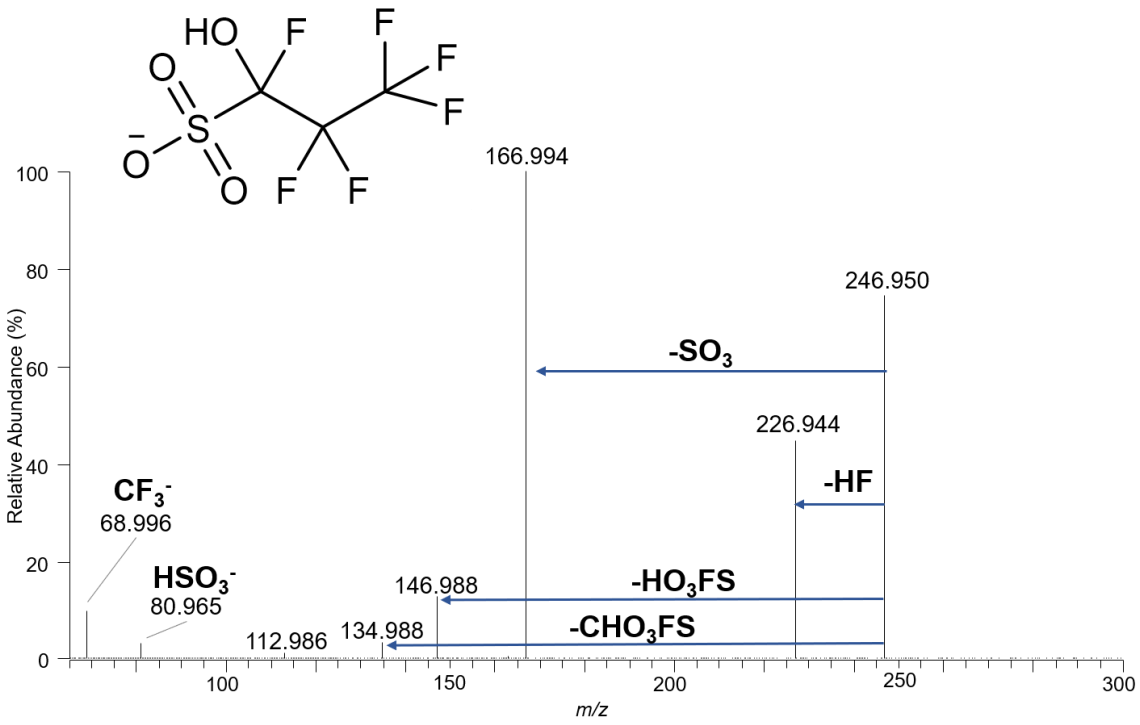

Figure D.10. Tandem MS data of *m/z* 246.951 and proposed neutral loss fragments. Due to the fluorinated nature of this compound, it is most likely a derivatization product of sevoflurane, a common surgical anesthetic.

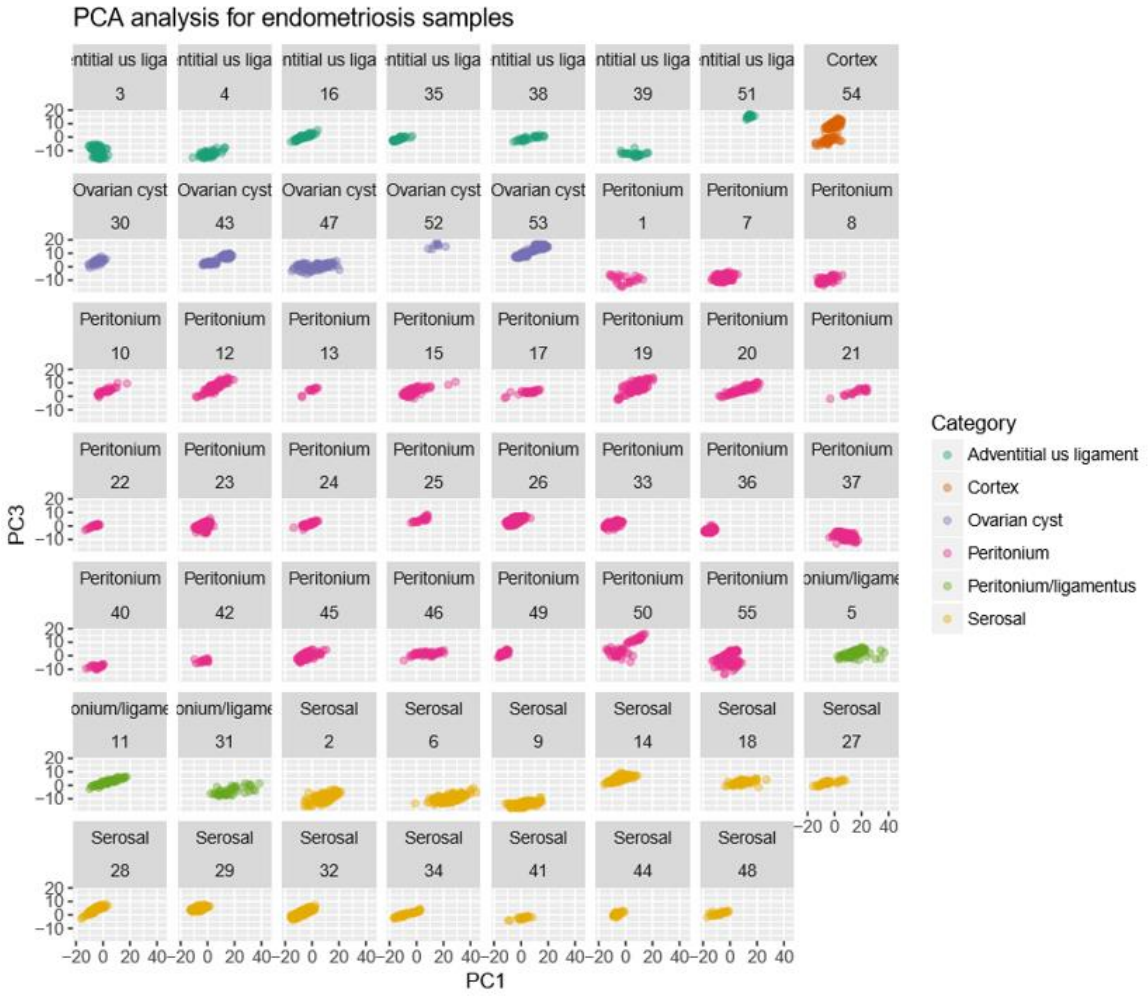

Figure D.11. PCA score plots faceted by sample number and colored by location of excision.

References

(1) Singhal, N.; Kumar, M.; Kanaujia, P. K.; Virdi, J. S. *Frontiers in Microbiology* **2015**, *6*.

(2) Sreekumar, A.; Poisson, L. M.; Rajendiran, T. M.; Khan, A. P.; Cao, Q.; Yu, J.; Laxman, B.; Mehra, R.; Lonigro, R. J.; Li, Y.; Nyati, M. K.; Ahsan, A.; Kalyana-Sundaram, S.; Han, B.; Cao, X.; Byun, J.; Omenn, G. S.; Ghosh, D.; Pennathur, S.; Alexander, D. C., et al. *Nature* **2009**, *457*, 910-914.

(3) Tang, W. H. W.; Wang, Z.; Levison, B. S.; Koeth, R. A.; Britt, E. B.; Fu, X.; Wu, Y.; Hazen, S. L. *N. Engl. J. Med.* **2013**, *368*, 1575-1584.

(4) Kitteringham, N. R.; Jenkins, R. E.; Lane, C. S.; Elliott, V. L.; Park, B. K. *J. Chromatogr. B* **2009**, *877*, 1229-1239.

(5) Qian, W.-J.; Jacobs, J. M.; Liu, T.; Camp, D. G.; Smith, R. D. *Molecular & Cellular Proteomics* **2006**, *5*, 1727-1744.

(6) Prentice, B. M.; Caprioli, R. M. *Postdoc J* **2016**, *4*, 3-13.

(7) Schwamborn, K.; Caprioli, R. M. *Nat. Rev. Cancer* **2010**, *10*, 639-646.

(8) Scott, D. A.; Casadonte, R.; Cardinali, B.; Spruill, L.; Mehta, A. S.; Carli, F.; Simone, N.; Kriegsmann, M.; Del Mastro, L.; Kriegsmann, J.; Drake, R. R. *PROTEOMICS – Clinical Applications* **2019**, *13*, 1800014.

(9) Kang, H. S.; Lee, S. C.; Park, Y. S.; Jeon, Y. E.; Lee, J. H.; Jung, S.-Y.; Park, I. H.; Jang, S. H.; Park, H. M.; Yoo, C. W.; Park, S. H.; Han, S. Y.; Kim, K. P.; Kim, Y. H.; Ro, J.; Kim, H. K. *BMC Cancer* **2011**, *11*, 465.

(10) Rauser, S.; Marquardt, C.; Balluff, B.; Deininger, S. O.; Albers, C.; Belau, E.; Hartmer, R.; Suckau, D.; Specht, K.; Ebert, M. P.; Schmitt, M.; Aubele, M.; Hofler, H.; Walch, A. *J. Proteome Res.* **2010**, *9*, 1854-1863.

(11) Oswald-Richter, K. A.; Beachboard, D. C.; Seeley, E. H.; Abraham, S.; Shepherd, B. E.; Jenkins, C. A.; Culver, D. A.; Caprioli, R. M.; Drake, W. P. *Journal of Clinical Immunology* **2012**, *32*, 1129-1140.

(12) Cassat, J. E.; Moore, J. L.; Wilson, K. J.; Stark, Z.; Prentice, B. M.; Van de Plas, R. V.; Perry, W. J.; Zhang, Y. F.; Virostko, J.; Colvin, D. C.; Rose, K. L.; Judd, A. M.; Reyzer, M. L.; Spraggins, J. M.; Grunenwald, C. M.; Gore, J. C.; Caprioli, R. M.; Skaar, E. P. *Science Translational Medicine* **2018**, *10*, 14.

(13) Niehaus, M.; Soltwisch, J.; Belov, M. E.; Dreisewerd, K. *Nature Methods* **2019**, *16*, 925-931.

(14) Frisz, J. F.; Lou, K.; Klitzing, H. A.; Hanafin, W. P.; Lizunov, V.; Wilson, R. L.; Carpenter, K. J.; Kim, R.; Hutcheon, I. D.; Zimmerberg, J.; Weber, P. K.; Kraft, M. L. *Proceedings of the National Academy of Sciences* **2013**, *110*, E613-E622.

(15) Van de Plas, R.; Yang, J.; Spraggins, J.; Caprioli, R. M. *Nature methods* **2015**, *12*, 366-372.

(16) Laskin, J.; Lanekoff, I. *Anal. Chem.* **2016**, *88*, 52-73.

(17) Fenn, J.; Mann, M.; Meng, C.; Wong, S.; Whitehouse, C. *Science* **1989**, *246*, 64-71.

(18) Takats, Z.; Wiseman, J. M.; Gologan, B.; Cooks, R. G. *Science* **2004**, *306*, 471-473.

(19) Wiseman, J. M.; Ifa, D. R.; Song, Q. Y.; Cooks, R. G. *Angew. Chem. Int. Ed.* **2006**, *45*, 7188-7192.

(20) Eberlin, L. S.; Norton, I.; Dill, A. L.; Golby, A. J.; Ligon, K. L.; Santagata, S.; Cooks, R. G.; Agar, N. Y. *Cancer Research* **2011**, canres.2465.2011.

(21) Eberlin, L. S.; Ferreira, C. R.; Dill, A. L.; Ifa, D. R.; Cheng, L.; Cooks, R. G. *ChemBioChem* **2011**, *12*, 2129-2132.

(22) Porcari, A. M.; Zhang, J.; Garza, K. Y.; Rodrigues-Peres, R. M.; Lin, J. Q.; Young, J. H.; Tibshirani, R.; Nagi, C.; Paiva, G. R.; Carter, S. A.; Sarian, L. O.; Eberlin, M. N.; Eberlin, L. S. *Anal. Chem.* **2018**, *90*, 11324-11332.

(23) Calligaris, D.; Caragacianu, D.; Liu, X. H.; Norton, I.; Thompson, C. J.; Richardson, A. L.; Golshan, M.; Easterling, M. L.; Santagata, S.; Dillon, D. A.; Jolesz, F. A.; Agar, N. Y. R. *Proceedings of the National Academy of Sciences of the United States of America* **2014**, *111*, 15184-15189.

(24) Sans, M.; Gharpure, K. M.; Tibshirani, R.; Zhang, J.; Liang, L.; Liu, J.; Young, J. H.; Dood, R.; Sood, A. K.; Eberlin, L. *Cancer Research* **2017**.

(25) Dória, M. L.; McKenzie, J. S.; Mroz, A.; Phelps, D. L.; Speller, A.; Rosini, F.; Strittmatter, N.; Golf, O.; Veselkov, K.; Brown, R.; Ghaem-Maghami, S.; Takats, Z. *Scientific Reports* **2016**, *6*, 39219.

(26) Eberlin, L. S.; Dill, A. L.; Costa, A. B.; Ifa, D. R.; Cheng, L.; Masterson, T.; Koch, M.; Ratliff, T. L.; Cooks, R. G. *Analytical Chemistry* **2010**, *82*, 3430-3434.

(27) Zhang, J.; Yu, W.; Ryu, S.; Lin, J.; Buentello, G.; Tibshirani, R.; Suliburk, J. W.; Eberlin, L. S. *Cancer Res.* **2016**, *76*, 1-10.

(28) DeHoog, R. J.; Zhang, J.; Alore, E.; Lin, J. Q.; Yu, W.; Woody, S.; Almendariz, C.; Lin, M.; Engelsman, A. F.; Sidhu, S. B.; Tibshirani, R.; Suliburk, J.; Eberlin, L. S. *Proceedings of the National Academy of Sciences* **2019**, *116*, 21401-21408.

(29) Jarmusch, A. K.; Pirro, V.; Baird, Z.; Hattab, E. M.; Cohen-Gadol, A. A.; Cooks, R. G. *Proceedings of the National Academy of Sciences of the United States of America* **2016**, *113*, 1486-1491.

(30) Pirro, V.; Alfaro, C. M.; Jarmusch, A. K.; Hattab, E. M.; Cohen-Gadol, A. A.; Cooks, R. G. *Proceedings of the National Academy of Sciences of the United States of America* **2017**, *114*, 6700-6705.

(31) Bergholt, M. S.; Serio, A.; McKenzie, J. S.; Boyd, A.; Soares, R. F.; Tillner, J.; Chiappini, C.; Wu, V.; Dannhorn, A.; Takats, Z.; Williams, A.; Stevens, M. M. *ACS Central Science* **2018**, *4*, 39-51.

(32) Margulis, K.; Zhou, Z.; Fang, Q.; Sievers, R. E.; Lee, R. J.; Zare, R. N. *Analytical Chemistry* **2018**, *90*, 12198-12206.

(33) Cody, R. B.; Laramée, J. A.; Durst, H. D. *Analytical Chemistry* **2005**, *77*, 2297-2302.

(34) Swales, J. G.; Hamm, G.; Clench, M. R.; Goodwin, R. J. A. *International Journal of Mass Spectrometry* **2018**.

(35) Guenther, S.; Muirhead, L. J.; Speller, A. V. M.; Golf, O.; Strittmatter, N.; Ramakrishnan, R.; Goldin, R. D.; Jones, E.; Veselkov, K.; Nicholson, J.; Darzi, A.; Takats, Z. *Cancer Research* **2015**, *75*, 1828-1837.

(36) Boughton, B. A.; Thinagaran, D.; Sarabia, D.; Bacic, A.; Roessner, U. *Phytochemistry Reviews* **2016**, *15*, 445-488.

(37) Ifa, D. R.; Jackson, A. U.; Paglia, G.; Cooks, R. G. *Anal. Bioanal. Chem.* **2009**, *394*, 1995-2008.

(38) Hsu, C. C.; Dorrestein, P. C. *Curr. Opin. Biotechnol.* **2015**, *31*, 24-34.

(39) Wiseman, J. M.; Ifa, D. R.; Song, Q. Y.; Cooks, R. G. *Angew. Chem.-Int. Edit.* **2006**, *45*, 7188-7192.

(40) Paine, M. R. L.; Kooijman, P. C.; Fisher, G. L.; Heeren, R. M. A.; Fernandez, F. M.; Ellis, S. R. *Journal of Materials Chemistry B* **2017**, *5*, 7444-7460.

(41) Chen, H.; Talaty, N. N.; Takáts, Z.; Cooks, R. G. *Anal. Chem.* **2005**, *77*, 6915-6927.

(42) Ifa, D. R.; Eberlin, L. S. *Clinical Chemistry* **2016**, *62*, 111-123.

(43) Dill, A. L.; Eberlin, L. S.; Costa, A. B.; Ifa, D. R.; Cooks, R. G. *Anal. Bioanal. Chem.* **2011**, *401*, 1949.

(44) Salcedo, D.; Villalta, P. W.; Varutbangkul, V.; Wormhoudt, J. C.; Miake-Lye, R. C.; Worsnop, D. R.; Ballenthin, J. O.; Thorn, W. F.; Viggiano, A. A.; Miller, T. M.; Flagan, R. C.; Seinfeld, J. H. *International Journal of Mass Spectrometry* **2004**, *231*, 17-30.

(45) López-Herrera, J. M.; Barrero, A.; Boucard, A.; Loscertales, I. G.; Márquez, M. *Journal of the American Society for Mass Spectrometry* **2004**, *15*, 253-259.

(46) Newsome, G. A.; Ackerman, L. K.; Johnson, K. J. *Analytical Chemistry* **2014**, *86*, 11977-11980.

(47) Marotta, E.; Paradisi, C. *Journal of the American Society for Mass Spectrometry* **2009**, *20*, 697-707.

(48) Newsome, G. A.; Ackerman, L. K.; Johnson, K. J. *Journal of The American Society for Mass Spectrometry* **2016**, *27*, 135-143.

(49) Casper, C. L.; Stephens, J. S.; Tassi, N. G.; Chase, D. B.; Rabolt, J. F. *Macromolecules* **2004**, *37*, 573-578.

(50) Supaphol, P.; Mit-uppatham, C.; Nithitanakul, M. *Macromolecular Materials and Engineering* **2005**, *290*, 933-942.

(51) Sans, M.; Gharpure, K.; Tibshirani, R.; Zhang, J.; Liang, L.; Liu, J.; Young, J. H.; Dood, R. L.; Sood, A. K.; Eberlin, L. S. *Cancer Research* **2017**, *77*, 2903-2913.

(52) Douglass, K. A.; Jain, S.; Brandt, W. R.; Venter, A. R. *Journal of The American Society for Mass Spectrometry* **2012**, *23*, 1896-1902.

(53) Yamashita, M.; Fenn, J. B. *The Journal of Physical Chemistry* **1984**, *88*, 4671-4675.

(54) Eberlin, L. S.; Ifa, D. R.; Wu, C.; Cooks, R. G. *Angewandte Chemie (International ed. in English)* **2010**, *49*, 873-876.

(55) Zhu, J.; Cole, R. B. *Journal of the American Society for Mass Spectrometry* **2000**, *11*, 932-941.

(56) Angel, P. M.; Spraggins, J. M.; Baldwin, H. S.; Caprioli, R. *Analytical Chemistry* **2012**, *84*, 1557-1564.

(57) Dill, A. L.; Eberlin, L. S.; Ifa, D. R.; Cooks, R. G. *Chem. Commun.* **2011**, *47*, 2741-2746.

(58) Fletcher, J. S.; Vickerman, J. C.; Winograd, N. *Curr Opin Chem Biol* **2011**, *15*, 733-740.

(59) Seeley, E. H.; Schwamborn, K.; Caprioli, R. M. *J. Biol. Chem.* **2011**, *286*, 25459-25466.

(60) Wu, C. P.; Dill, A. L.; Eberlin, L. S.; Cooks, R. G.; Ifa, D. R. *Mass Spectrom. Rev.* **2013**, *32*, 218-243.

(61) Hankin, J. A.; Murphy, R. C. *Anal. Chem.* **2010**, *82*, 8476-8484.

(62) Laskin, J.; Heath, B. S.; Roach, P. J.; Cazares, L.; Semmes, O. J. *Analytical Chemistry* **2012**, *84*, 141-148.

(63) Chen, H. W.; Gamez, G.; Zenobi, R. *J. Am. Soc. Mass Spectrom.* **2009**, *20*, 1947-1963.

(64) Yetukuri, L.; Ekroos, K.; Vidal-Puig, A.; Oresic, M. *Mol. Biosyst.* **2008**, *4*, 121-127.

(65) Hsieh, Y.; Casale, R.; Fukuda, E.; Chen, J. W.; Knemeyer, I.; Wingate, J.; Morrison, R.; Korfmacher, W. *Rapid Communications in Mass Spectrometry* **2006**, *20*, 965-972.

(66) Lou, X. W.; van Dongen, J. L. J.; Vekemans, J.; Meijer, E. W. *Rapid. Commun. Mass Sp.* **2009**, *23*, 3077-3082.

(67) Hsu, C. C.; Chou, P. T.; Zare, R. N. *Anal. Chem.* **2015**, *87*, 11171-11175.

(68) Kertesz, V.; Weiskittel, T. M.; Van Berkel, G. J. *Anal. Bioanal. Chem.* **2015**, *407*, 2117-2125.

(69) Lombard-Banek, C.; Moody, S. A.; Nemes, P. *Angew. Chem. Int. Edit.* **2016**, *55*, 2454-2458.

(70) Collins, D. C.; Lee, M. L. *Anal. Bioanal. Chem.* **2002**, *372*, 66-73.

(71) Kanu, A. B.; Dwivedi, P.; Tam, M.; Matz, L.; Hill, H. H. *J. Mass Spectrom.* **2008**, *43*, 1-22.

(72) Ray, J. A.; Kushnir, M. M.; Yost, R. A.; Rockwood, A. L.; Meikle, A. W. *Clin. Chim. Acta* **2015**, *438*, 330-336.

(73) Guevremont, R. *Can. J. Anal. Sci. Spectrosc.* **2004**, *49*, 105-113.

(74) Kolakowski, B. M.; Mester, Z. *Analyst* **2007**, *132*, 842-864.

(75) Da Costa, C.; Turner, M.; Reynolds, J. C.; Whitmarsh, S.; Lynch, T.; Creaser, C. S. *Anal. Chem.* **2016**, *88*, 2453-2458.

(76) Manicke, N. E.; Belford, M. *Journal of the American Society for Mass Spectrometry* **2015**, *26*, 701-705.

(77) Griffiths, R. L.; Dexter, A.; Creese, A. J.; Cooper, H. J. *Analyst* **2015**, *14*, 6879-6885.

(78) Li, H.; Smith, B. K.; Mark, L.; Nemes, P.; Nazarian, J.; Vertes, A. *International Journal of Mass Spectrometry* **2015**, *377*, 681-689.

(79) Roscioli, K. M.; Tufariello, J. A.; Zhang, X.; Li, S. X.; Goetz, G. H.; Cheng, G. L.; Siems, W. F.; Hill, H. H. *Analyst* **2014**, *139*, 1740-1750.

(80) Galhena, A. S.; Harris, G. A.; Kwasnik, M.; Fernandez, F. M. *Anal. Chem.* **2010**, *82*, 9159-9163.

(81) Sarsby, J.; Griffiths, R. L.; Race, A. M.; Bunch, J.; Randall, E. C.; Creese, A. J.; Cooper, H. J. *Anal. Chem.* **2015**, *87*, 6794-6800.

(82) Griffiths, R. L.; Creese, A. J.; Race, A. M.; Bunch, J.; Cooper, H. J. *Anal. Chem.* **2016**, *88*, 6758-6766.

(83) Robichaud, G.; Garrard, K. P.; Barry, J. A.; Muddiman, D. C. *J. Am. Soc. Mass Spectom.* **2013**, *24*, 718-721.

(84) Swearingen, K. E.; Moritz, R. L. *Expert Review of Proteomics* **2012**, *9*, 505-517.

(85) Ji, J.; Kline, A. E.; Amoscato, A.; Samhan-Arias, A. K.; Sparvero, L. J.; Tyurin, V. A.; Tyurina, Y. Y.; Fink, B.; Manole, M. D.; Puccio, A. M.; Okonkwo, D. O.; Cheng, J. P.; Alexander, H.; Clark, R. S. B.; Kochanek, P. M.; Wipf, P.; Kagan, V. E.; Bayir, H. *Nat. Neurosci.* **2012**, *15*, 1407-1413.

(86) Sapandowski, A.; Stope, M.; Evert, K.; Evert, M.; Zimmermann, U.; Peter, D.; Paege, I.; Burchardt, M.; Schild, L. *Mol. Cell. Biochem.* **2015**, *410*, 175-185.

(87) Corcelli, A.; Angelini, R.; Lobasso, S.; Bowron, A.; Steward, C. *Faseb J.* **2015**, *29*.

(88) Sandhoff, K.; Harzer, K. *J. Neurosci.* **2013**, *33*, 10195-10208.

(89) Yu, R. K.; Tsai, Y. T.; Ariga, T. *Neurochem. Res.* **2012**, *37*, 1230-1244.

(90) Prideaux, B.; ElNaggar, M. S.; Zimmerman, M.; Wiseman, J. M.; Li, X.; Dartois, V. *Int. J. Mass Spectrom.* **2015**, *377*, 699-708.

(91) Zang, L.; Toy, D. P.; Hancock, W. S.; Sgroi, D. C.; Karger, B. L. *J. Proteome Res.* **2004**, *3*, 604-612.

(92) Helmreich, E. J. M. *Biophys. Chem.* **2002**, *100*, 519-534.

(93) de Carvalho, C. C. C. R.; Caramujo, M. J. *Molecules* **2018**, *23*, 2583.

(94) Kuhajda, F. P. *Nutrition* **2000**, *16*, 202-208.

(95) Alo, P. L.; Visca, P.; Marci, A.; Mangoni, A.; Botti, C.; Di Tondo, U. *Cancer* **1996**, *77*, 474-482.

(96) Alò, P. L.; Visca, P.; Trombetta, G.; Mangoni, A.; Lenti, L.; Monaco, S.; Botti, C.; Serpieri, D. E.; Di Tondo, U. *Tumori J.* **1999**, *85*, 35-40.

(97) Pizer, E. S.; Lax, S. F.; Kuhajda, F. P.; Pasternack, G. R.; Kurman, R. J. *Cancer* **1998**, *83*, 528-537.

(98) Epstein, J. I.; Carmichael, M.; Partin, A. W. *Urology* **1995**, *45*, 81-86.

(99) Kuhajda, F. P.; Jenner, K.; Wood, F. D.; Hennigar, R. A.; Jacobs, L. B.; Dick, J. D.; Pasternack, G. R. *Proc. Nat. Acad. Sci. USA* **1994**, *91*, 6379-6383.

(100) Kridel, S. J.; Lowther, W. T.; Pemble, C. W. *Expert Opin. Inv. Drug* **2007**, *16*, 1817-1829.

(101) Menendez, J. A.; Lupu, R. *Expert Opin. Ther. Tar.* **2017**, *21*, 1001-1016.

(102) Murphy, R. C.; Axelsen, P. H. *Mass Spectrom Rev* **2011**, *30*, 579-599.

(103) Mitchell, T. W.; Pham, H.; Thomas, M. C.; Blanksby, S. J. *J. Chromatogr. B* **2009**, *877*, 2722-2735.

(104) Han, X. In *Lipidomics*, 2016, pp 229-242.

(105) Zheng, X.; Smith, R. D.; Baker, E. S. *Curr Opin Chem Biol* **2018**, *42*, 111-118.

(106) Zhang, W.; Zhang, D.; Chen, Q.; Wu, J.; Ouyang, Z.; Xia, Y. *Nat. Commun.* **2019**, *10*, 79.

(107) Xie, X.; Xia, Y. *Anal. Chem.* **2019**, *91*, 7173-7180.

(108) Wang, M.; Han, R. H.; Han, X. *Anal. Chem.* **2013**, *85*, 9312-9320.

(109) Randolph, C. E.; Foreman, D. J.; Blanksby, S. J.; McLuckey, S. A. *Anal. Chem.* **2019**, *91*, 9032-9040.

(110) Randolph, C. E.; Foreman, D. J.; Betancourt, S. K.; Blanksby, S. J.; McLuckey, S. A. *Anal. Chem.* **2018**, *90*, 12861-12869.

(111) Paine, M. R. L.; Poad, B. L. J.; Eijkel, G. B.; Marshall, D. L.; Blanksby, S. J.; Heeren, R. M. A.; Ellis, S. R. *Angewandte Chemie International Edition* **2018**, *57*, 10530-10534.

(112) Ma, X.; Zhao, X.; Li, J.; Zhang, W.; Cheng, J.-X.; Ouyang, Z.; Xia, Y. *Anal. Chem.* **2016**, *88*, 8931-8935.

(113) Murphy, R. C.; Okuno, T.; Johnson, C. A.; Barkley, R. M. *Anal. Chem.* **2017**, *89*, 8545-8553.

(114) Feng, Y.; Chen, B.; Yu, Q.; Li, L. *Anal. Chem.* **2019**, *91*, 1791-1795.

(115) Kuo, T.-H.; Chung, H.-H.; Chang, H.-Y.; Lin, C.-W.; Wang, M.-Y.; Shen, T.-L.; Hsu, C.-C. *Anal. Chem.* **2019**, *91*, 11905-11915.

(116) Hsu, F.-F.; Turk, J. *J. Am. Soc. Mass Spectrom.* **1999**, *10*, 600-612.

(117) Yang, K.; Dilthey, B. G.; Gross, R. W. *Anal. Chem.* **2013**, *85*, 9742-9750.

(118) Klein, D. R.; Brodbelt, J. S. *Anal. Chem.* **2017**, *89*, 1516-1522.

(119) Ryan, E.; Nguyen, C. Q. N.; Shiea, C.; Reid, G. E. *J. Am. Soc. Mass Spectrom.* **2017**, *28*, 1406-1419.

(120) Brown, S. H. J.; Mitchell, T. W.; Blanksby, S. J. *Biochimica et Biophysica Acta (BBA) - Molecular and Cell Biology of Lipids* **2011**, *1811*, 807-817.

(121) Jones, J. W.; Thompson, C. J.; Carter, C. L.; Kane, M. A. *J Mass Spectrom* **2015**, *50*, 1327-1339.

(122) Yoo, H. J.; Håkansson, K. *Anal. Chem.* **2010**, *82*, 6940-6946.

(123) Pham, H. T.; Maccarone, A. T.; Campbell, J. L.; Mitchell, T. W.; Blanksby, S. J. *Journal of the American Society for Mass Spectrometry* **2013**, *24*, 286-296.

(124) Fang, M.; Rustam, Y.; Palmieri, M.; Sieber, O. M.; Reid, G. E. *Analytical and Bioanalytical Chemistry* **2020**.

(125) Poad, B. L. J.; Marshall, D. L.; Harazim, E.; Gupta, R.; Narreddula, V. R.; Young, R. S. E.; Duchoslav, E.; Campbell, J. L.; Broadbent, J. A.; Cvačka, J.; Mitchell, T. W.; Blanksby, S. J. *J. Am. Soc. Mass Spectrom.* **2019**, *30*, 2135-2143.

(126) Williams, P. E.; Klein, D. R.; Greer, S. M.; Brodbelt, J. S. *J. Am. Chem. Soc.* **2017**, *139*, 15681-15690.

(127) Sun, C.; Li, T.; Song, X.; Huang, L.; Zang, Q.; Xu, J.; Bi, N.; Jiao, G.; Hao, Y.; Chen, Y.; Zhang, R.; Luo, Z.; Li, X.; Wang, L.; Wang, Z.; Song, Y.; He, J.; Abliz, Z. *Proc. Nat. Acad. Sci. USA* **2019**, *116*, 52-57.

(128) Calligaris, D.; Caragacianu, D.; Liu, X.; Norton, I.; Thompson, C. J.; Richardson, A. L.; Golshan, M.; Easterling, M. L.; Santagata, S.; Dillon, D. A.; Jolesz, F. A.; Agar, N. Y. R. *Proc. Nat. Acad. Sci. USA* **2014**, *111*, 15184-15189.

(129) Guo, S.; Wang, Y.; Zhou, D.; Li, Z. *Sci. Rep.* **2014**, *4*, 5959.

(130) Jackson, A. U.; Shum, T.; Sokol, E.; Dill, A.; Cooks, R. G. *Anal. Bioanal. Chem.* **2011**, *399*, 367-376.

(131) Lostun, D.; Perez, C. J.; Licence, P.; Barrett, D. A.; Ifa, D. R. *Anal. Chem.* **2015**, *87*, 3286-3293.

(132) Bednařík, A.; Bölsker, S.; Soltwisch, J.; Dreisewerd, K. *Angew. Chem. Int. Ed.* **2018**, *57*, 12092-12096.

(133) Wäldchen, F.; Spengler, B.; Heiles, S. *J. Am. Chem. Soc.* **2019**, *141*, 11816-11820.

(134) Tang, F.; Guo, C.; Ma, X.; Zhang, J.; Su, Y.; Tian, R.; Shi, R.; Xia, Y.; Wang, X.; Ouyang, Z. *Anal. Chem.* **2018**, *90*, 5612-5619.

(135) Klein, D. R.; Feider, C. L.; Garza, K. Y.; Lin, J. Q.; Eberlin, L. S.; Brodbelt, J. S. *Analytical Chemistry* **2018**, *90*, 10100-10104.

(136) Anderson, J. L.; Ding, R.; Ellern, A.; Armstrong, D. W. *Journal of the American Chemical Society* **2005**, *127*, 593-604.

(137) Rao, W.; Mitchell, D.; Licence, P.; Barrett, D. A. *Rapid Commun. Mass Spectrom.* **2014**, *28*, 616-624.

(138) Lostun, D.; Perez, C. J.; Licence, P.; Barrett, D. A.; Ifa, D. R. *Analytical Chemistry* **2015**, *87*, 3286-3293.

(139) Shaw, J. B.; Li, W.; Holden, D. D.; Zhang, Y.; Griep-Raming, J.; Fellers, R. T.; Early, B. P.; Thomas, P. M.; Kelleher, N. L.; Brodbelt, J. S. *Journal of the American Chemical Society* **2013**, *135*, 12646-12651.

(140) Kessner, D.; Chambers, M.; Burke, R.; Agus, D.; Mallick, P. *Bioinformatics* **2008**, *24*, 2534-2536.

(141) Race, A. M.; Styles, I. B.; Bunch, J. *Journal of Proteomics* **2012**, *75*, 5111-5112.

(142) Bokhart, M. T.; Nazari, M.; Garrard, K. P.; Muddiman, D. C. *Journal of The American Society for Mass Spectrometry* **2018**, *29*, 8-16.

(143) Liebisch, G.; Vizcaíno, J. A.; Köfeler, H.; Trötzmüller, M.; Griffiths, W. J.; Schmitz, G.; Spener, F.; Wakelam, M. J. O. *J Lipid Res* **2013**, *54*, 1523-1530.

(144) Klein, D. R.; Brodbelt, J. S. *Analytical Chemistry* **2017**, *89*, 1516-1522.

(145) Klein, D. R.; Feider, C. L.; Garza, K. Y.; Lin, J. Q.; Eberlin, L. S.; Brodbelt, J. S. *Anal. Chem.* **2018**, *90*, 10100-10104.

(146) Currie, E.; Schulze, A.; Zechner, R.; Walther, Tobias C.; Farese, Robert V. *Cell Metab.* **2013**, *18*, 153-161.

(147) Monaco, M. E. *Oncotarget* **2017**, *8*, 29487-29500.

(148) Wheeler, J. M. *J Reprod. Med.* **1989**, *34*, 41-46.

(149) Shafrir, A. L.; Farland, L. V.; Shah, D. K.; Harris, H. R.; Kvaskoff, M.; Zondervan, K.; Missmer, S. A. *Best Practice & Research Clinical Obstetrics & Gynaecology* **2018**, *51*, 1-15.

(150) Canis, M.; Donnez, J. G.; Guzick, D. S.; Halme, J. K.; Rock, J. A.; Schenken, R. S.; Vernon, M. W. *Fertil. Steril.* **1997**, *67*, 817-821.

(151) Simoens, S.; Dunselman, G.; Dirksen, C.; Hummelshoj, L.; Bokor, A.; Brandes, I.; Brodszky, V.; Canis, M.; Colombo, G. L.; DeLeire, T.; Falcone, T.; Graham, B.; Halis, G.; Horne, A.; Kanj, O.; Kjer, J. J.; Kristensen, J.; Lebovic, D.; Mueller, M.; Vigano, P., et al. *Hum. Reprod.* **2012**, *27*, 1292-1299.

(152) Eskenazi, B.; Warner, M. L. *Obstet. Gynecol. Clin. N. Am.* **1997**, *24*, 235-258.

(153) Sampson, J. A. *Am. J. Obstet. Gynecol.* **1927**, *14*, 422-469.

(154) Vercellini, P.; Vigano, P.; Somigliana, E.; Fedele, L. *Nat. Rev. Endocrinol.* **2014**, *10*, 261-275.

(155) Nisenblat, V.; Prentice, L.; Bossuyt, P. M. M.; Farquhar, C.; Hull, M. L.; Johnson, N. *Cochrane Database Syst Rev.* **2016**, 132.

(156) May, K. E.; Conduit-Hulbert, S. A.; Villar, J.; Kirtley, S.; Kennedy, S. H.; Becker, C. M. *Hum. Reprod. Update* **2010**, *16*, 651-674.

(157) Schweppe, K.-W.; Wynn, R. M.; Beller, F. K. *Am. J. Obstet. Gynecol.* **1984**, *148*, 1024-1039.

(158) Bedaiwy, M. A.; Gupta, S.; Noriega, J.; Brainard, J.; Agarwal, A.; Falcone, T. *Fertil. Steril.* **2008**, *90*, S438.

(159) Taylor, R. N.; Lebovic, D. I.; Mueller, M. D. *Ann. N. Y. Acad. Sci.* **2002**, *955*, 89-100.

(160) Lee, Y. H.; Tan, C. W.; Venkatratnam, A.; Tan, C. S.; Cui, L.; Loh, S. F.; Griffith, L.; Tannenbaum, S. R.; Chan, J. K. Y. *J. Clin. Endocrinol. Metab.* **2014**, *99*, E1913-E1921.

(161) Beste, M. T.; Pfäffle-Doyle, N.; Prentice, E. A.; Morris, S. N.; Lauffenburger, D. A.; Isaacson, K. B.; Griffith, L. G. *Sci. Transl. Med.* **2014**, *6*.

(162) Hocher, B.; Adamski, J. *Nat. Rev. Nephrol.* **2017**, *13*, 269-284.

(163) Patel, R. *Clin. Chem.* **2015**, *61*, 100-111.

(164) Belczacka, I.; Latosinska, A.; Metzger, J.; Marx, D.; Vlahou, A.; Mischak, H.; Frantzi, M. *Mass Spectrom. Rev.* **2019**, *38*, 49-78.

(165) Cordeiro, F. B.; Cataldi, T. R.; Perkel, K. J.; do Vale Teixeira da Costa, L.; Rochetti, R. C.; Stevanato, J.; Eberlin, M. N.; Zylbersztejn, D. S.; Cedenho, A. P.; Turco, E. G. L. *J. Assist. Reprod. Genet.* **2015**, *32*, 1817-1825.

(166) Cordeiro, F. B.; Cataldi, T. R.; do Vale Teixeira da Costa, L.; de Souza, B. Z.; Montani, D. A.; Fraietta, R.; Labate, C. A.; Cedenho, A. P.; Lo Turco, E. G. *Metabolomics* **2017**, *13*, 120.

(167) Adamyan, L.; Starodubtseva, N.; Borisova, A.; Stepanian, A.; Chagovets, V.; Salimova, D.; Wang, Z.; Kononikhin, A.; Popov, I.; Bugrova, A.; Chingin, K.; Kozachenko, A.; Chen, H.; Frankevich, V. *J. Minim. Invasive Gynecol.* **2017**.

(168) Kasvandik, S.; Samuel, K.; Peters, M.; Eimre, M.; Peet, N.; Roost, A. M.; Padrik, L.; Paju, K.; Peil, L.; Salumets, A. *J. Proteome Res.* **2016**, *15*, 572-584.

(169) Chagovets, V. V.; Wang, Z.; Kononikhin, A. S.; Starodubtseva, N. L.; Borisova, A.; Salimova, D.; Popov, I. A.; Kozachenko, A. V.; Chingin, K.; Chen, H.; Frankevich, V. E.; Adamyan, L. V.; Sukhikh, G. T. *Sci. Rep.* **2017**, *7*, 2546.

(170) Dutta, M.; Anitha, M.; Smith, P. B.; Chiaro, C. R.; Maan, M.; Chaudhury, K.; Patterson, A. D. *J. Proteome Res.* **2016**, *15*, 2626-2633.

(171) Li, J.; Gao, Y.; Guan, L.; Zhang, H.; Sun, J.; Gong, X.; Li, D.; Chen, P.; Ma, Z.; Liang, X.; Huang, M.; Bi, H. *Front. Physiol.* **2018**, *9*, 14.

(172) Parazzini, F.; Esposito, G.; Tozzi, L.; Noli, S.; Bianchi, S. *Eur. J. Obstet. Gynecol. Reprod. Biol.* **2016**, *209*, 3-7.

(173) Teng, S.-W.; Horng, H.-C.; Ho, C.-H.; Yen, M.-S.; Chao, H.-T.; Wang, P.-H. *J. Chin. Med. Assoc.* **2016**, *79*, 577-582.

(174) Kajiyama, H.; Suzuki, S.; Yoshihara, M.; Tamauchi, S.; Yoshikawa, N.; Niimi, K.; Shibata, K.; Kikkawa, F. *Free Radical Biology and Medicine* **2019**, *133*, 186-192.

(175) Ahn, S. H.; Singh, V.; Tayade, C. *Fertil. Steril.* **2007**, *107*, 523-532.

(176) Buchberger, A. R.; DeLaney, K.; Johnson, J.; Li, L. J. *Anal. Chem.* **2018**, *90*, 240-265.

(177) Eberlin, L. S.; Tibshirani, R. J.; Zhang, J.; Longacre, T. A.; Berry, G. J.; Bingham, D. B.; Norton, J. A.; Zare, R. N.; Poultsides, G. A. *Proc. Nat. Acad. Sci. U.S.A.* **2014**, *111*, 2436-2441.

(178) Norris, J. L.; Caprioli, R. M. *Chem. Rev.* **2013**, *113*, 2309-2342.

(179) Eberlin, L. S.; Ferreira, C. R.; Dill, A. L.; Ifa, D. R.; Cooks, R. G. *Biochim. Biophys. Acta Mol. Cell Biol. Lipids* **2011**, *1811*, 946-960.

(180) Palmer, A.; Phapale, P.; Chernyavsky, I.; Lavigne, R.; Fay, D.; Tarasov, A.; Kovalev, V.; Fuchser, J.; Nikolenko, S.; Pineau, C.; Becker, M.; Alexandrov, T. *Nature Methods* **2016**, *14*, 57.

(181) Chambers, M. C.; Maclean, B.; Burke, R.; Amodei, D.; Ruderman, D. L.; Neumann, S.; Gatto, L.; Fischer, B.; Pratt, B.; Egertson, J.; Hoff, K.; Kessner, D.; Tasman, N.; Shulman, N.; Frewen, B.; Baker, T. A.; Brusniak, M. Y.; Paulse, C.; Creasy, D.; Flashner, L., et al. *Nat. Biotechnol.* **2012**, *30*, 918-920.

(182) Race, A. M.; Styles, I. B.; Bunch, J. *J. Proteome Res.* **2012**, *75*, 5111-5112.

(183) Robichaud, G.; Garrard, K. P.; Barry, J. A.; Muddiman, D. C. *Journal of the American Society for Mass Spectrometry* **2013**, *24*, 718-721.

(184) Friedman, J.; Hastie, T.; Tibshirani, R. *J. Stat. Softw.* **2010**, *33*, 1-22.

(185) Efron, B. *J. Am. Stat. Assoc* **2004**, *99*, 96-104.

(186) Veselkov, K.; Sleeman, J.; Claude, E.; Vissers, J. P. C.; Galea, D.; Mroz, A.; Laponogov, I.; Towers, M.; Tonge, R.; Mirnezami, R.; Takats, Z.; Nicholson, J. K.; Langridge, J. I. *Sci. Rep.* **2018**, *8*.

(187) Tillner, J.; Wu, V.; Jones, E. A.; Pringle, S. D.; Karancsi, T.; Dannhorn, A.; Veselkov, K.; McKenzie, J. S.; Takats, Z. *J. Am. Soc. Mass Spectom.* **2017**, *28*, 2090-2098.

(188) Coulon, D.; Faure, L.; Salmon, M.; Wattelet, V.; Bessoule, J.-J. *Biochimie* **2012**, *94*, 75-85.

(189) Nielsen, M. M. B.; Lambertsen, K. L.; Clausen, B. H.; Meyer, M.; Bhandari, D. R.; Larsen, S. T.; Poulsen, S. S.; Spengler, B.; Janfelt, C.; Hansen, H. S. *Scientific Reports* **2016**, *6*, 39571.

(190) Tibshirani, R. *J. R. Stat. Soc. Series B Stat. Methodol.* **1996**, *58*, 267-288.

(191) Clement, P. B. *Adv Anat Pathol.* **2007**, *14*, 241-260.

(192) Hopeman, M. M.; Riley, J. K.; Frolova, A. I.; Jiang, H.; Jungheim, E. S. *Reprod. Sci.* **2015**, *22*, 1083-1087.

(193) Vouk, K.; Hevir, N.; Ribic-Pucelj, M.; Haarpaintner, G.; Scherb, H.; Osredkar, J.; Moller, G.; Prehn, C.; Rizner, T. L.; Adamski, J. *Hum. Reprod.* **2012**, *27*, 2955-2965.

(194) Vouk, K.; Ribič-Pucelj, M.; Adamski, J.; Rižner, T. L. *J. Steroid Biochem. Mol. Biol.* **2016**, *159*, 60-69.

(195) Letsiou, S.; Peterse, D. P.; Fassbender, A.; Hendriks, M. M.; van den Broek, N. J.; Berger, R.; O, D. F.; Vanhie, A.; Vodolazkaia, A.; Van Langendonckt, A.; Donnez, J.;

Harms, A. C.; Vreeken, R. J.; Groothuis, P. G.; Dolmans, M.-M.; Brenkman, A. B.; D'Hooghe, T. M. *Fertil. Steril.* **2017**, *107*, 699-706.e696.

(196) Leventis, P. A.; Grinstein, S. *Annu. Rev. Biophys.* **2010**, *39*, 407-427.

(197) Bevers, E. M.; Comfurius, P.; van Rijn, J. L.; Hemker, H. C.; Zwaal, R. F. *Eur. J. Biochem.* **1982**, *122*, 429-436.

(198) McKinnon, B.; Bertschi, D.; Wotzkow, C.; Bersinger, N. A.; Evers, J.; Mueller, M. D. *J. Mol. Endocrinol.* **2014**, *52*, 169-179.

(199) Ahad, F.; Ganie, S. A. *Indian J. Endocrinol. Metab.* **2010**, *14*, 13-17.

(200) Ghert, W. R.; Eskin, B. A.; Google Patents, 1995.

(201) Li, T.; He, J.; Mao, X.; Bi, Y.; Luo, Z.; Guo, C.; Tang, F.; Xu, X.; Wang, X.; Wang, M.; Chen, J.; Abliz, Z. *Sci. Rep.* **2015**, *5*, 14089.

(202) Nisolle, M.; Donnez, J. *Fertil. Steril.* **1997**, *68*, 585-596.

(203) Teichmann, A. T.; Cremer, P.; Wieland, H.; Kuhn, W.; Seidel, D. *Maturitas* **1988**, *10*, 27-33.

(204) Burry, K. A.; Patton, P. E.; Illingworth, D. R. *American Journal of Obstetrics & Gynecology* **1989**, *160*, 1454-1461.

(205) Griffiths, R. L.; Hughes, J. W.; Abbatiello, S. E.; Belford, M. W.; Styles, I. B.; Cooper, H. J. *Analytical Chemistry* **2020**.

(206) Li, G.; Delafield, D. G.; Li, L. *TrAC Trends in Analytical Chemistry* **2019**, 115546.

(207) Bowman, A. P.; Abzalimov, R. R.; Shvartsburg, A. A. *Journal of the American Society for Mass Spectrometry* **2017**, *28*, 1552-1561.

(208) Deng, L.; Ibrahim, Y. M.; Baker, E. S.; Aly, N. A.; Hamid, A. M.; Zhang, X.; Zheng, X.; Garimella, S. V. B.; Webb, I. K.; Prost, S. A.; Sandoval, J. A.; Norheim, R. V.; Anderson, G. A.; Tolmachev, A. V.; Smith, R. D. *ChemistrySelect* **2016**, *1*, 2396-2399.

(209) Zhang, J.; Feider, C. L.; Nagi, C.; Yu, W.; Carter, S. A.; Suliburk, J.; Cao, H. S. T.; Eberlin, L. S. *Journal of The American Society for Mass Spectrometry* **2017**, *28*, 1166-1174.

(210) Garza, K. Y.; Feider, C. L.; Klein, D. R.; Rosenberg, J. A.; Brodbelt, J. S.; Eberlin, L. S. *Analytical Chemistry* **2018**, *90*, 7785-7789.

(211) Towers, M. W.; Karancsi, T.; Jones, E. A.; Pringle, S. D.; Claude, E. *Journal of the American Society for Mass Spectrometry* **2018**, *29*, 2456-2466.